Corresponding author: Alexander S. Bradley (abradley@wustl.edu)
Department of Earth, Environmental, and Planetary Sciences
Washington University in St. Louis

# Spatial autocorrelation inflates the global leaf-wax $\delta^2$H–precipitation slope

Alexander S. Bradley[a,*]

[a]*Department of Earth, Environmental, and Planetary Sciences, Washington University in St. Louis, 1 Brookings Drive, Saint Louis, Missouri 63130, USA*

## Abstract

Leaf wax hydrogen isotope ratios ($\delta^2H_{wax}$) are used to make inferences about past hydroclimate, but global calibrations between $\delta^2H_{wax}$ and precipitation isotopes ($\delta^2H_{precip}$) ignore spatial autocorrelation and inflate apparent relationships. This study compiled 1,129 surface sediment and soil measurements of $\delta^2H_{wax}$ from $n$-$C_{29}$ alkanes and developed hierarchical Bayesian spatial models to separate geographic covariation from isotopic processes. The fitted spatial field accounted for 48–57% of variance and had characteristic length scales of ~3,600–3,950 km. Accounting for this structure reduces the $\delta^2H_{wax}$–$\delta^2H_{precip}$ slope from a non-spatial baseline of 0.78 to 0.53–0.62, indicating that a substantial fraction of the non-spatial slope estimate reflects confounding by spatial structure rather than the underlying wax–precipitation isotope relationship.

The dominant spatial effects are shifts in regional intercepts. Slopes vary modestly around a near-uniform global mean. Grass and tree cover have negative effects on $\delta^2H_{wax}$, and the $\delta^2H_{precip}$ × tree and × shrub interactions are small but statistically discernible even after spatial adjustment. Elevation, annual precipitation, and $C_4$ fraction effects are weak. Spatial calibrations cut the residual standard deviation in $\delta^2H_{wax}$ at the calibration sites by ~25% (from ~21‰ to ~16‰). Inverting through the calibration gives a single-point $\delta^2H_{precip}$ posterior standard deviation of ~29‰ and, for independent samples within a single record, a 95% detection threshold of ~81‰. For within-record contrasts, positively correlated calibration residuals can partially cancel, and thresholds are correspondingly lower. These uncertainty and threshold estimates are lower bounds; unmodeled residual confounding, spatial-intercept and covariate uncertainty, and non-stationarity would widen real-world reconstruction errors. Inversions are implemented in the accompanying R package `leafwax`.

*Keywords:* leaf wax, hydrogen isotopes, paleoclimate, spatial autocorrelation

## 1. Introduction

Sedimentary leaf waxes contain hydrogen isotope ratios ($\delta^2H_{wax}$) that are interpreted as paleorecords of hydroclimate (Sachse et al., 2012). These waxes are long-chain $n$-alkanes and $n$-acids made by terrestrial plants, that partially inherit their isotopic composition from precipitation. Because of their link to precipitation isotopes ($\delta^2H_{precip}$), paleo-records of $\delta^2H_{wax}$ have been inferred to record information about past rainfall amount, moisture sources, and atmospheric circulation (Tierney et al., 2008; Konecky et al., 2016; Daniels et al., 2021; Martins et al., 2022; Zhao et al., 2024).

Biology, climate, and sedimentary processes all complicate the relationship between $\delta^2H_{wax}$ and $\delta^2H_{precip}$. Plant functional types (PFTs) show systematic differences in apparent fractionation. The isotopic offset between precipitation and wax can be tens of permil different among trees, shrubs, and grasses (Liu et al., 2006; Liu and An, 2019; Konecky et al., 2019). These patterns are probably related to variations in rooting depths, leaf morphologies, and water-use strategies. Among grasses, $C_4$ species tend to make waxes that are more $^2$H-enriched than $C_3$ grasses growing under similar conditions, possibly due to differences in leaf-water evaporative enrichment (Smith and Freeman, 2006) or biosynthetic fractionation (Gamarra et al., 2016).

*Corresponding author.
*Email address:* `abradley@wustl.edu` (Alexander S. Bradley)

Climate variables other than precipitation isotopes also affect the $\delta^2H_{wax}$ signal. Temperature influences the isotopic composition of precipitation, through equilibrium fractionation, along with the degree of evaporative enrichment in leaves (Kahmen et al., 2013; Cernusak et al., 2016). Atmospheric humidity sets transpiration rates which affect how much isotopic enrichment occurs as water is lost from leaves (Sachse et al., 2012). Soil moisture governs which water pools a plant draws on and when it is photosynthetically active, which can bias the seasonal signal that ends up in the waxes (Wu et al., 2016; Goldsmith et al., 2018; Tipple et al., 2013). Each of these is mechanistically important and each correlates strongly with $\delta^2H_{precip}$, so the individual effects are hard to statistically separate (Bowen, 2008; Bowen et al., 2019).

Sedimentary archives integrate wax signals over basin-scale regions. As waxes from plants across a catchment are transported to a depositional environment, they mix into a composite signal whose source area is poorly defined (Galy and Eglinton, 2011). Elevation gradients within a catchment add isotopic variation through precipitation lapse rates and shifts in vegetation. Monsoons and storm tracks, along with moisture recycling impose additional variation on precipitation isotopes and ecosystem properties, in spatially coherent ways.

These overlapping influences produce considerable scatter in global $\delta^2H_{wax}$-$\delta^2H_{precip}$ calibrations (Sachse et al., 2012; McFarlin et al., 2019). Paleoclimate applications require knowing how large a change in $\delta^2H_{wax}$ must be in order to confidently infer that $\delta^2H_{precip}$ has changed. This requires understanding both the residual uncertainty around the $\delta^2H_{wax}$-$\delta^2H_{precip}$ relationship, and the temporal autocorrelation structure of the $\delta^2H_{wax}$ record.

One way of quantifying the residual uncertainty is through ordinary least squares regression (Figure 1). This approach estimates the slope and residual variance of the regression, with predictive uncertainty expressed through a prediction interval (McClelland et al., 2021). For $\delta^2H_{precip}$ reconstructions, these prediction intervals are large, typically more than 100‰ (see supplement). But OLS treats all sites as statistically independent and so implicitly ignores spatial autocorrelation. This overstates the amount of independent information in the calibration dataset and can inflate the apparent strength of the proxy relationship through spatial confounding (Hodges and Reich, 2010).

Another common practice is to assume a constant apparent fractionation factor (e.g. $\varepsilon_{app} \approx$ -120‰ for $C_3$ plants), calculating $\delta^2H_{precip} = \delta^2H_{wax} - \varepsilon_{app}$ to invert measured $\delta^2H_{wax}$ values (Feakins et al., 2016; Corcoran et al., 2022). Doing so implicitly assumes a unit slope and applies a uniform offset, without accounting for geographic variation or quantifying residual uncertainty. The same constant-fractionation logic sits behind forward proxy system models (PSMs) such as WaxPSM (Konecky et al., 2019), which simulate $\delta^2H_{wax}$ from environmental inputs. PSMs produce synthetic proxy records to compare against climate model output (Evans et al., 2013). But PSMs are not statistically invertible; uncertainty derives from deterministic transfer functions only, and there is no residual error term for calibration scatter. Defensible paleoclimate reconstruction needs calibrated prediction intervals (National Research Council, 2006; Tingley and Huybers, 2010), which neither WaxPSM nor the constant $\varepsilon_{app}$ approach supplies for $\delta^2H_{precip}$. Existing frameworks describe important controls on $\delta^2H_{wax}$, but they do not solve the inverse problem central to paleoclimate reconstruction: whether an observed shift in sedimentary $\delta^2H_{wax}$ marks a statistically meaningful change in past $\delta^2H_{precip}$.

We address this gap with hierarchical Bayesian spatial models that jointly estimate the $\delta^2H_{wax}$-$\delta^2H_{precip}$ slope, intercept, and residual variance while accounting for spatial autocorrelation. By treating geographic variation as a latent spatial process instead of noise, the model can separate identifiable environmental relationships from spatially structured covariance. Applied to a global compilation of 1,129 surface sediment and soil $\delta^2H_{wax}$ measurements, it reduces the non-spatial baseline $\delta^2H_{wax}$-$\delta^2H_{precip}$ slope from 0.78 to 0.53–0.62, which indicates that conventional calibrations partly reflect geographic covariation. The fitted spatial component accounts for much of the variance in the dataset. The spatial field absorbs some of the vegetation effect, but grass and tree cover still show negative associations with $\delta^2H_{wax}$, and the $\delta^2H_{precip}$ × tree and × shrub interactions are statistically resolved. For paleoclimate reconstruction, location-specific spatial models cut uncertainty by ∼25%, and models restricted to paleo-reconstructable variables do nearly as well as those that include modern vegetation data. The accompanying R package `leafwax` supports spatially aware reconstructions with full uncertainty propagation.

## 2. Methods

### *2.1. Data Compilation*

We compiled 1,129 globally distributed surface sediment and soil measurements of the *n*-$C_{29}$ alkane $\delta^2H_{wax}$ (Section S2.1 for detailed methods on data preparation). We modeled the *n*-$C_{29}$ alkane because it is abundant in sediments,

of terrestrial plant origin, and already extensively calibrated. The approach described here could also be used for long-chain alkanoic acids. Sample locations spanned all inhabited continents (Figure 2). Asia was sampled most densely (n = 551), followed by the Americas (n = 373), Africa (n = 143), Oceania (n = 32), and Europe (n = 30). Site elevations ranged from sea level to over 5,200 meters and covered all major terrestrial biomes.

For each site we took the precipitation hydrogen isotope values ($\delta^2 H^{\mathrm{OIPC}}_{\mathrm{precip}}$) from the Online Isotopes in Precipitation Calculator (OIPC) (Bowen and Revenaugh, 2003; Bowen, 2018), a raster dataset that interpolates gridded estimates from GNIP station data and geographic predictors. Seven additional environmental covariates went into the compilation: elevation from GMTED2010 (Amatulli et al., 2018), vegetation cover fractions (trees, shrubs, grasses) from MODIS land cover (Friedl and Sulla-Menashe, 2019), $C_4$ vegetation fraction (Luo et al., 2024), and four climate variables from TerraClimate (Abatzoglou et al., 2018) – annual precipitation, soil moisture, maximum temperature, and vapor pressure deficit. We averaged all vegetation and climate data over 2001–2019, the long-term window relevant to how signals integrate into sediments. Section S2.1.4 gives the extraction methods and data specifications in full.

At each sample site, we calculated distance-weighted averages of the raster data with exponential decay kernels at nine spatial scales (1, 3, 5, 10, 20, 40, 70, 100, 150 km). Averaging over nearby grid cells allowed estimation of environmental values for sample locations that fall outside the terrestrial raster coverage, such as for near-offshore sediment samples. Without this approach, many marine sediment samples that sit just beyond raster boundaries would be excluded. Working across scales also reveals the characteristic scale at which environmental signals integrate into sedimentary leaf waxes.

### *2.2. Exploratory Data Analysis and Variable Selection*

We began by examining the geographic structure of the data and finding collinear predictors. Residuals from a simple OLS regression of $\delta^2\mathrm{H}_{\mathrm{wax}}$ on $\delta^2 H^{\mathrm{OIPC}}_{\mathrm{precip}}$ were significantly spatially autocorrelated (Moran's I = 0.58, $p < 0.001$) (Moran, 1950), and they departed from the global relationship in a region-by-region pattern (Section S2.2.1). That structure is what motivated the modeling approach below.

To check for multicollinearity among environmental predictors we used variance inflation factors (VIF; O'Brien, 2007) together with correlation analysis. Several climate variables were strongly correlated ($|r| > 0.7$): maximum temperature with vapor pressure deficit (r = 0.80), $\delta^2 H^{\mathrm{OIPC}}_{\mathrm{precip}}$ with both of these (r = 0.77 to 0.85), and annual precipitation with soil moisture (r = 0.85). VIF screening (threshold = 5) (James et al., 2013), weighed against ecological relevance, led us to keep $\delta^2 H^{\mathrm{OIPC}}_{\mathrm{precip}}$, elevation, $C_4$ fraction, and plant functional types as primary predictors and to drop the redundant climate variables from our main models (Section S2.2.2).

### *2.3. Statistical Modeling Framework*

Our model for sedimentary $\delta^2\mathrm{H}_{\mathrm{wax}}$ is a hierarchical Bayesian framework (Gelman et al., 2013) built to carry multiple sources of variation and uncertainty. Two quantities are kept separate throughout: $\delta^2\mathrm{H}_{\mathrm{precip}}$, the latent precipitation hydrogen-isotope value at a site that the calibration slope acts on and that the inversion reconstructs, and $\delta^2 H^{\mathrm{OIPC}}_{\mathrm{precip}}$, the observed OIPC raster value used as an errors-in-variables predictor with its associated standard error. The model relates $\delta^2\mathrm{H}_{\mathrm{wax}}$ to environmental predictors as:

$$\delta^2 H_{wax,i} \sim \mathcal{N}\left(\mu_i,\, \sigma^2_{\mathrm{measurement},i} + \sigma^2\right) \tag{1}$$

where $\mu_i$ is the linear predictor at site $i$, $\sigma^2_{\mathrm{measurement},i}$ is the per-site analytical variance, reported where available and otherwise assigned as described in Section S2.1.2; after assignment, it is treated as known. $\sigma^2$ is the residual variance estimated from the data. Uncertainty in the OIPC predictor $\delta^2 H^{\mathrm{OIPC}}_{\mathrm{precip},i}$ enters as an errors-in-variables term: the latent value $\delta^2 H_{\mathrm{precip},i}$ at site $i$ is sampled with variance $\sigma^2_{\mathrm{OIPC},i}$ around the OIPC point estimate, and that latent value is propagated through $\mu_i$ (Section S2.3.4).

The mean function $\mu_i$ includes both spatially varying and globally fixed components:

$$\begin{aligned}\mu_i = \beta_0(s_i) + \beta_{\delta^2\mathrm{H}_p}(s_i) \cdot \delta^2\mathrm{H}_{\mathrm{precip},i} + f_{\mathrm{elev}}(\mathrm{elevation}_i) + \beta_{\mathrm{C4}} \cdot \mathrm{C4}_i \\ + \beta_{\mathrm{precip}} \cdot \mathrm{precip}_i + \beta_{\mathrm{PFT}} \cdot \mathrm{PFT}_i + \text{interaction terms}\end{aligned} \tag{2}$$

The global fixed effects describe the mean influence of:

- Elevation: modeled using B-splines with nine interior knots (Wood, 2017) to capture potential nonlinear patterns without imposing a specific functional form
- $C_4$ vegetation fraction: a linear effect representing the enrichment in $C_4$-dominated ecosystems
- Plant functional types: separate coefficients for tree, shrub, and grass fractions
- Interactions: $\delta^2H_{precip}$ × vegetation terms testing whether isotopic fractionation varies systematically among plant types.

We explicitly modeled three sources of uncertainty. First, analytical uncertainty in $\delta^2H_{wax}$ measurements was taken from the source studies where available or otherwise assigned before model fitting. Second, uncertainty in the OIPC predictor $\delta^2 H^{OIPC}_{precip}$ was drawn from the OIPC uncertainty raster and treated as errors-in-variables relating the observed OIPC value to the latent $\delta^2H_{precip}$ entering the regression. Third, residual variation $\sigma^2$ captures micro-scale spatial structure and unexplained variance, estimated from the data. Each uncertainty was propagated into predictions (Section S2.3.4).

The spatially varying coefficients $\beta_0(s_i)$ and $\beta_{\delta^2H_p}(s_i)$ allow slope and intercept of the $\delta^2H_{wax}$ response to $\delta^2H_{precip}$ to vary geographically, as described in the following section.

### *2.4. Spatial Modeling Framework*

To capture geographic variation in the $\delta^2H_{wax}$-$\delta^2H_{precip}$ relationship not represented by the environmental predictors, we added spatially varying coefficients to the hierarchical Bayesian framework. Nearby sites share unmeasured influences that produce spatial autocorrelation in the residuals.

The model decomposes the observed $\delta^2H_{wax}$ signal into three components:

$$\delta^2H_{wax} = \text{Fixed effects} + \text{Spatial field} + \text{Residual variation} \quad (3)$$

The fixed effects include the global relationships with $\delta^2H_{precip}$, elevation, vegetation, and their interactions. The spatial field captures smooth geographic variation in both the intercept ($\beta_0$) and the slope ($\beta_{\delta^2H_p}$), allowing these parameters to vary continuously across Earth's surface. The residual variation represents local-scale variability and measurement error.

We modeled spatial patterns using an approximation of a Gaussian process based on Matérn kernels (Banerjee et al., 2008, 2025), which describe how similarity between locations changes as a function of distance (Supplementary Section 2.4). In this model, locations that are geographically close to each other tend to have more similar values than distant locations. We modeled the intercept $\beta_0(s)$ and slope $\beta_{\delta^2H_p}(s)$ with independent spatial bases, so each could vary across space in its own way. This allows the $\delta^2H_{wax}$-$\delta^2H_{precip}$ relationship to vary by region while still changing smoothly across space.

A length scale parameter ($\rho$) controls the spatial correlation structure, describing how correlations decay with distance. Two sites much closer together than $\rho$ share similar parameter values; two sites farther apart than $\rho$ are effectively independent. The values of $\rho$ were estimated from the data rather than being fixed in advance.

Fitting the full Gaussian process on a global dataset is computationally intensive, so we used a predictive process approximation (Banerjee et al., 2008; Finley et al., 2009) that projects the GP onto a set of 125 globally distributed knot locations. Computational complexity drops from $O(n^3)$ to approximately $O(nm^2)$, where n = 1,129 observations and m = 125 knots. The knots serve as spatial basis functions, and the spatial field is interpolated from them at any location. We placed the knots for approximately uniform global coverage so that regional patterns are captured even where data are sparse.

Two forms of regularization guard against overfitting in regions with few observations. The first is a set of penalized complexity (PC) priors (Simpson et al., 2017) on the spatial variance hyperparameters, which discourage departures from a non-spatial base model. The second is spatially adaptive regularization on individual knot effects, with prior variance that grows with local data density: prior constraints are stronger where data are sparse and looser where observations are abundant. So the first level governs how much spatial structure matters overall, and the second adapts the strength of regularization to local data density (Heaton et al., 2019). This density-dependent prior scaling on the knot effects makes the fitted spatial component a low-rank predictive-process spatial basis with density-adaptive shrinkage rather than a stationary Gaussian process. The Matérn kernel defines the smooth spatial basis, and the adaptive prior shrinks knot-level deviations more strongly in data-poor regions (Section S2.4).

Pairing environmental predictors with spatial fields lets the model separate process-based relationships from geographic covariation. Take $C_4$ plants: they cluster in warm, dry regions that also tend to have enriched $\delta^2H_{precip}$. A non-spatial model cannot say whether $\delta^2H_{wax}$ variability comes from $C_4$ vegetation directly or from the suite of correlated climate factors (temperature, aridity, precipitation source) that vary together across space. With spatial structure modeled at a length scale estimated from the data, predictor effects can be distinguished from spatially-structured residuals when the two operate at different spatial scales (Paciorek, 2010; Gilbert et al., 2025).

### *2.5. Model Configurations and Comparison*

To weigh the relative importance of spatial structure, environmental predictors, and their interactions, we evaluated 14 model configurations (Table 1). The simplest used $\delta^2H_{precip}$ alone as a predictor; the fullest added spatial effects, elevation, vegetation, and interaction terms.

We compared models with the leave-one-out cross-validation information criterion (LOOIC), which estimates out-of-sample predictive accuracy while accounting for posterior uncertainty (Vehtari et al., 2017); lower LOOIC is better. For in-sample fit we computed Bayesian $R^2$ (Gelman et al., 2019), and we used root mean squared error (RMSE) for a direct performance comparison.

We implemented all models in Stan using Hamiltonian Monte Carlo (Carpenter et al., 2017), running 8 chains of 2,000 to 4,000 iterations (half warmup) depending on model complexity. Convergence was assessed using $\hat{R}$ and bulk effective sample size. All parameters had $\hat{R} \leq 1.011$; 13 of 14 models had $\hat{R} < 1.01$, while *baseline_env* reached 1.011 for one B-spline elevation coefficient. The minimum bulk ESS across all models was 857 (*baseline_env*, non-spatial), and all spatial models had bulk ESS $\geq$ 1,293 (Vehtari et al., 2021).

### *2.6. Model Validation*

We validated the spatial models several ways. The first was regional in-sample performance, with residuals stratified across five geographic regions (Americas, Europe, Africa, Asia, Oceania). The baseline environmental spatial model gave residual RMSE values of 14.4‰ (Americas, n=373), 12.3‰ (Europe, n=30), 11.5‰ (Africa, n=143), 17.4‰ (Asia, n=551), and 15.0‰ (Oceania, n=32), against an overall RMSE of 15.6‰ (Table S3).

To check whether the spatial models captured broad patterns and were not overfitting to local clusters, we examined three diagnostics. First, the estimated GP length scales (3,600–3,950 km) far exceeded the typical data spacing (mean nearest-neighbor distance = 34 km), so the fitted patterns are smooth and continental in scale, not localized interpolation. Second, the effective number of parameters ($p_{eff}$; Spiegelhalter et al., 2002) ranged from 44.0 to 55.0 among the spatial models, 3.9–4.9% of the 1,129 observations, below the level that would suggest overfitting. Third, prediction intervals widened in data-sparse regions without becoming unstable. In *baseline_env_sp*, mean 95% interval width increased from 63.8‰ in dense regions to 66.1‰ in sparse regions, and the intervals in spatial models were narrower than in non-spatial models (~65‰ vs. ~80‰).

Three sets of simulation tests (Section S2.6) were used to evaluate model behavior (Section S2.6):

- *Parameter recovery.* We generated synthetic $\delta^2H_{wax}$ data from the *baseline_veg_sp* model with known slopes, then refit the same model. One scenario used a uniform slope of 0.7; the other used a spatially varying slope with global mean 0.65. In both cases, the simulated spatial intercept was independent of the precipitation-isotope predictor.
- *Confounding stress test.* We repeated the simulation, but forced the spatial intercept to correlate with the precipitation-isotope predictor at controlled levels ($\rho_c$ = 0, 0.3, 0.45, 0.5). The $\rho_c \approx 0.45$ case matches the observed correlation between fitted spatial intercepts and $\delta^2H^{OIPC}_{precip}$ in the real data.
- *Prior sensitivity.* We refit *baseline_veg_sp* to the real data under seven alternative prior choices, varying the prior on the precipitation-isotope slope, the PC prior for $\sigma_{slope}$, and the GP length-scale prior.

The first two tests ask whether the model recovers known slopes under controlled conditions. The third asks whether the real-data slope estimate is sensitive to prior choice. Full designs and results are reported in Section S2.6.

## 3. Results

### *3.1. Model Performance*

Across the 14 model variants (Table 1), spatial models outperformed their non-spatial counterparts on every comparison. This provides strong evidence for spatial structure, and is supported by the OLS residual Moran's I (0.58,

$p < 0.001$; Section S2.2.1), the continental-scale Gaussian-process length scales (3,600–3,950 km, Section S2.4), and the LOOIC (Vehtari et al., 2017). Additional environmental and vegetation predictors added little once the spatial field was included. The LOOIC comparison is pointwise leave-one-out and is informative about interpolation within the observed calibration structure; we did not perform spatially blocked validation, so reported predictive gains should not be read as transferability to entirely unsampled regions.

The best-performing model (*full_interact_sp*), which included spatial effects, elevation, vegetation, and $\delta^2H_{precip}$-vegetation interactions, gave LOOIC = 1,264.7 with $R^2$ = 0.839 and RMSE = 15.5‰. The closely related *full_sp* model gave nearly identical performance (ΔLOOIC = 9.4 ± 8.3, $R^2$ = 0.837, RMSE = 15.5‰). Both improve over the baseline non-spatial model ($R^2$ = 0.697, RMSE = 21.2‰), with a lower prediction error and ~14 percentage-points more variance explained. Adding a spatial Gaussian process alone (*baseline_sp*) accounts for most of this improvement ($R^2$ = 0.829, RMSE = 15.9‰, ΔLOOIC = 42.2 ± 14.2 relative to *full_interact_sp*).

Simpler spatial models performed nearly as well as the most complex variants. The baseline environmental spatial model (*baseline_env_sp*), which includes $\delta^2H_{precip}$, elevation, and precipitation amount, gave $R^2$ = 0.836 and RMSE = 15.6‰ (ΔLOOIC = 12.6 ± 10.0). Vegetation predictors (plant functional types, $C_4$ abundance) and their interactions with $\delta^2H_{precip}$ add only modest improvement in LOOIC beyond the spatial field and basic environmental variables. Even simpler models using only the spatial field and $\delta^2H_{precip}$ (*baseline_sp*: $R^2$ = 0.829, RMSE = 15.9‰) perform nearly as well as models that include detailed vegetation information.

Non-spatial models, regardless of predictor complexity, performed substantially worse than even the simplest spatial model. The full non-spatial model with all predictors ($R^2$ = 0.731, RMSE = 20.0‰, ΔLOOIC = 488.3 ± 42.9) could not match the *baseline_sp* model, which used spatial structure with $\delta^2H_{precip}$ alone. Spatial autocorrelation explains more $\delta^2H_{wax}$ variance than the environmental predictors.

### *3.2. Spatial Confounding of Variables*

The apparent global relationship between $\delta^2H_{wax}$ and $\delta^2H_{precip}$ weakens once we account for spatial autocorrelation. In the baseline non-spatial model (*baseline*), the slope ($\beta_{\delta^2H_p}$) was 0.778 (95% CI: 0.749–0.808; Table 2; Figure 3). The point-value OLS regression in Figure 1 is slightly steeper (0.832), and OLS at the fitted integration scale also resulted in a slope of 0.778 (Figure S4). Introducing a Gaussian process spatial field (*baseline_sp*) reduced the slope to 0.574 (95% CI: 0.473–0.671; Table 2; Figure 3). Adding environmental covariates with the spatial field yielded a slope of 0.528 [0.408, 0.644] in *full_sp* and 0.590 [0.441, 0.737] in *full_interact_sp*. These results show that about a quarter to a third of the non-spatial slope estimate is removed by accounting for spatial autocorrelation, indicating shared spatial structure between the $\delta^2H_{precip}$ predictor and the $\delta^2H_{wax}$ response.

Spatial confounding arises because broad geographic gradients in $\delta^2H_{wax}$ overlap with broad geographic gradients in $\delta^2H_{precip}$. This produces correlations driven by shared geography rather than by the underlying wax–precipitation isotope relationship. The fitted spatial field captured this structure at continental scales, and accounted for 48–57% of total variance across spatial models (Table 3). This was comparable to or exceeded the contribution of all environmental predictors combined. 96–98% of this spatial variance (Table 3) originated from spatially varying intercepts. The posterior-mean spatial intercept has standard deviation 14.2–17.2‰ and ranges from -41 to +48‰ at observation sites and -47 to +52‰ at interpolated locations (Figure 4A). The posterior-mean spatial slope has standard deviation 0.12–0.15 at observation locations, around model-specific global means of 0.53–0.62. The *full_sp* model shown in Figure 4B has an observation-level slope range of approximately 0.27–0.79. The dominance of spatial intercept variance indicates that most of the spatial adjustment reflects regional baseline offsets.

We also tested whether the spatial Gaussian process itself absorbed variance from $\delta^2H^{OIPC}_{precip}$ that should have remained in the fixed-effect slope. This would indicate statistical confounding rather than appropriate variance partitioning. We computed correlations between the posterior mean spatial intercepts at observation locations and the corresponding $\delta^2H^{OIPC}_{precip}$ values. Spatial intercepts correlate with precipitation isotopes at $r$ = 0.39–0.51 across spatial models ($R^2$ = *0.15–0.26*), so 15–26% of spatial variance overlaps with precipitation patterns and 74–85% is independent spatial structure.

### *3.3. Spatial Integration*

The spatial Gaussian process had characteristic length scales of 3,600–3,950 km across model variants, far exceeding the mean nearest-neighbor distance of 34 km and indicating smooth continental-scale residual structure rather than

local interpolation. The spatial integration scale parameter ($\lambda$ = 5.7–6.7 km) closely matches the OIPC grid resolution (~9 km). Despite OIPC values remaining correlated beyond 70 km, model performance did not improve with larger integration radii, so the estimated $\lambda$ is a data-resolution constraint. This pattern holds even in simple OLS regression, where spatial integration improves model fit regardless of modeling approach (Figures S4 and S5).

### *3.4. Environmental Predictors*

Environmental and vegetation predictors had mixed effects once spatial structure was accounted for (Table 4). Elevation effects were small across the full elevation range, and credible intervals were wide (Figure S6). In the *baseline_env_sp* model, $\delta^2H_{wax}$ values changed by less than ~10‰ across the lower-elevation range from sea level to ~1,000 m. The wide credible intervals on elevation coefficients indicate that these effects are poorly constrained by the data, with spatial patterns absorbing much of the systematic elevation signal.

After accounting for $\delta^2H_{precip}$, mean annual precipitation had a small negative relationship with $\delta^2H_{wax}$ in the non-spatial *baseline_env* model ($\beta$ = -0.052 [-0.081, -0.022], standardized). The sign flipped to a small positive effect in the *baseline_env_sp* model ($\beta$ = +0.065 [0.017, 0.113]), which points to partial confounding with the spatial field. Either effect is small in magnitude, but the sign reversal argues against a direct mechanistic interpretation of the precipitation-amount coefficient.

Vegetation predictors keep measurable effects in the spatial models, even though they add little to LOOIC. In *full_sp*, grass cover ($\beta$ = -0.24 [-0.40, -0.08]) and tree cover $\beta$ = -0.21 [-0.41, -0.01]) have negative effects, while the shrub and $C_4$ coefficients are not statistically resolved ($\beta_{shrub}$ = 0.07 [-0.17, 0.31]; $\beta_{C4}$ = 0.05 [-0.03, 0.14]). The *full* (non-spatial) model gives tree, grass, and $C_4$ significant negative effects of larger magnitude, so the spatial field absorbs part of the vegetation signal that non-spatial calibrations attribute to these covariates.

To see whether vegetation modulates the isotopic relationship, we tested plant functional type interactions with $\delta^2H_{precip}$ in *full_interact_sp* (Table 5). Two of the four interaction terms are statistically resolved: $\delta^2H_{precip}$ × tree ($\beta$ = -0.24 [-0.42, -0.06], shallower $\delta^2H_{wax}$–$\delta^2H_{precip}$ slopes in tree-dominated landscapes) and $\delta^2H_{precip}$ × shrub ($\beta$ = +0.27 [+0.11, +0.43], steeper slopes in shrub-dominated landscapes). The other two are not: $\delta^2H_{precip}$ × $C_4$ ($\beta$ = +0.02 [-0.08, +0.12]) and $\delta^2H_{precip}$ × grass ($\beta$ = -0.03 [-0.14, +0.09]). Since *full_interact_sp* improves LOOIC over *full_sp* by only 9.4 ± 8.3 units, the interaction terms are statistically detectable but not decisively preferred for prediction. The detectable interactions match vegetation-specific fractionation differences from plant physiological studies (Smith and Freeman, 2006; McInerney et al., 2011; Sachse et al., 2012; Kahmen et al., 2013), but at the resolution of global compilations the vegetation-mediated slope variation is partly entangled with broader spatial structure.

### *3.5. Simulation tests of model behavior*

Simulations using *baseline_veg_sp* evaluated model behavior under controlled conditions. In scenarios where the spatial intercept was independent of the predictor, the model recovered the simulated slope: a uniform slope of 0.7 was recovered as 0.71 [0.60, 0.82], and a spatially varying slope with global mean 0.65 was recovered as 0.71 [0.59, 0.81]. Both 95% credible intervals contained the simulated values.

When the spatial intercept was instead correlated with $\delta^2H^{OIPC}_{precip}$, as is the case in our real data, the model recovered the simulated slope only at $\rho_c$ = 0 (posterior median 0.51 vs. simulated value 0.46; 95% CI [0.43, 0.61]). At higher correlation levels the recovered slope was biased upward in proportion to $\rho_c$: +0.21 at $\rho_c$ = 0.3, +0.28 at $\rho_c$ = 0.45 (the same $\rho$ as in the real data), and +0.30 at $\rho_c$ = 0.5, with the 95% credible intervals excluding the simulated slope for $\rho_c \geq 0.3$ (Table S4). At $\rho_c$ = 0.45, the value closest to the empirical correlation in the real data, OLS estimated a slope of 0.84 even though the simulated true slope was 0.38. The fitted spatial field reduced this bias but did not remove it: the recovered slope was 0.66. In this simulation, the spatial model removed approximately 40% of the OLS bias, while about 60% remained on the slope.

The prior-sensitivity refits of *baseline_veg_sp* gave similar slopes across all seven prior variants. Posterior medians for $\beta_{\delta^2H_p}$ ranged from 0.614 to 0.638, and the 95% credible intervals almost entirely overlapped (Table S5). This suggests that the slope estimate on the real data is not strongly sensitive to reasonable prior choices. However, the confounding stress test showed that, under a constructed confounding scenario matched to the empirical intercept–OIPC correlation, the model-recovered slope is biased upward, and the bias grows as confounding increases. The spatially adjusted slopes of 0.53–0.62 should therefore be interpreted as less-confounded estimates that may still retain upward bias, rather than as fully corrected slopes.

## 4. Discussion

### *4.1. Spatial confounding inflates the apparent global wax–precipitation relationship*

Regional baselines drive the apparent slope, not a single global fractionation. Once the model accounts for spatial autocorrelation, the non-spatial baseline $\delta^2H_{wax}$–$\delta^2H_{precip}$ slope drops from 0.78 to 0.53–0.62, and regional baselines show shifts of up to ~50‰ (Figure 4A). This pattern resolves a long-standing tension in the literature, where average apparent fractionation factors ($\varepsilon_{app}$) have been treated as quasi-constants even though they systematically vary with aridity, latitude, and temperature (Sachse et al., 2012; Polissar and Freeman, 2010; Douglas et al., 2012; Konecky et al., 2016; Bakkelund et al., 2018). The non-spatial regressions conflate two things: the wax–precipitation isotope relationship itself, and broad regional differences in climate and vegetation. When the spatial field accounts for regional differences, the residual slope is broadly coherent across continents: the observation-level SD is ~0.13 around a global mean of 0.53–0.62.

Spatial confounding occurs when the spatial structure of the predictor variable correlates with other factors that also produce the response (Hodges and Reich, 2010). In a non-spatial regression of $\delta^2H_{wax}$ on $\delta^2H_{precip}$, regions with similar $\delta^2H_{precip}$ also share hydrological and ecological characteristics. Therefore the regression confounds the underlying relationship with the variance from spatial clustering. Separating these requires a spatial model in both the slope and the intercept.

One challenge in doing this is that adding spatial structure could in principle over-absorb precipitation-related variance. However, that is unlikely in this case. Correlations between posterior-mean spatial intercepts and $\delta^2H^{OIPC}_{precip}$ are moderate (r = 0.39–0.51), leaving 74–85% of the spatial intercept variability independent of the precipitation variability. The spatial variability is mainly expressed by regional baseline differences (observation-level SD = 14.2–17.2‰), with smaller slope variations (observation-level SD = 0.12–0.15). This suggests that the global wax–precipitation slope is broadly similar across the globe, but regional intercepts vary substantially.

Another concern is that the spatial GP could under-absorb precipitation-related spatial confounding. This would leave residual bias in the estimated slope. The simulation tests suggested that this did, in fact, happen in this model. In the graded confounding stress test, the model recovered the correct simulated slope only when the synthetic spatial intercept was independent of $\delta^2H_{precip}$. When that correlation matched the empirical intercept–OIPC correlation, the recovered slope was biased upward by approximately 0.28 relative to the simulated truth. This suggests that the GP is biased in the direction of under-absorbing confounding. This likely occurs because the predictor and the spatial field vary over similar spatial scales, so the model cannot uniquely separate their shared spatial variance, and depends on the prior. The allocation of shared variance between the fixed-effect slope and the spatial field depends partly on the prior structure (Reich et al., 2006; Hodges and Reich, 2010; Paciorek, 2010). This does not negate the hypothesis of spatial confounding, but suggests that our estimate of spatial confounding is a minimum.

Therefore, the spatially adjusted slope of 0.53–0.62 represents only a partial correction to the non-spatial estimate. This supports the interpretation that non-spatial calibrations are spatially confounded, and produce slopes that are too steep because they conflate the precipitation-isotope relationship with broad geographic covariation. The simulations show that even a Gaussian process model cannot unwind all of the confounding. The adjusted slope should therefore be interpreted as a less-confounded regression coefficient, and not as a physical fractionation parameter. Methods that explicitly separate the predictor from the spatial field (restricted spatial regression, Reich et al., 2006; Hanks et al., 2015; Spatial+, Dupont et al., 2022) could reduce the bias even further, but they require a different model structure than the one developed here.

The implications for paleoclimate calibrations depends on the spatial scale. In our model, the spatial intercept varies by ~50‰ over continental distances of ~3,800 km, which helps resolve the differences among published calibrations. Global non-spatial regressions (Sachse et al., 2012; McFarlin et al., 2019) are capturing real patterns, but the slopes are partially dependent on spatially structured covariation rather than only the precipitation-isotope effect. Regional calibrations yield a wide range of slopes (Garcin et al., 2012; Liu and An, 2018; Shanahan et al., 2013; Struck et al., 2020; Feakins et al., 2016; Gaviria-Lugo et al., 2023), consistent with additional regional processes operating at scales smaller than the correlation length estimated here. Distinguishing baseline spatial differences from environmental effects at sub-continental scales will require much denser sampling within regions than is currently available. Future calibration efforts should account for spatial structure explicitly, either through spatial regression models like those developed here or by developing regionally specific calibrations that minimize geographic confounding within more homogeneous climate zones. Both come with caveats about spatial stationarity that are addressed in Section 4.5.

### 4.2. The global slope is unexpectedly low

The spatially adjusted slope ($\beta_{\delta^2H_p} \approx 0.54$ in *baseline_env_sp*, with a 0.53–0.62 range across spatial-model variants; Table 2) is lower than a simple constant-fractionation model would predict. If leaf wax $\delta^2H$ were source-water $\delta^2H$ modified by a single, location-independent apparent fractionation factor of $\varepsilon_{app} \approx -120‰$ for $C_3$ plants (Sachse et al., 2012), the slope should then be about 0.88. So the 0.53–0.62 global slope is best understood as a regression coefficient against an annual-precipitation predictor that tracks the biosynthetic water signal imperfectly, not as a fractionation parameter linking plant source water to leaf waxes.

Annual precipitation $\delta^2H$ is an imperfect proxy for the water used in lipid biosynthesis, and that mismatch can shallow the apparent slope. OIPC is interpolated GNIP weighted-mean annual precipitation, but plants draw on soil or source water that may be seasonally biased, elevation-dependent, catchment-integrated, stored over variable timescales, or modified by evaporation (Tipple et al., 2013; Sachse et al., 2012). Leaf-water enrichment and plant ecology can also add variation in wax $\delta^2H$ depending on humidity, aridity, vegetation type, or other environmental gradients. Those covariate effects enter the data structurally, not as random residual variance. And uncertainty in the OIPC predictor itself – interpolation error, plus the mismatch between sample sites and the source-water areas that actually feed them – can produce regression-dilution-like attenuation that biases the estimated slope toward zero.

The reduced slope is thus consistent with precipitation $\delta^2H$ remaining an important control on leaf wax $\delta^2H$, while also showing that the global calibration slope is a regression coefficient rather than a physical fractionation parameter. It relates wax $\delta^2H$ to an annual precipitation-isotope predictor, and its attenuation comes from source-water mismatch, predictor uncertainty, and additional leaf-water or ecological controls.

### 4.3. Signals integrate over continental scales

The spatial field suggests that there are large regional baseline differences in modern $\delta^2H_{wax}$ calibrations that $\delta^2H_{precip}$, elevation, vegetation, and precipitation amount leave unexplained. In the fitted intercept field, offsets are negative across high-latitude and western North America and positive in western South America, southern Africa, Australia, and parts of central Asia. Europe and eastern Asia are more mixed, and within-region variability is substantial. The patterns are smooth at continental scales, though the length scale itself is best interpreted as a property of the fitted residual field; it is not evidence for a particular physical process.

While variation in the intercept dominates the variation, the slope field also shows interesting features. In *full_sp*, posterior-mean slopes are low over the Tibetan Plateau and interior central Asia and higher south of the Himalaya in the South Asian monsoon domain (Figure 4B). The contrast may mark a real hydroclimatic boundary, with annual precipitation isotopes north of the Himalaya less tightly coupled to plant or catchment source waters because of snowmelt, storage, elevation, and moisture-source effects. This region is densely sampled, topographically complex, and probably subject to high precipitation-isotope interpolation uncertainty, so this pattern is a hypothesis and not than a resolved mechanism.

The causes of these regional baselines and slope differences is unresolved. Possibilities include moisture-source trajectories, moisture recycling, growing-season timing, soil-water residence time, evaporative enrichment, vegetation effects too coarse to capture with global datasets, or some combination of these. The model cannot determine which processes are responsible but rather establishes that their combined effect is spatially coherent and large enough to matter for calibration.

The spatial integration scale for precipitation isotopes ($\lambda$ = 5.7–6.7 km) has a different interpretation. Because it is close to the OIPC grid resolution (0.083°), it likely reflects optimal handling of the gridded predictor rather than a catchment-scale integration. Averaging over several pixels reduces sensitivity to grid-cell assignment when sample locations fall near OIPC pixel boundaries, improving model fit even in non-spatial models ($R^2$ from 0.643 to 0.695). By contrast, the fitted spatial field captures residual spatial structure that remains after the measured predictors have been included.

Site location therefore conditions $\delta^2H_{wax}$ interpretation; the same wax value implies different $\delta^2H_{precip}$ at different regions. The same $\delta^2H_{wax}$ value can imply different $\delta^2H_{precip}$ values depending on regional baseline offset, with differences of up to ~50‰ across the calibration domain. The spatial model improves prediction by estimating these baseline offsets empirically, even without a mechanistic explanation for them. This approach depends on spatial stationarity: if the modern spatial baseline field has changed through time, then reconstruction uncertainty will be larger than the model estimates.

### 4.4. Vegetation effects are partially resolved, but not along $C_3/C_4$ lines

Plant functional type is widely understood to influence $\delta^2H_{wax}$ and may reflect differences in plant physiological factors such as rooting depth, leaf morphology, leaf-water enrichment, and biosynthetic fractionation (Smith and Freeman, 2006; Polissar and Freeman, 2010; Kahmen et al., 2013; Sachse et al., 2012; Konecky et al., 2019; Shanahan et al., 2013). $C_4$ grasses are typically reported to produce waxes enriched by more than 20‰ relative to $C_3$ grasses under similar conditions (Smith and Freeman, 2006). On this basis, PFT fractions and $C_4$ would be predicted to explain a share of global $\delta^2H_{wax}$ variability.

The spatial models partly confirm this prediction. In *full_sp*, grass cover carries a significant negative coefficient ($\beta$ = -0.24 [-0.40, -0.08]) and tree cover a marginal negative coefficient ($\beta$ = -0.21 [-0.41, -0.01]); shrub cover and $C_4$ fraction are not statistically resolved. In *full_interact_sp*, two of four $\delta^2H_{precip} \times$ PFT interactions are statistically resolved: the tree interaction is negative (slope shallower in tree-dominated landscapes; $\beta$ = -0.24 [-0.42, -0.06]) and the shrub interaction is positive (slope steeper in shrub-dominated landscapes; $\beta$ = +0.27 [+0.11, +0.43]). $C_4 \times \delta^2H_{precip}$ and grass $\times \delta^2H_{precip}$ interactions both have credible intervals overlapping zero. The pattern of resolved coefficients does not align with a simple $C_3/C_4$ dichotomy: the PFT signal cuts across woody/herbaceous lines rather than along the photosynthetic-pathway axis.

MODIS-derived PFT fractions integrate over species composition within each grid cell and group plants with different fractionation behavior, so species- or clade-level effects may be averaged into broad vegetation categories. The weak $C_4$ effect may indicate that $C_4$ fraction is not a major control on sedimentary $\delta^2H_{wax}$ at the scale of this compilation. It may also reflect limitations of the predictor: the $C_4$ fraction product (Luo et al., 2024) is coarser (~56 km resolution) than the other covariates, and fine-scale $C_4$ patches that contribute disproportionately to sediment archives may be missed. Spatial confounding adds a further difficulty because warm-arid $C_4$ regions differ from $C_3$ regions in evapotranspiration, soil-water residence time, and seasonal precipitation as well as photosynthetic pathway. These models therefore provide little support for using global $C_4$ fraction as a strong predictor of $\delta^2H_{wax}$.

The interaction model, *full_interact_sp*, improves only modestly on *full_sp* in LOOIC ($\Delta$LOOIC = 9.4 ± 8.3). Although some interaction coefficients are statistically resolved, they add little predictive information at the scale of the global compilation. For reconstruction at an individual site, predictions are therefore unlikely to depend strongly on which of these models is used, e.g. *full_sp*, *full_interact_sp*, or *baseline_env_sp*. PFT differences produce only minor differences in modeled $\delta^2H_{wax}$ once the spatial field and other covariates are included.

### 4.5. Practical Applications

#### 4.5.1. Uncertainty Reduction and Spatial Context

Regional calibrations (Hou et al., 2008; Garcin et al., 2012; Bakkelund et al., 2018; Shanahan et al., 2013; Struck et al., 2020; Feakins et al., 2016) report slopes that differ from our global estimate because these studies capture environmental relationships operating at spatial scales smaller than the ~3,800 km correlation length. Variation in slopes with spatial scale is expected when underlying processes vary spatially (Paciorek, 2010).

Whether to use a regional or global calibration depends on the context of an individual study, but both require uncertainty quantification. Regional calibrations can provide tighter prediction intervals and capture local-scale processes within their calibration area. When spatial autocorrelation exists in the data, however, simple regressions that treat observations as spatially independent underestimate uncertainty and produce prediction intervals that are too narrow.

The global spatial framework is most useful where no regional calibration is available or where the goal is to separate continental baseline offsets from process relationships. By estimating location-specific baselines, the model accounts for offsets of up to ~50‰ that would otherwise be carried as residual variance or folded into non-spatial slopes. It also propagates uncertainty within a Bayesian framework. Compared to non-spatial global regressions, this approach reduces overall prediction RMSE by approximately 25%. Regardless of approach, complete uncertainty propagation requires accounting for analytical measurement uncertainty, calibration parameter uncertainty, and spatial structure. Spatial structure can be addressed either through explicit modeling or by widening prediction intervals in regional extrapolations.

#### 4.5.2. Global model selection for paleoclimate reconstruction

For paleoclimate reconstruction, the modern vegetation and precipitation-amount fields used during calibration may not represent the conditions during deposition. The spatial models without vegetation predictors (*elevation_only_sp*,

*elevation_c4_sp*) perform nearly as well as the full model. For many applications therefore, the spatial-only models without vegetation covariates are much simpler and provide near-equivalent calibration performance.

### *4.5.3. Detecting changes in paleo-hydroclimate*

Interpreting a shift in $\delta^2H_{wax}$ as a change in $\delta^2H_{precip}$ requires separating precipitation-isotope change from calibration uncertainty and from other processes that can alter wax isotopes. The first challenge is statistical: the calibration itself contains residual scatter and slope uncertainty. The second is interpretive: vegetation change, sediment integration, evapotranspiration, source-water seasonality, and related processes can all shift $\delta^2H_{wax}$ even when $\delta^2H_{precip}$ remains unchanged.

The calibration-model residual scatter, $\sigma_{residual}$ (~16‰ for the spatial models), represents unexplained variation in $\delta^2H_{wax}$ around the fitted relationship. When the calibration is inverted to reconstruct $\delta^2H_{precip}$, this uncertainty increases because residual variation in wax space is divided by the calibration slope, and because uncertainty in the slope is also propagated. The resulting uncertainty therefore applies both to isolated reconstructions and to within-record comparisons.

Within a single sedimentary record, however, one major source of uncertainty partly cancels. Assuming spatial stationarity, the spatial intercept is fixed for a given site within each posterior draw, so it contributes the same offset to all samples from that record. When two intervals are compared, this shared intercept drops out. Relative changes within a record are therefore better constrained than absolute reconstructions from isolated measurements. Other sources of uncertainty do not cancel in the same way. Vegetation composition, sediment integration, evapotranspirative regime, and source-water seasonality can all vary through time and remain relevant for interpreting within-record shifts.

For within-record comparisons, the relevant uncertainty is the variance of the difference between two reconstructed intervals. For two single samples with lag-1 residual correlation $\rho_t$ and independent analytical errors, the variance of the difference is

$$\mathrm{Var}(X_1 - X_2) = 2\sigma^2_{\mathrm{residual}}(1 - \rho_t) + 2\sigma^2_{\mathrm{analytical}} \tag{4}$$

(Box et al., 2008). The autocorrelation term applies only to the residual component because analytical measurement error is independent between samples by construction. With $\sigma_{residual} \approx 15.6$‰ and analytical uncertainty of ~3‰, the corresponding 95% threshold for detecting a change in $\delta^2H_{wax}$ is

$$1.96 \times \sqrt{2 \times 15.6^2(1 - \rho_t) + 2 \times 3^2}‰ \tag{5}$$

Converting this to a threshold on $\delta^2H_{precip}$ requires dividing by the local effective slope $\beta_{eff}$. For the global posterior median $\beta_{eff} \approx 0.54$, the threshold increases by approximately a factor of 1.8. For independent samples ($\rho_t = 0$), the resulting 95% threshold for detecting a change in $\delta^2H_{precip}$ is ~81‰ (95% CI 67–105‰). Positive temporal autocorrelation lowers this threshold because adjacent residuals partly cancel. Under the same framework, the threshold decreases to ~58‰ for $\rho_t = 0.5$, ~39‰ for $\rho_t = 0.8$, and ~29‰ for $\rho_t = 0.9$ (Figure 5).

These thresholds describe only the calibration-imposed statistical limits. A separate question is whether the observed wax shift could arise from vegetation change alone. To evaluate this possibility, we compare two vegetation states at a single site while holding $\delta^2H_{precip}$ fixed at the site's calibration-period OIPC value. For each posterior draw $m$, the fitted vegetation-only contrast is

$$\Delta\mu^{(m)}_{\mathrm{veg}} = \mathbf{x}^{(m)\top}_{\mathrm{veg},2}\boldsymbol{\beta}^{(m)}_{\mathrm{veg}} - \mathbf{x}^{(m)\top}_{\mathrm{veg},1}\boldsymbol{\beta}^{(m)}_{\mathrm{veg}} \tag{6}$$

where $\boldsymbol{\beta}^{(m)}_{\mathrm{veg}}$ contains the vegetation-related coefficients for draw $m$, and the vectors $\mathbf{x}^{(m)}_{\mathrm{veg},1}$ and $\mathbf{x}^{(m)}_{\mathrm{veg},2}$ describe the two vegetation states in the same transformed predictor format used by the fitted Stan model. Conceptually, the contrast combines the direct effect of changing vegetation composition with vegetation-dependent changes in the wax–precipitation slope.

Repeating the calculation across posterior draws gives the range of wax-isotope shifts expected from vegetation change alone. If the observed $\delta^2H_{wax}$ shift exceeds this vegetation-only range, then the specified vegetation change cannot explain the record by itself. However, this does not uniquely identify precipitation isotopes as the cause. The

additional signal could still reflect sediment-source change, source-water seasonality, evapotranspirative enrichment, depositional processes, or other record-specific effects.

Both the detection-threshold calculation and the vegetation-envelope test rely on stationarity assumptions that the global calibration itself cannot supply. The temporal autocorrelation $\rho_t$ must be estimated from the record being analyzed, and the local effective slope $\beta_{\text{eff}}$ is inherited from the modern calibration. Applying that slope to paleo intervals implicitly assumes that the relevant controls on wax formation and sediment integration remained sufficiently stable through time. Alternatively, the one could replace the modeled slope with a slope supported by independent record-specific evidence. Either choice becomes part of the interpretation itself and should be stated explicitly.

#### *4.5.4. Implementation and uncertainty propagation*

The accompanying R package `leafwax` implements a posterior predictive inversion of the calibration to reconstruct $\delta^2\text{H}_{\text{precip}}$ from $\delta^2\text{H}_{\text{wax}}$ measurements using the global calibration described in this paper. Per posterior draw, the package solves the forward model for the $\delta^2\text{H}_{\text{precip}}$ value consistent with the observed wax measurement. No informative prior on $\delta^2\text{H}_{\text{precip}}$ is imposed beyond the implicit support set by the calibration posterior and the OIPC range. The package returns full posterior distributions that propagate analytical measurement error, spatial uncertainty in site-specific effects, residual variance after accounting for predictors, and uncertainty in the global regression parameters. The posterior distributions support probabilistic inference. Users can compute the probability that $\delta^2\text{H}_{\text{precip}}$ exceeds any threshold of interest or that changes between time periods are meaningful (Figure 5). Because residual spatial confounding can leave the spatially adjusted slope too high (Section 4.1), absolute reconstructed magnitudes should be interpreted cautiously; the package is therefore most useful for propagating relative uncertainties between time intervals within a record, or between sites. It is not recommended for absolute reconstructions.

The `leafwax` package can be paired with Bayesian change-point tools such as `bcp` (Erdman and Emerson, 2007) or `Rbeast` (Zhao et al., 2019) for complementary change-point or trend analysis. These tools answer a different question and do not estimate the lag-1 autocorrelation $\rho_t$ used in the threshold formula; the Figure 5 thresholds reflect the calibration-imposed limit.

#### *4.5.5. Quantifying confidence in change detection*

Leaf wax paleoclimate reconstruction is an inverse problem. A shift in $\delta^2\text{H}_{\text{wax}}$ can mark a change in $\delta^2\text{H}_{\text{precip}}$, but it can equally follow from changes in vegetation composition, evapotranspiration, soil-water dynamics, plant water uptake, or sedimentary integration. Several of those controls are themselves climate-sensitive, so interpreting a wax-isotope shift as driven by precipitation isotopes alone requires independent constraints or stationarity assumptions.

These results help define the limits of that interpretation. Across the calibration domain, the $\delta^2\text{H}_{\text{wax}}$–$\delta^2\text{H}_{\text{precip}}$ slope is broadly coherent, so precipitation isotopes are an important control on wax isotopes. But regional baseline offsets are large: the interpolated spatial intercept field ranges from -47 to +52‰. This makes any attempt to assign an absolute $\delta^2\text{H}_{\text{precip}}$ value from a single wax measurement highly uncertain. Most paleoreconstructions instead compare changes within a sedimentary record. In that case, the fixed spatial intercept cancels when two intervals are compared, so relative changes within a record are better constrained than absolute reconstructed values.

The remaining uncertainty depends on whether the non-precipitation controls on $\delta^2\text{H}_{\text{wax}}$ stay approximately stable, or can be independently modeled. When a $\delta^2\text{H}_{\text{wax}}$ shift is small, this distinction is critical: the same signal may be consistent with a precipitation-isotope change, a change in vegetation, a change in source-water seasonality, or some combination of processes. The calibration can quantify the confidence with which a $\delta^2\text{H}_{\text{precip}}$ change can be inferred, since a wax-isotope shift is not necessarily a direct precipitation-isotope signal.

#### *4.5.6. A taxonomy of leaf-wax-based hydroclimate claims*

Different kinds of claims can be made from leaf-wax isotope records, and they do not all require the same level of evidence. We propose four levels of interpretation, ordered from most to least defensible.

*Level 1: a $\delta^2H_{wax}$ shift occurred between two intervals.* This is a measurement-level claim. It is supported when the observed wax contrast exceeds analytical uncertainty. For two single samples with equal analytical uncertainty $\sigma_{\text{analytical}}$, the analytical-noise threshold is $z_{\alpha/2}\,\sqrt{2}\,\sigma_{\text{analytical}}$. The lag-1 autocorrelation $\rho_t$ does not enter because analytical measurement error is independent between samples by construction. For comparisons between interval means rather than single samples, the analytical uncertainty must be propagated from the covariance structure of the included measurements. No climatic or ecological interpretation is required at Level 1.

*Level 2: the wax shift is consistent with a directional hydroclimate change.* This requires evidence that the shift is unlikely to result from sediment-source change or depositional artifact. It also requires either: (a) independent evidence against vegetation reorganization (for example biomarker or pollen evidence for vegetation stability), or (b) demonstration that the observed wax shift exceeds the vegetation-only envelope predicted from a specified PFT-change scenario (Section 4.5.3). The `leafwax` R package implements both approaches, but the user remains responsible for defending the supporting evidence or vegetation scenario.

*Level 3: the wax shift implies a quantitative $\delta^2H_{precip}$ change.* This requires a specified and justified local effective slope, explicit uncertainty propagation through the inversion, and a posterior-probability test that the reconstructed magnitude exceeds the claimed threshold at the stated confidence level (Section S4.1). The `leafwax` package provides the inversion framework for this calculation.

*Level 4: the reconstructed magnitude is uniquely attributable to precipitation-isotope change.* This excludes alternative explanations such as vegetation change, source-water seasonality, or evapotranspirative enrichment. Achieving this level requires independent evidence that these non-precipitation controls remained approximately stationary through the interval being reconstructed.

The calibration framework directly supports Levels 1 and 2. Levels 3 and 4 require additional assumptions and record-specific evidence, as discussed in Sections 4.5.3 and 4.5.5.

### *4.6. Limitations and future directions*

Testing spatial stationarity through time requires records with independent constraints on $\delta^2H_{precip}$, which are often impractical to obtain. Speleothem fluid inclusions or ice cores could provide such constraints, if they could be paired with coeval leaf-wax records across major climate transitions. This would allow testing of whether slopes, intercepts, or spatial structure change systematically through time.

The global environmental datasets used in this study are relatively coarse. The $C_4$ vegetation product has 56 km resolution, plant functional types are resolved at ~9 km, and precipitation isotopes are interpolated from sparse observations. This spatial resolution may miss ecologically important local heterogeneity, especially in mountainous or topographically complex regions. Higher-resolution environmental datasets could improve calibration precision and help separate biological from climatic effects. Recent land-cover products derived from Sentinel-2 imagery and deep learning reach ~10 m resolution (Karra et al., 2021), much finer than the MODIS-derived vegetation products used here. These datasets do not yet have the multi-decadal coverage needed to characterize long-term vegetation patterns. Future calibrations that combine higher-resolution vegetation data with temporally dynamic precipitation-isotope models (Yoshimura et al., 2008) may better constrain seasonal integration effects and local vegetation influences.

## 5. Conclusions

The fitted spatial field accounts for 48–57% of variance in $\delta^2H_{wax}$, with characteristic length scales of ~3,600–3,950 km. These values are model-based variance partitions, not unique physical decompositions. Adding spatial structure reduces the non-spatial baseline slope from 0.78 to 0.53–0.62, indicating that much of the conventional global slope reflects shared spatial structure rather than only the wax–precipitation isotope relationship. This confounding occurs because broad geographic gradients in $\delta^2H_{wax}$ overlap with broad gradients in $\delta^2H_{precip}$.

The spatial field explains as much variance as all environmental predictors combined. Some vegetation effects remain statistically resolved after spatial adjustment: grass and tree cover have negative coefficients in *full_sp*, and the $\delta^2H_{precip}$×tree and ×shrub interactions are resolved in *full_interact_sp*. However, the pattern does not follow a simple $C_3/C_4$ distinction. Spatial intercepts dominate the regional signal, with an observation-level SD of 14.2–17.2‰ and an interpolated field range of -47 to +52‰. Slope variation is smaller but still detectable, with an observation-level SD of 0.12–0.15 and a range of 0.27–0.79 in *full_sp*. Thus, the fitted wax–precipitation isotope relationship varies modestly across regions, while regional hydrological and ecological processes produce large baseline offsets in $\delta^2H_{wax}$.

For paleoclimate applications, the spatial models reduce prediction RMSE for $\delta^2H_{wax}$ by approximately 25% relative to conventional regressions (from ~21‰ to ~16‰). These improvements are interpolation-oriented and do not establish transferability to entirely unsampled regions, which would require spatially blocked validation. Inverting the calibration to reconstruct $\delta^2H_{precip}$ substantially increases uncertainty because residual variation in wax space is

divided by the calibration slope and because slope uncertainty is propagated through the inversion. The posterior SD for a single-point reconstruction is ~29‰ (95% CI 24–38‰), conditional on the fitted spatial structure. Absolute reconstruction uncertainty is larger because it also includes uncertainty in spatial intercepts, environmental covariates, and possible non-stationarity. The resulting detection thresholds are therefore large: for two independent samples, the 95% threshold for detecting a change in $\delta^2H_{precip}$ is ~81‰ (95% CI 67–105‰). For within-record contrasts, positive residual autocorrelation lowers this threshold because adjacent residuals partly cancel: the threshold is ~58‰ for $\rho_t = 0.5$ (48–76‰), ~39‰ for $\rho_t = 0.8$ (32–50‰), and ~29‰ for $\rho_t = 0.9$ (24–38‰). These values should be interpreted as lower bounds under the fitted spatial model. Residual confounding not fully absorbed by the fitted spatial field (Section 4.1; Section S2.6) would make $\sigma_{residual}$ too low and the corresponding thresholds too small. The within-record thresholds are also record-specific because they depend on $\rho_t$ and on the local effective slope assumed for the site (Sections 4.5.3 and 4.5.5). The `leafwax` R package implements these spatial calibrations and returns full posterior distributions for paleoclimate reconstruction.


## Acknowledgments

The author acknowledges support from a block grant from the Taylor Geospatial Institute. Washington University provided support from the Geospatial Research Initiative and from the Department of Earth, Environmental, and Planetary Sciences through support of the Fossett Laboratory. Discussions with Bronwen Konecky, Jack Hutchings, and Joe Guinness helped clarify the statistical and interpretive aspects of this work.


## Declaration of generative AI and AI-assisted technologies in the writing process

During the preparation of this work the author used Claude Sonnet to check internal consistency of numerical values, notation, and cross-references, and to assist with copy-editing and language refinement. After using this tool, the author reviewed and edited the content as needed and takes full responsibility for the content of the publication.

## Data Availability

The code and data products supporting this study are versioned in GitHub and archived on Zenodo. The spatial-model code is available at `https://doi.org/10.5281/zenodo.20172575`. The accompanying `leafwax` R package, which implements the Bayesian inversion of the calibration for paleoclimate reconstruction, is available at `https://doi.org/10.5281/zenodo.20172570` and on CRAN. The posterior draws from all 14 fitted models are archived as *leafwax v10 model posteriors* at `https://doi.org/10.5281/zenodo.20085465`.

## Appendix A. Supplementary Materials

The supplementary material provides additional methodological details for the Bayesian spatial models used in this study. It includes full descriptions of the model design, data processing steps, and prior specifications.

Abatzoglou, J. T., Dobrowski, S. Z., Parks, S. A., Hegewisch, K. C., 2018. Terraclimate, a high-resolution global dataset of monthly climate and climatic water balance from 1958-2015. Sci. Data. 5, 170191.

Amatulli, G., Domisch, S., Tuanmu, M.-N., Parmentier, B., Ranipeta, A., Malczyk, J., Jetz, W., 2018. A suite of global, cross-scale topographic variables for environmental and biodiversity modeling.

Bakkelund, A., Porter, T. J., Froese, D. G., Feakins, S. J., 2018. Net fractionation of hydrogen isotopes in n-alkanoic acids from soils in the northern boreal forest. Org. Geochem. 125, 1–13.

Banerjee, S., Gelfand, A. E., Carlin, B. P., 2025. Hierarchical Modeling and Analysis for Spatial Data, 3rd Edition. Chapman & Hall/CRC, Boca Raton, FL.

Banerjee, S., Gelfand, A. E., Finley, A. O., Sang, H., 2008. Gaussian predictive process models for large spatial data sets. J. R. Stat. Soc. Series B Stat. Methodol. 70, 825–848.

Bowen, G. J., 2008. Spatial analysis of the intra-annual variation of precipitation isotope ratios and its climatological corollaries: precipitation isotopic seasonality. J. Geophys. Res. 113.

Bowen, G. J., 2018. Gridded maps of the isotopic composition of meteoric waters. Online Isotopes in Precipitation Calculator, version 3.1. URL `http://www.waterisotopes.org`

Bowen, G. J., Cai, Z., Fiorella, R. P., Putman, A. L., 2019. Isotopes in the water cycle: Regional- to global-scale patterns and applications. Annu. Rev. Earth Planet. Sci. 47, 453–479.

Bowen, G. J., Revenaugh, J., 2003. Interpolating the isotopic composition of modern meteoric precipitation. Water Resour. Res. 39, 1–13.

Box, G. E. P., Jenkins, G. M., Reinsel, G. C., 2008. Time series analysis, 4th Edition. John Wiley & Sons, Hoboken, NJ.

Carpenter, B., Gelman, A., Hoffman, M. D., Lee, D., Goodrich, B., Betancourt, M., Brubaker, M. A., Guo, J., Li, P., Riddell, A., 2017. Stan: A probabilistic programming language. J. Stat. Softw. 76.

Cernusak, L. A., Barbour, M. M., Arndt, S. K., Cheesman, A. W., English, N. B., Feild, T. S., Helliker, B. R., Holloway-Phillips, M. M., Holtum, J. A. M., Kahmen, A., McInerney, F. A., Munksgaard, N. C., Simonin, K. A., Song, X., Stuart-Williams, H., West, J. B., Farquhar, G. D., 2016. Stable isotopes in leaf water of terrestrial plants. Plant Cell Environ. 39, 1087–1102.

Corcoran, M. C., Diefendorf, A. F., Lowell, T. V., Hall, B. L., Spoth, M. M., Schartman, A., Brickle, P., 2022. Hydrogen and carbon isotope fractionation in modern plant wax n-alkanes from the falkland islands. Org. Geochem. 166, 104404.

Daniels, W. C., Russell, J. M., Morrill, C., Longo, W. M., Giblin, A. E., Holland-Stergar, P., Welker, J. M., Wen, X., Hu, A., Huang, Y., 2021. Lacustrine leaf wax hydrogen isotopes indicate strong regional climate feedbacks in beringia since the last ice age. Quat. Sci. Rev. 269, 107130.

Douglas, P. M. J., Pagani, M., Brenner, M., Hodell, D. A., Curtis, J. H., 2012. Aridity and vegetation composition are important determinants of leaf-wax $\delta$d values in southeastern mexico and central america. Geochim. Cosmochim. Acta. 97, 24–45.

Dupont, E., Wood, S. N., Augustin, N. H., 2022. Spatial+: A novel approach to spatial confounding. Biometrics 78, 1279–1290.

Erdman, C., Emerson, J. W., 2007. bcp: An r package for performing a bayesian analysis of change point problems. Journal of Statistical Software 23.

Evans, M. N., Tolwinski-Ward, S. E., Thompson, D. M., Anchukaitis, K. J., 2013. Applications of proxy system modeling in high resolution paleoclimatology. Quat. Sci. Rev. 76, 16–28.

Feakins, S. J., Bentley, L. P., Salinas, N., Shenkin, A., Blonder, B., Goldsmith, G. R., Ponton, C., Arvin, L. J., Wu, M. S., Peters, T., West, A. J., Martin, R. E., Enquist, B. J., Asner, G. P., Malhi, Y., 2016. Plant leaf wax biomarkers capture gradients in hydrogen isotopes of precipitation from the andes and amazon. Geochim. Cosmochim. Acta. 182, 155–172.

Finley, A. O., Sang, H., Banerjee, S., Gelfand, A. E., 2009. Improving the performance of predictive process modeling for large datasets. Comput. Stat. Data Anal. 53, 2873–2884.

Friedl, M., Sulla-Menashe, D., 2019. MCD12Q1 MODIS/Terra+Aqua Land Cover Type Yearly L3 Global 500m SIN Grid V006. NASA EOSDIS Land Processes Distributed Active Archive Center.

Galy, V., Eglinton, T., 2011. Protracted storage of biospheric carbon in the ganges – brahmaputra basin. Nat. Geosci. 4, 1–5.

Gamarra, B., Sachse, D., Kahmen, A., 2016. Effects of leaf water evaporative $^2$h-enrichment and biosynthetic fractionation on leaf wax n-alkane $\delta^2$h values in c3 and c4 grasses. Plant Cell Environ. 39, 2390–2403.

Garcin, Y., Schwab, V. F., Gleixner, G., Kahmen, A., Todou, G., Séné, O., Onana, J.-M., Achoundong, G., Sachse, D., 2012. Hydrogen isotope ratios of lacustrine sedimentary n-alkanes as proxies of tropical african hydrology: Insights from a calibration transect across cameroon. Geochim. Cosmochim. Acta. 79, 106–126.

Gaviria-Lugo, N., Läuchli, C., Wittmann, H., Bernhard, A., Frings, P., Mohtadi, M., Rach, O., Sachse, D., 2023. Climatic controls on leaf wax hydrogen isotope ratios in terrestrial and marine sediments along a hyperarid-to-humid gradient. Biogeosciences 20, 4433–4453.

Gelman, A., Carlin, J. B., Stern, H. S., Dunson, D. B., Vehtari, A., Rubin, D. B., 2013. Bayesian Data Analysis, 3rd Edition. Chapman & Hall/CRC, Philadelphia, PA.

Gelman, A., Goodrich, B., Gabry, J., Vehtari, A., 2019. R-squared for bayesian regression models. Am. Stat. 73, 307–309.

Gilbert, B., Ogburn, E. L., Datta, A., 2025. Consistency of common spatial estimators under spatial confounding. Biometrika 112 (2), asae070.

Goldsmith, G. R., Allen, S. T., Braun, S., Engbersen, N., González-Quijano, C. R., Kirchner, J. W., Siegwolf, R. T. W., 2018. Spatial variation in throughfall, soil, and plant water isotopes in a temperate forest. Ecohydrology, e2059.

Hanks, E. M., Schliep, E. M., Hooten, M. B., Hoeting, J. A., 2015. Restricted spatial regression in practice: geostatistical models, confounding, and robustness under model misspecification. Environmetrics 26, 243–254.

Heaton, M. J., Datta, A., Finley, A. O., Furrer, R., Guinness, J., Guhaniyogi, R., Gerber, F., Gramacy, R. B., Hammerling, D., Katzfuss, M., Lindgren, F., Nychka, D. W., Sun, F., Zammit-Mangion, A., 2019. A case study competition among methods for analyzing large spatial data. J. Agric. Biol. Environ. Stat. 24, 398–425.

Hodges, J. S., Reich, B. J., 2010. Adding spatially-correlated errors can mess up the fixed effect you love. Am. Stat. 64, 325–334.

Hou, J., D'Andrea, W. J., Huang, Y., 2008. Can sedimentary leaf waxes record d/h ratios of continental precipitation? field, model, and experimental assessments. Geochim. Cosmochim. Acta. 72, 3503–3517.

James, G., Witten, D., Hastie, T., Tibshirani, R., 2013. An Introduction to Statistical Learning: with Applications in R. Springer, New York.

Kahmen, A., Hoffmann, B., Schefuß, E., Arndt, S. K., Cernusak, L. a., West, J. B., Sachse, D., 2013. Leaf water deuterium enrichment shapes leaf

wax n-alkane δd values of angiosperm plants II: Observational evidence and global implications. Geochim. Cosmochim. Acta. 111, 50–63.
Karra, K., Kontgis, C., Statman-Weil, Z., Mazzariello, J. C., Mathis, M., Brumby, S. P., 2021. Global land use / land cover with sentinel 2 and deep learning. 2021 IEEE International Geoscience and Remote Sensing Symposium IGARSS.
Konecky, B., Russell, J., Bijaksana, S., 2016. Glacial aridity in central indonesia coeval with intensified monsoon circulation. Earth Planet. Sci. Lett. 437, 15–24.
Konecky, B. L., Dee, S. G., Noone, D. C., 2019. Waxpsm: A forward model of leaf wax hydrogen isotope ratios to bridge proxy and model estimates of past climate. J. Geophys. Res. Biogeosci. 124, 2107–2125.
Liu, J., An, Z., 2018. A hierarchical framework for disentangling different controls on leaf wax δd-alkane values in terrestrial higher plants. Quat. Sci. Rev. 201, 409–417.
Liu, J., An, Z., 2019. Variations in hydrogen isotopic fractionation in higher plants and sediments across different latitudes: Implications for paleohydrological reconstruction. Sci. Total Environ. 650, 470–478.
Liu, W., Yang, H., Li, L., 2006. Hydrogen isotopic compositions of n-alkanes from terrestrial plants correlate with their ecological life forms. Oecologia 150, 330–338.
Luo, X., Zhou, H., Satriawan, T. W., Tian, J., Zhao, R., Keenan, T. F., Griffith, D. M., Sitch, S., Smith, N. G., Still, C. J., 2024. Mapping the global distribution of c4 vegetation using observations and optimality theory. Nat. Commun. 15, 1219.
Martins, G. S., Cordeiro, R. C., Turcq, B., Meyers, P. A., Mendez-Millan, M., Moreira, L. S., Fontes, D., Rodrigues, R. A., Sifeddine, A., Behling, H., Bouloubassi, I. D., 2022. Late quaternary hydrological changes in the southeastern amazon basin from n-alkane molecular and isotopic records in sediments of saci lake, pará state (brazil). Glob. Planet. Change. 213, 103833.
McClelland, H. L. O., Halevy, I., Wolf-Gladrow, D. A., Evans, D., Bradley, A. S., 2021. Statistical uncertainty in paleoclimate proxy reconstructions. Geophys. Res. Lett. 48, 1–11.
McFarlin, J. M., Axford, Y., Masterson, A. L., Osburn, M. R., 2019. Calibration of modern sedimentary $\delta$2h plant wax-water relationships in greenland lakes. Quat. Sci. Rev. 225, 105978.
McInerney, F. A., Helliker, B. R., Freeman, K. H., 2011. Hydrogen isotope ratios of leaf wax n-alkanes in grasses are insensitive to transpiration. Geochim. Cosmochim. Acta. 75, 541–554.
Moran, P. A. P., 1950. Notes on continuous stochastic phenomena. Biometrika 37, 17–23.
National Research Council, 2006. Surface Temperature Reconstructions for the Last 2,000 Years. The National Academies Press, Washington, DC.
O'Brien, R. M., 2007. A caution regarding rules of thumb for variance inflation factors. Qual. Quant. 41, 673–690.
Paciorek, C. J., 2010. The importance of scale for spatial-confounding bias and precision of spatial regression estimators. Stat. Sci. 25, 107–125.
Polissar, P. J., Freeman, K. H., 2010. Effects of aridity and vegetation on plant-wax δd in modern lake sediments. Geochim. Cosmochim. Acta. 74, 5785–5797.
Reich, B. J., Hodges, J. S., Zadnik, V., 2006. Effects of residual smoothing on the posterior of the fixed effects in disease-mapping models. Biometrics 62, 1197–1206.
Sachse, D., Billault, I., Bowen, G. J., Chikaraishi, Y., Dawson, T. E., Feakins, S. J., Freeman, K. H., Magill, C. R., Mcinerney, F. A., Meer, M. T. J. V. D., Polissar, P., Robins, R. J., Sachs, J. P., Schmidt, H.-L., Sessions, A. L., White, J. W. C., West, J. B., 2012. Molecular paleohydrology : Interpreting the hydrogen-isotopic composition of lipid biomarkers from photosynthesizing organisms. Annual Review of Earth and Planetary Sciences 40, 221–252.
Shanahan, T. M., Hughen, K. a., Ampel, L., Sauer, P. E., Fornace, K., 2013. Environmental controls on the 2h/1h values of terrestrial leaf waxes in the eastern canadian arctic. Geochim. Cosmochim. Acta. 119, 286–301.
Simpson, D., Rue, H., Riebler, A., Martins, T. G., Sørbye, S. H., 2017. Penalising model component complexity: A principled, practical approach to constructing priors.
Smith, F. a., Freeman, K. H., 2006. Influence of physiology and climate on δd of leaf wax n-alkanes from c3 and c4 grasses. Geochim. Cosmochim. Acta. 70, 1172–1187.
Spiegelhalter, D. J., Best, N. G., Carlin, B. P., Van Der Linde, A., 2002. Bayesian measures of model complexity and fit. J. R. Stat. Soc. Series B Stat. Methodol. 64, 583–639.
Struck, J., Bliedtner, M., Strobel, P., Bittner, L., Bazarradnaa, E., Andreeva, D., Zech, W., Glaser, B., Zech, M., Zech, R., 2020. Leaf waxes and hemicelluloses in topsoils reflect the $\delta^2$H and $\delta^{18}$O isotopic composition of precipitation in Mongolia. Frontiers in Earth Science 8, 343.
Tierney, J. E., Russell, J. M., Huang, Y., Damsté, J. S. S., Hopmans, E. C., Cohen, A. S., 2008. Northern hemisphere controls on tropical southeast african climate during the past 60,000 years. Science 322, 252–255.
Tingley, M. P., Huybers, P., 2010. A bayesian algorithm for reconstructing climate anomalies in space and time. part i: Development and applications to paleoclimate reconstruction problems. J. Clim. 23, 2759–2781.
Tipple, B. J., Berke, M. A., Doman, C. E., Khachaturyan, S., Ehleringer, J. R., 2013. Leaf-wax n-alkanes record the plant–water environment at leaf flush. Proceedings of the National Academy of Sciences 110 (7), 2659–2664.
Vehtari, A., Gelman, A., Gabry, J., 2017. Practical bayesian model evaluation using leave-one-out cross-validation and WAIC. Stat. Comput. 27, 1413–1432.
Vehtari, A., Gelman, A., Simpson, D., Carpenter, B., Bürkner, P.-C., 2021. Rank-normalization, folding, and localization: An improved r^ for assessing convergence of MCMC (with discussion). Bayesian Anal. 16.
Wood, S. N., 2017. Generalized additive models. Chapman and Hall/CRC, Boca Raton, FL.
Wu, H., Li, X.-Y., Jiang, Z., Chen, H., Zhang, C., Xiao, X., 2016. Contrasting water use pattern of introduced and native plants in an alpine desert ecosystem, northeast qinghai-tibet plateau, china. Sci. Total Environ. 542, 182–191.
Yoshimura, K., Kanamitsu, M., Noone, D., Oki, T., 2008. Historical isotope simulation using reanalysis atmospheric data. J. Geophys. Res. 113.
Zhao, B., Russell, J. M., Blaus, A., de Novaes Nascimento, M., Freeman, A., Bush, M. B., 2024. Tropical andean climate variations since the last deglaciation. Proc. Natl. Acad. Sci. U. S. A. 121, e2320143121.
Zhao, K., Wulder, M. A., Hu, T., Bright, R., Wu, Q., Qin, H., Li, Y., Toman, E., Mallick, B., Zhang, X., Brown, M., 2019. Detecting change-point, trend, and seasonality in satellite time series data to track abrupt changes and nonlinear dynamics: A bayesian ensemble algorithm. Remote Sens. Environ. 232, 111181.

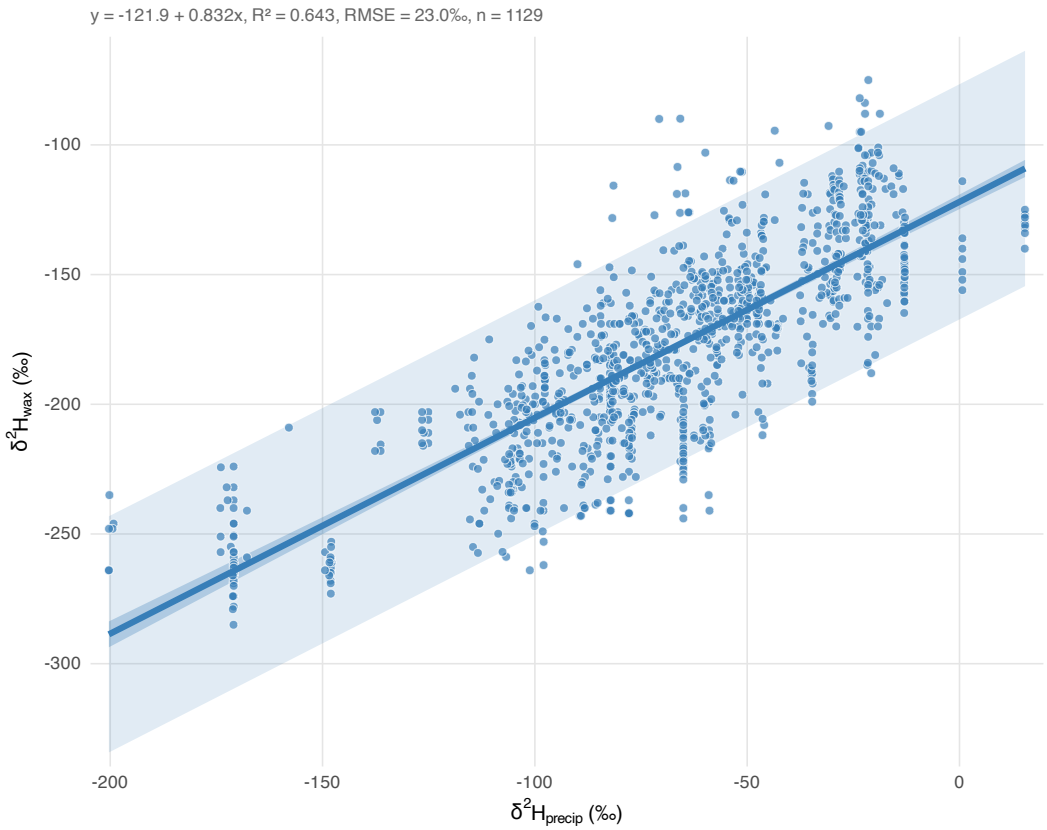


Figure 1: **Global relationship between precipitation and leaf wax hydrogen isotopes.** Ordinary least squares regression of $\delta^2H_{wax}$ against $\delta^2H^{OIPC}_{precip}$ using point values from the OIPC $\delta^2H_{precip}$ field at each sample location (n = 1,129 surface sediment and soil samples). The linear relationship (y = -121.9 + 0.832x) explains 64% of variance ($R^2$ = 0.643, RMSE = 23.0‰). The dark shaded band is the 95% confidence interval on the regression line; the lighter outer band is the 95% prediction interval. The model-comparison baseline uses the fitted spatial-integration version of this predictor, whose slope is 0.778 (Figure S4; Table 2).

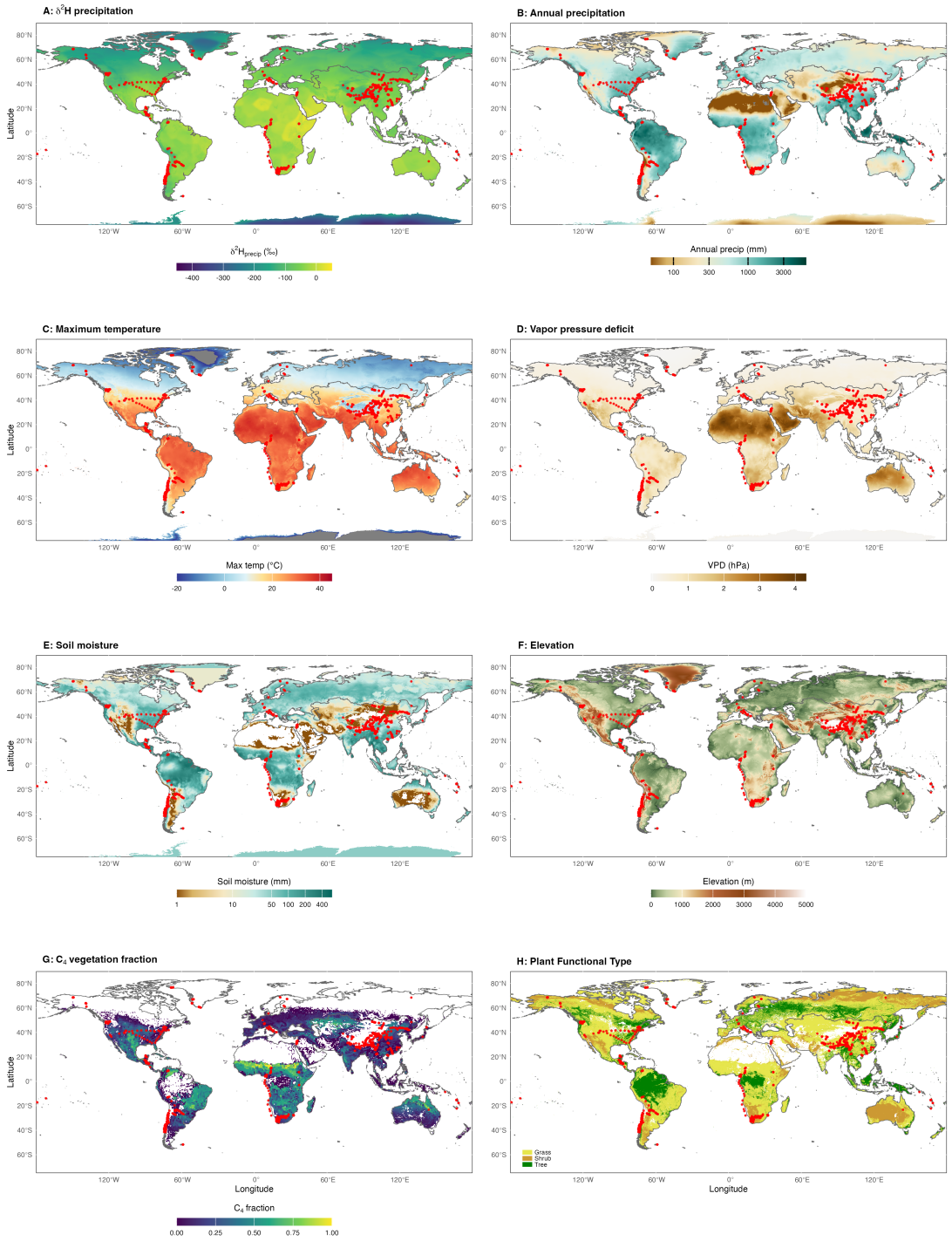


Figure 2: **Global distribution of calibration samples and environmental variables.** (A) $\delta^2H_{precip}$ (OIPC), (B) Annual precipitation, (C) Maximum temperature, (D) Vapor pressure deficit, (E) Soil moisture, (F) Elevation, (G) $C_4$ vegetation fraction, and (H) Plant functional type. Red points show the 1,129 surface sediment and soil sample locations used in this study. Continent outlines (gray) are shown for spatial reference. Environmental data are extracted at sample locations from global gridded datasets (see Methods).

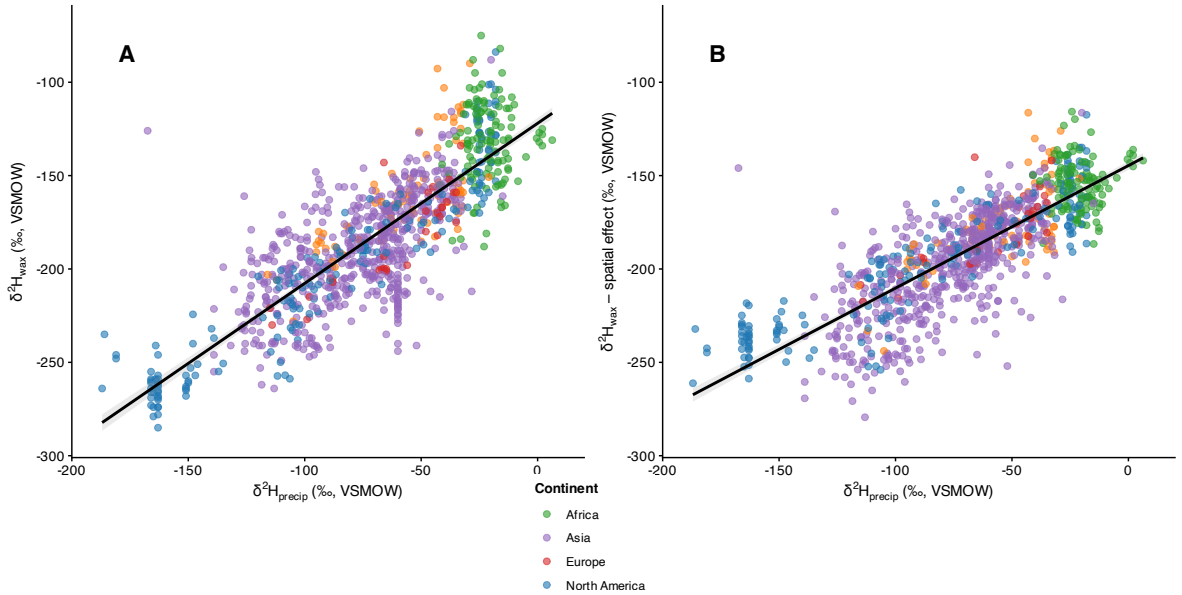


Figure 3: **Spatial confounding inflates the apparent $\delta^2H_{wax}$-$\delta^2H_{precip}$ relationship.** (A) Non-spatial baseline regression using the fitted spatial-integration predictor (slope = 0.78, 95% CI: 0.75–0.81) showing an artificially steep relationship driven by continental-scale geographic covariation. Points are colored by continent, with regional clustering visible. (B) Spatially adjusted regression after removing the fitted Gaussian-process spatial effects from observed $\delta^2H_{wax}$ values. The spatial model yields a flatter relationship (slope = 0.57, 95% CI: 0.48–0.67, from *baseline_sp*), representing a less-confounded isotopic association after accounting for regional baseline offsets.

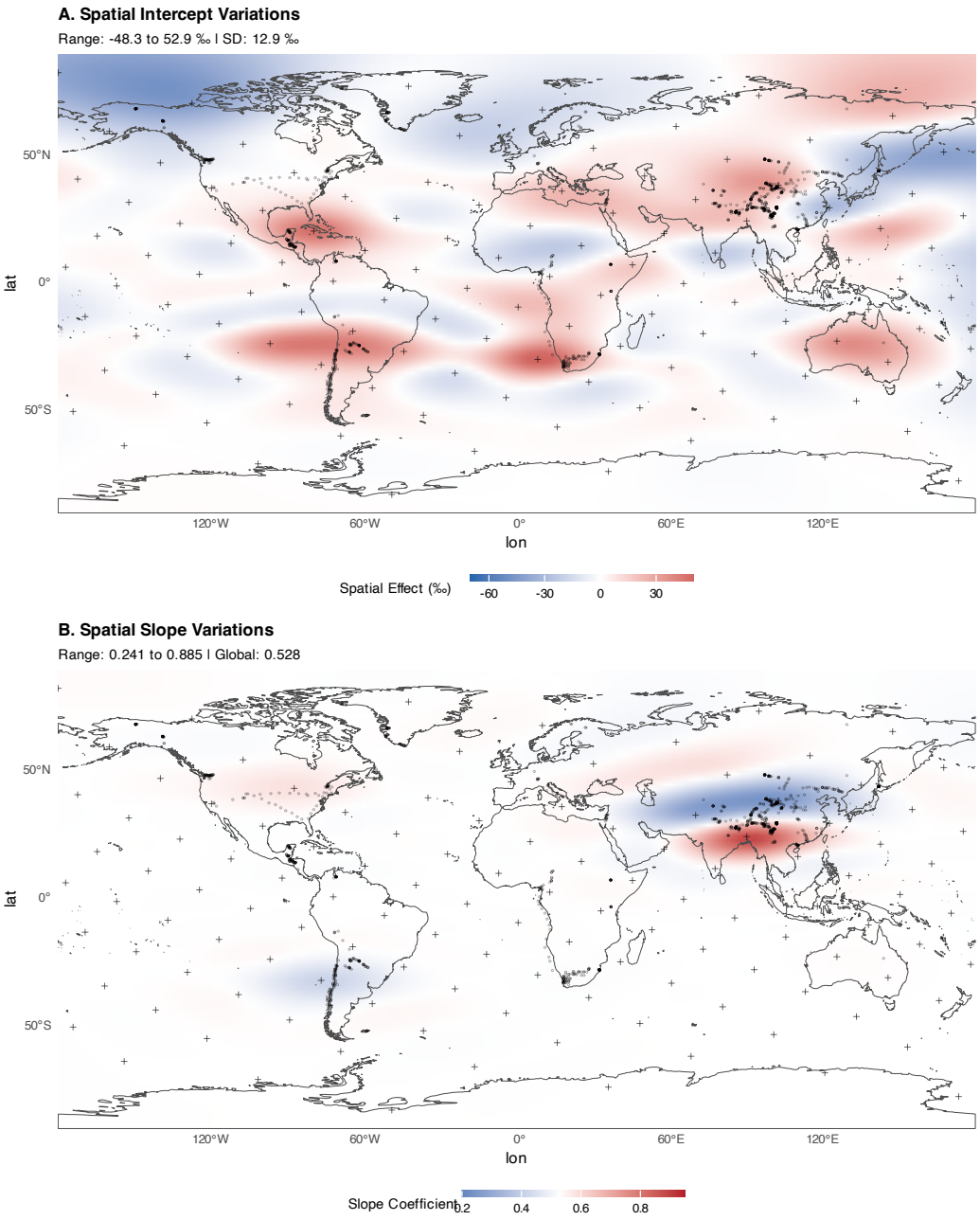


Figure 4: **Geographic patterns of spatially varying model parameters.** Posterior mean estimates from the *full_sp* model showing (A) spatially varying intercepts ($\beta_0$), representing location-specific baseline $\delta^2H_{wax}$ values; the *interpolated field* ranges from approximately -47 to +52‰ globally with a global mean near zero (the field at observation locations alone ranges from -41 to +48‰). (B) Spatially varying slopes ($\beta_{\delta^2H_p}$), representing location-specific sensitivity of $\delta^2H_{wax}$ to $\delta^2H_{precip}$; the field *at observation locations* ranges from approximately 0.27 to 0.79 around a global mean of ~0.53. Black crosses indicate knot locations; colors represent interpolated values between knots.

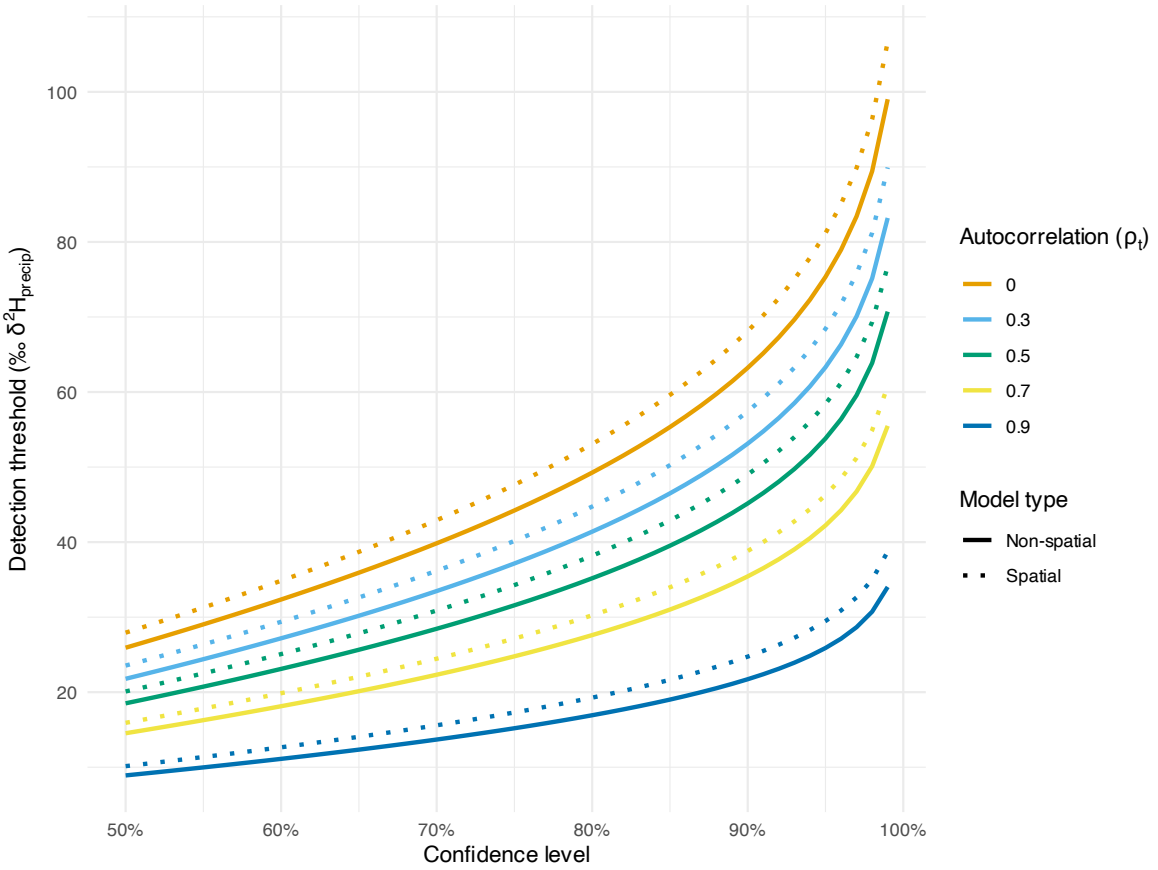


Figure 5: **Detection thresholds for $\delta^2H_{precip}$ change in single sedimentary records.** Minimum detectable change in $\delta^2H_{precip}$ (‰) versus confidence level for varying lag-1 temporal autocorrelation ($\rho_t$). Solid lines: non-spatial baseline model (median $\beta_{\delta^2H_p} = 0.78$, residual $\sigma \approx 21$‰). Dotted lines: spatial *baseline_env_sp* model (median $\beta_{\delta^2H_p} = 0.54$, residual $\sigma \approx 16$‰). Each curve summarizes the posterior median of the per-draw 95% threshold, propagating both residual variance and slope uncertainty (Section 4.5.3 gives the full expression). The non-spatial curves sit slightly below the spatial curves because the non-spatial slope is inflated through unaccounted spatial confounding; the spatial values are the more defensible estimates of the detection threshold. All thresholds are lower bounds under the fitted spatial model; residual confounding not absorbed by the fitted spatial field would shift them upward.

Table 1: Model performance metrics for all candidate models

| Model | Predictors | Max $\hat{R}$ | Min ESS | LOOIC | SE | ΔLOOIC | SE | $p_{\text{eff}}$ | $n_{\text{hi-k}}$ |
|---|---|---|---|---|---|---|---|---|---|
| baseline | $\delta^2H_p$ | 1.004 | 3107 | 1864.7 | 51.7 | 600.0 | 47.7 | 3.2 | 0 |
| baseline_sp | $\delta^2H_p$ + GP | 1.004 | 2206 | 1306.9 | 59.8 | 42.2 | 14.2 | 44.2 | 1 |
| baseline_env | $\delta^2H_p$, elev, precip | 1.011 | 857 | 1775.0 | 53.5 | 510.3 | 42.7 | 11.8 | 0 |
| baseline_env_sp | $\delta^2H_p$, elev, precip + GP | 1.005 | 1319 | 1277.3 | 59.6 | 12.6 | 10.0 | 52.8 | 3 |
| baseline_veg | $\delta^2H_p$, PFT, C4, PFT $\times \delta^2H_p$, C4 $\times \delta^2H_p$ | 1.004 | 2985 | 1748.9 | 52.9 | 484.2 | 45.1 | 9.3 | 0 |
| baseline_veg_sp | $\delta^2H_p$, PFT, C4, PFT $\times \delta^2H_p$, C4 $\times \delta^2H_p$ + GP | 1.004 | 3029 | 1282.7 | 60.0 | 18.0 | 9.4 | 46.4 | 0 |
| full | $\delta^2H_p$, PFT, C4, elev, precip | 1.007 | 1283 | 1753.0 | 53.4 | 488.3 | 42.9 | 15.8 | 0 |
| full_sp | $\delta^2H_p$, PFT, C4, elev, precip + GP | 1.005 | 1293 | 1274.1 | 60.1 | 9.4 | 8.3 | 54.9 | 1 |
| full_interact | $\delta^2H_p$, PFT $\times$ $\delta^2H_p$, C4 $\times$ $\delta^2H_p$, elev, precip | 1.004 | 1541 | 1690.6 | 54.9 | 425.9 | 41.2 | 17.9 | 0 |
| full_interact_sp | $\delta^2H_p$, PFT $\times$ $\delta^2H_p$, C4 $\times$ $\delta^2H_p$, elev, precip + GP | 1.004 | 1669 | 1264.7 | 59.8 | -0.0 | 0.0 | 55.0 | 2 |
| elevation_only_sp | $\delta^2H_p$, elev + GP | 1.004 | 1377 | 1286.3 | 59.2 | 21.6 | 11.0 | 50.7 | 1 |
| elevation_c4_sp | $\delta^2H_p$, elev, C4 + GP | 1.004 | 1388 | 1288.9 | 59.3 | 24.2 | 11.0 | 51.7 | 3 |
| c4_only_sp | $\delta^2H_p$, C4 + GP | 1.003 | 2064 | 1309.4 | 60.0 | 44.6 | 14.6 | 44.0 | 1 |
| elevation_c4_interact_sp | $\delta^2H_p$, C4 $\times \delta^2H_p$, elev + GP | 1.003 | 1661 | 1287.3 | 59.2 | 22.6 | 11.1 | 52.7 | 1 |

*Note:* $\hat{R}$ = Gelman-Rubin convergence diagnostic; ESS = effective sample size; LOOIC = leave-one-out information criterion; SE = standard error; ΔLOOIC reported vs the lowest-LOOIC model; $p_{\text{eff}}$ = effective number of parameters; $n_{\text{hi-k}}$ = count of observations with Pareto-$k > 0.7$; GP = Gaussian process; $\delta^2H_p = \delta^2H_{\text{precip}}$; elev = elevation.

Table 2: Table 2. Global parameter estimates for all models

| Model | RMSE (‰) | $R^2$ | $\beta_0$ (‰) | $\beta_{\delta^2H_p}$ | $\lambda_{int}$ (km) | GP scale (km) | Knot Slope SD | Knot Int. SD (‰) |
|---|---|---|---|---|---|---|---|---|
| baseline | 21.2 | 0.697 | -177.6 [-178.9, -176.4] | 0.778 [0.749, 0.808] | 6.4 [2.6, 13.7] | - | - | - |
| baseline_sp | 15.9 | 0.829 | -185.4 [-193.2, -178.0] | 0.574 [0.473, 0.671] | 5.7 [2.4, 11.8] | 3948 [2387, 6024] | 0.373 | 39.2 |
| baseline_env | 20.3 | 0.724 | -178.0 [-179.3, -176.8] | 0.854 [0.816, 0.891] | 7.8 [3.4, 15.5] | - | - | - |
| baseline_env_sp | 15.6 | 0.836 | -187.5 [-196.2, -179.2] | 0.543 [0.419, 0.662] | 6.2 [2.7, 12.9] | 3836 [2338, 5964] | 0.347 | 42.0 |
| baseline_veg | 20.0 | 0.730 | -167.4 [-174.8, -160.0] | 0.699 [0.597, 0.800] | 7.9 [3.0, 18.5] | - | - | - |
| baseline_veg_sp | 15.7 | 0.834 | -177.6 [-187.5, -167.9] | 0.623 [0.497, 0.751] | 6.5 [2.7, 13.8] | 3596 [2065, 5845] | 0.356 | 31.3 |
| full | 20.0 | 0.731 | -172.5 [-178.6, -166.3] | 0.851 [0.811, 0.892] | 8.0 [3.4, 16.5] | - | - | - |
| full_sp | 15.5 | 0.837 | -179.7 [-190.2, -169.9] | 0.528 [0.408, 0.644] | 6.6 [2.7, 13.8] | 3885 [2391, 5926] | 0.326 | 40.2 |
| full_interact | 19.4 | 0.747 | -166.0 [-173.7, -158.3] | 0.715 [0.604, 0.823] | 10.0 [4.2, 21.7] | - | - | - |
| full_interact_sp | 15.5 | 0.839 | -178.4 [-188.9, -168.2] | 0.590 [0.441, 0.737] | 6.7 [2.8, 14.4] | 3615 [2102, 5918] | 0.341 | 33.7 |
| elevation_only_sp | 15.7 | 0.834 | -186.3 [-194.3, -178.5] | 0.585 [0.464, 0.698] | 6.4 [2.7, 13.3] | 3820 [2296, 5931] | 0.387 | 38.8 |
| elevation_c4_sp | 15.7 | 0.834 | -186.1 [-194.2, -178.1] | 0.584 [0.464, 0.699] | 6.4 [2.7, 13.3] | 3818 [2289, 5936] | 0.384 | 38.7 |
| c4_only_sp | 16.0 | 0.829 | -184.0 [-191.7, -176.5] | 0.573 [0.469, 0.669] | 5.7 [2.4, 11.6] | 3869 [2321, 5928] | 0.368 | 37.7 |
| elevation_c4_interact_sp | 15.7 | 0.835 | -184.3 [-193.0, -176.1] | 0.562 [0.440, 0.679] | 6.5 [2.7, 13.5] | 3819 [2304, 5908] | 0.380 | 39.3 |

*Note:* "Knot Slope SD" and "Knot Int. SD" are the Gaussian-process amplitude hyperparameters ($\sigma_{\text{slope}}$ and $\sigma_{\text{intercept}}$), not the standard deviation of the posterior-mean spatial field across sites. The latter are smaller (~0.12–0.15 and 14.2–17.2‰, Section 3.2) because the predictive-process projection and density-adaptive shrinkage reduce the realized variance of the fitted field.

Table 3: Variance decomposition for spatial models

| Model | Spatial (%) | Residual (%) | Intercept (%) | Slope (%) |
|---|---|---|---|---|
| baseline_sp | 51.4 | 48.6 | 96.6 | 3.4 |
| baseline_env_sp | 56.9 | 43.1 | 97.6 | 2.4 |
| baseline_veg_sp | 47.8 | 52.2 | 96.6 | 3.4 |
| full_sp | 56.5 | 43.5 | 97.7 | 2.3 |
| full_interact_sp | 52.2 | 47.8 | 97.1 | 2.9 |
| elevation_only_sp | 53.5 | 46.5 | 96.5 | 3.5 |
| elevation_c4_sp | 53.4 | 46.6 | 96.5 | 3.5 |
| c4_only_sp | 51.0 | 49.0 | 96.6 | 3.4 |
| elevation_c4_interact_sp | 54.2 | 45.8 | 96.7 | 3.3 |

*Note:* Variance components shown as percentage of total variance. Spatial = variance explained by spatial Gaussian process; Residual = unexplained variance; Intercept/Slope = proportion of spatial variance attributed to intercept vs. slope components.

Table 4: Environmental covariate coefficients

| Model | $\beta_{C4}$ | $\beta_{tree}$ | $\beta_{shrub}$ | $\beta_{grass}$ | $\beta_{precip}$ |
|---|---|---|---|---|---|
| baseline | - | - | - | - | - |
| baseline_sp | - | - | - | - | - |
| baseline_env | - | - | - | - | -0.052 [-0.081, -0.022] |
| baseline_env_sp | - | - | - | - | 0.065 [0.017, 0.113] |
| baseline_veg | -0.059 [-0.175, 0.061] | -0.177 [-0.440, 0.088] | 0.805 [0.557, 1.050] | -0.236 [-0.424, -0.051] | - |
| baseline_veg_sp | 0.101 [-0.032, 0.236] | -0.442 [-0.715, -0.173] | 0.569 [0.287, 0.859] | -0.233 [-0.439, -0.028] | - |
| full | -0.070 [-0.151, 0.009] | -0.252 [-0.456, -0.052] | 0.160 [-0.053, 0.371] | -0.197 [-0.357, -0.038] | -0.016 [-0.054, 0.021] |
| full_sp | 0.054 [-0.032, 0.141] | -0.207 [-0.410, -0.005] | 0.067 [-0.166, 0.305] | -0.243 [-0.404, -0.078] | 0.078 [0.028, 0.130] |
| full_interact | -0.067 [-0.191, 0.055] | 0.006 [-0.278, 0.296] | 0.787 [0.513, 1.061] | -0.281 [-0.485, -0.082] | 0.000 [-0.036, 0.036] |
| full_interact_sp | 0.081 [-0.062, 0.221] | -0.522 [-0.799, -0.241] | 0.523 [0.211, 0.835] | -0.249 [-0.467, -0.029] | 0.062 [0.013, 0.112] |
| elevation_only_sp | - | - | - | - | - |
| elevation_c4_sp | 0.011 [-0.068, 0.089] | - | - | - | - |
| c4_only_sp | 0.061 [-0.013, 0.135] | - | - | - | - |
| elevation_c4_interact_sp | 0.087 [-0.054, 0.232] | - | - | - | - |

*Note:* Coefficient estimates shown as posterior mean [95% credible interval]. $\beta_{C4}$ = C4 grass fraction effect; $\beta_{tree}, \beta_{shrub}, \beta_{grass}$ = plant functional type effects; $\beta_{precip}$ = precipitation effect. Dashes indicate parameters not included in the model. All coefficients on the Stan model's standardized $\delta^2$H scale.

Table 5: $\delta^2H_{precip}$×vegetation interaction coefficients

| Model | $\beta_{\delta^2H_p \times C4}$ | $\beta_{\delta^2H_p \times tree}$ | $\beta_{\delta^2H_p \times shrub}$ | $\beta_{\delta^2H_p \times grass}$ |
|---|---|---|---|---|
| full_interact | -0.003 [-0.084, 0.075] | 0.268 [0.105, 0.429] | 0.480 [0.342, 0.620] | 0.049 [-0.064, 0.161] |
| full_interact_sp | 0.021 [-0.077, 0.120] | -0.240 [-0.416, -0.063] | 0.267 [0.105, 0.429] | -0.028 [-0.142, 0.088] |

*Note:* Each coefficient is the change in the $\delta^2H_{wax}$–$\delta^2H_{precip}$ slope per unit increase in that vegetation fraction; a positive value indicates a steeper slope in that vegetation type. Estimates shown as posterior mean [95% credible interval]. Dashes indicate interaction terms not included in the model. All coefficients on the Stan model's standardized $\delta^2H$ scale.

# Supplementary Material for "Spatial autocorrelation inflates the global leaf-wax $\delta^2$H–precipitation slope"

Alexander S. Bradley[a]

[a]*Department of Earth, Environmental, and Planetary Sciences, Washington University in St. Louis, 1 Brookings Drive, Saint Louis, Missouri 63130, USA*

### *S1.1 Ordinary Least Squares Regression*

The relationship between $\delta^2\mathrm{H}_{\mathrm{wax}}$ and $\delta^2\mathrm{H}_{\mathrm{precip}}$ can be described by an ordinary least squares (OLS) regression (Sachse et al., 2012). We use $\delta^2\mathrm{H}_{\mathrm{precip}}$ for the latent precipitation hydrogen-isotope value at a site and $\delta^2 H^{\mathrm{OIPC}}_{\mathrm{precip}}$ for the observed OIPC raster value (the same convention as in the main text Methods, Section 2.3). The OLS approach treats the observed OIPC value as if it were the latent predictor, modeling $\delta^2\mathrm{H}_{\mathrm{wax}}$ as a linear function of $\delta^2 H^{\mathrm{OIPC}}_{\mathrm{precip}}$ with Gaussian noise accounting for unexplained variation around the regression line. It can be written as:

$$\delta^2 H_{wax,i} = \beta_0 + \beta_{\delta^2\mathrm{H}_p}\, \delta^2 H^{\mathrm{OIPC}}_{precip,i} + \epsilon_i \tag{S1}$$

where $\delta^2 H^{\mathrm{OIPC}}_{\mathrm{precip},i}$ is the observed OIPC raster value at site $i$ (treated by OLS as if it were the latent $\delta^2 H_{\mathrm{precip},i}$, with no errors-in-variables correction; see Section S2.3 for the Bayesian EIV treatment), $\delta^2 H_{\mathrm{wax},i}$ is the measured wax value, $\beta_0$ is the intercept, $\beta_{\delta^2\mathrm{H}_p}$ is the slope, and $\epsilon_i$ is an error term, typically assumed to follow a normal distribution:

$$\epsilon_i \sim \mathcal{N}\left(0, \sigma^2\right) \tag{S2}$$

Equation 1 is a full generative model for $\delta^2\mathrm{H}_{\mathrm{wax}}$ that assumes all residual variation is unstructured. $\epsilon_i$ therefore implicitly absorbs both measurement error and any spatial or ecological effects not included in the linear predictor. If fractionation followed simple two-pool mixing (which is unlikely), $\beta_{\delta^2\mathrm{H}_p}$ would represent the fractionation factor $\alpha$ and $\beta_0$ would represent the same fractionation $\varepsilon$ expressed in permil (Sessions and Hayes, 2005).

OLS has several advantages for proxy-based reconstructions (McClelland et al., 2021): it is simple to implement, provides an intuitive way to relate proxy measurements to environmental variables, and supports straightforward estimation of prediction uncertainty. It also helps expose common challenges in proxy calibration, such as the dominance of unexplained variance. OLS regression relies on strict assumptions about error structure (e.g., homoscedasticity, uncorrelated residuals) and assumes predictors are measured without error; when this last assumption is violated, slope estimates are biased toward zero (regression dilution). Analyses that involve nonlinear responses, interacting covariates, or uncertainty in the predictors require more flexible tools than ordinary least squares.

OLS still provides a useful baseline for the $\delta^2 H^{\mathrm{OIPC}}_{\mathrm{precip}}$–$\delta^2\mathrm{H}_{\mathrm{wax}}$ relationship. Figure 1 in the main text shows the OLS regression of the $\delta^2\mathrm{H}_{\mathrm{wax}}$ of 1,129 sedimentary *n*-$\mathrm{C}_{29}$ alkanes against point values from the OIPC $\delta^2\mathrm{H}_{\mathrm{precip}}$ field (i.e. $\delta^2 H^{\mathrm{OIPC}}_{\mathrm{precip}}$). The relationship is linear ($p < 2.2 \times 10^{-16}$) with $\beta_0 = -121.9 \pm 1.4$ and $\beta_{\delta^2\mathrm{H}_p} = 0.832 \pm 0.018$, and $R^2 = 0.643$ (RMSE = 23.0‰); $\delta^2 H^{\mathrm{OIPC}}_{\mathrm{precip}}$ strongly predicts $\delta^2\mathrm{H}_{\mathrm{wax}}$. The non-spatial model baseline used in the main text instead uses the fitted spatial-integration predictor, giving a slope of 0.778 (Figure S4; Table 2).

Any calibration also requires uncertainty on the predicted relationship. The prediction interval is the appropriate measure because it incorporates both parameter uncertainty and the residual variance (National Research Council, 2006). In an OLS regression the prediction interval absorbs all unmodeled influences on the calibration. Bayesian approaches yield posterior predictive intervals that serve the same purpose, combining model and residual uncertainty. Whether the framework is frequentist or Bayesian, the prediction interval is the most informative expression of uncertainty for paleoclimate reconstructions. National Research Council (2006) note that the bounds of the prediction interval only capture statistical uncertainty in the calibration dataset, and do not account for additional sources of uncertainty such as non-stationarity. For the regression of $\delta^2\mathrm{H}_{\mathrm{wax}}$ on $\delta^2 H^{\mathrm{OIPC}}_{\mathrm{precip}}$, the 95% prediction interval for $\delta^2\mathrm{H}_{\mathrm{wax}}$

carries substantial unexplained variability, even near the center of the calibration range. At the mean value of $\delta^2 H^{\text{OIPC}}_{\text{precip}}$, the half-width of the prediction interval is 45.3‰ (i.e., $\delta^2 H^{\text{OIPC}}_{precip,i}$ predicts a value of $\delta^2 H_{wax,i} \pm 45.3‰$), and the full width is 90.5‰.

For applications to paleohydrology, this noisy relationship must be inverted. That is, we measure $\delta^2\text{H}_{\text{wax,0}}$ to make an estimate $\widehat{\delta^2\text{H}_{\text{precip}}}$. Formally, this is done via the inverted equation:

$$\widehat{\delta^2\text{H}_{\text{precip,0}}} = \frac{\delta^2\text{H}_{\text{wax,0}} - \widehat{\beta_0}}{\widehat{\beta_{\delta^2\text{H}_p}}} \tag{S3}$$

This estimate of $\delta^2\text{H}_{\text{precip}}$ from $\delta^2\text{H}_{\text{wax}}$ carries an even larger uncertainty than the forward calibration. With frequentist methods, an exact solution for the range of the inverse prediction interval (IPI) requires solving a quadratic inequality derived from Fieller's theorem (Fieller, 1954), which fully accounts for uncertainty in the regression slope $\beta_{\delta^2\text{H}_p}$. Although the full Fieller calculation is seldom carried out, an approximation to the IPI can be obtained by assuming no uncertainty in $\beta$ (McClelland et al., 2021):

$$\delta^2\text{H}_{\text{precip,0}} = \widehat{\delta^2\text{H}_{\text{precip,0}}} \pm \frac{\widehat{\sigma}\, t_{\alpha,n-2}}{\left|\widehat{\beta_{\delta^2\text{H}_p}}\right|} \tag{S4}$$

where $t_{\alpha,n-2}$ is the dimensionless critical value of the Student's $t$-distribution, which depends on $n$, the number of observations in the calibration, and $\alpha$ which determines the confidence level. This equation shows that the uncertainty rises dramatically as the slope $\left|\widehat{\beta_{\delta^2\text{H}_p}}\right|$ approaches zero.

For the global regression shown in Figure 1 of the main text, a $\delta^2\text{H}_{\text{wax}}$ value of -180‰ vs. VSMOW would predict a reconstructed $\delta^2\text{H}_{\text{precip}}$ of -69.7‰. The 95% uncertainty range calculated by the Fieller exact solution would be [-124.3, -15.4]‰, and the McClelland approximation gives essentially the same bounds at [-124.1, -15.4]‰. Both methods yield an uncertainty with a full width of approximately 109‰ at $\delta^2\text{H}_{\text{wax}}$ = -180‰, and the IPI widens toward the edges of the calibration. This uncertainty range exceeds the variation in $\delta^2\text{H}_{\text{wax}}$ signals in many records used for paleohydrological reconstructions (Tierney et al., 2008; Konecky et al., 2016; Daniels et al., 2021; Martins et al., 2022; Zhao et al., 2024).

Global OLS regressions are therefore unsuitable for reconstructing $\delta^2\text{H}_{\text{precip}}$. Smaller variations in $\delta^2\text{H}_{\text{wax}}$ can be taken to reflect real ecological or climatic changes, but cannot be assumed to reflect changes in $\delta^2\text{H}_{\text{precip}}$ (McFarlin et al., 2019). In most records, the inference that $\delta^2\text{H}_{\text{wax}}$ directly tracks $\delta^2\text{H}_{\text{precip}}$ is not warranted given the magnitude of uncertainty in $\delta^2\text{H}_{\text{precip}}$ reconstructions from global OLS calibrations. By extension, inferring wetter or drier conditions from changes in $\delta^2\text{H}_{\text{wax}}$ is also problematic: detecting a discernible change in $\delta^2\text{H}_{\text{precip}}$ requires understanding both the prediction uncertainty and the temporal autocorrelation in the $\delta^2\text{H}_{\text{wax}}$ signal, since autocorrelation affects the statistical significance of differences between time points. Confidently inferring $\delta^2\text{H}_{\text{precip}}$ or wet/dry cycles requires additional constraints or alternative approaches, unless changes are large in magnitude (McFarlin et al., 2019). Additional constraints could include estimates of the fraction of $C_4$ vegetation (Collins et al., 2013; Wang et al., 2013; Utida et al., 2019) or of plant functional type (Feakins, 2013; Chang et al., 2021; Daniels et al., 2021; Konecky et al., 2019).

### *S1.2 Constant Fractionation Approaches*

Some studies (Corcoran et al., 2022; Eensalu et al., 2023; Feakins et al., 2016; Konecky et al., 2019; Tipple et al., 2013) avoid global OLS regressions and instead assume a constant or plant-dependent apparent fractionation factor ($^2\varepsilon_{\text{app}}$). This approach treats the relationship between $\delta^2\text{H}_{\text{precip}}$ and $\delta^2\text{H}_{\text{wax}}$ as a simple offset, imposing a 1:1 transfer (slope = 1) and applying a global mean intercept without accounting for residual uncertainty. These assumptions simplify paleoclimate reconstruction but bypass the statistical machinery needed to quantify prediction uncertainty and assess the significance of observed changes.

In its simplest form, this relationship is modeled as:

$$\delta^2 H_{wax,0} = \beta_0 + \delta^2 H_{precip,0} \tag{S5}$$

Which assumes

$$\beta_0 = {}^2\varepsilon_{\text{app}} \tag{S6}$$

$$\beta_{\delta^2\text{H}_p} = 1 \tag{S7}$$

$$\epsilon_i = 0 \tag{S8}$$

In other words, the model assumes the relationship between $\delta^2\text{H}_{\text{wax}}$ and $\delta^2\text{H}_{\text{precip}}$ has a slope of 1 and no uncertainty. Neither assumption is valid. If the relationship were two-component mixing, the slope should reflect the fractionation factor: for an offset of ${}^2\varepsilon_{\text{app}} \approx$ -120‰, the expected slope is approximately 0.88, not 1 (Sessions and Hayes, 2005). The actual relationship is not this simple, and if the process is complex enough to deviate from simple fractionation theory, the slope should be estimated from data rather than assumed. An assumption of zero uncertainty is untenable for any fractionation estimated from data with measurement error and natural variability.

For approaches that account for vegetation composition, ${}^2\varepsilon_{\text{app}}$ is sometimes varied by plant functional type (PFT), yielding

$$\delta^2\text{H}_{\text{wax},0} = \delta^2\text{H}_{\text{precip},0} + \sum_j {}^2\varepsilon_{\text{app},j} \cdot \text{PFT}_j \tag{S9}$$

where $\text{PFT}_j$ is the fractional abundance of plant type $j$, and each ${}^2\varepsilon_{\text{app},j}$ is a fixed fractionation factor for that plant type. The fractionation values are usually taken from prior vegetation studies (e.g. $C_3$ vs $C_4$, or tree/shrub/grass) rather than being estimated alongside the calibration data, and the associated uncertainties are seldom carried forward in the analysis.

Although this approach allows ${}^2\varepsilon_{\text{app}}$ to vary by plant type and its variance can be described empirically (e.g., via boxplots), it does not provide a statistical model for predicting $\delta^2\text{H}_{\text{precip}}$ or propagating uncertainty from observed $\delta^2\text{H}_{\text{wax}}$. Regression-based methods, by contrast, explicitly model the relationship, quantify both within- and across-group variance, and support hypothesis testing and predictive inference.

Forward simulations such as WaxPSM (Konecky et al., 2019) are similar in approach. WaxPSM varies the inputs (e.g., $\delta^2\text{H}_{\text{precip}}$, vegetation fractions) by Monte Carlo sampling but treats the leaf wax fractionation factors as fixed numbers taken from the literature. Each draw passes through a deterministic transfer function with no residual-error term, so the spread in the model's output reflects only input uncertainty, without the scatter seen in calibration data. Models of this kind explore how environmental variability propagates through biological and geochemical processes to influence isotopic signals in sedimentary leaf waxes. They are useful complements to statistical calibration but are not generally inverted to predict $\delta^2\text{H}_{\text{precip}}$.

### *S2.1 Data Compilation and Processing*

#### *S2.1.1 Data Preparation*

A global database of 1,129 published surface sediment and soil measurements of the *n*-$C_{29}$ alkane $\delta^2\text{H}_{\text{wax}}$ was constructed by aggregating compilation databases (Liu and An, 2019; McFarlin et al., 2019; Ladd et al., 2021), a large open-access deposit (ETH Zurich Research Collection, Ladd et al., 2021), the recent process-based modeling and compilation work of Hren and Brandon (2026), and individual dataset releases via Wyoming Data Repository, NOAA WDS Paleoclimatology, PANGAEA, and primary publications (Struck et al., 2020; Corcoran et al., 2022; Roy and Sanyal, 2022; Gaviria-Lugo et al., 2023; Wang et al., 2023; Repasch et al., 2021; Gensel et al., 2022; Nieto-Moreno et al., 2016). Thirteen compilation-style source entries plus five direct ingests from individual primary publications make up the 18 source rows in Table S1; collectively these index 49 unique primary-publication DOIs. We restricted our analysis to the *n*-$C_{29}$ alkane because this is a widely applied proxy and allows comparability with prior calibrations. The method described here could be applied to other compounds.

Environmental predictor variables were extracted from global gridded datasets as described in the main text (Section 2.1.2). All raster processing was performed using R (terra package version 1.7) and Python (earthaccess for data downloads). The preprocessing workflow consisted of the following steps:

$C_4$ vegetation: $C_4$ fractional cover data were extracted from the NUS $C_4$ distribution dataset NetCDF (Luo et al., 2024). The 19 annual layers (2001–2019) were temporally averaged to create a mean $C_4$ fraction raster. The NetCDF file was transposed and georeferenced to WGS84 to ensure correct spatial orientation.

MODIS land cover: MODIS MCD12Q1 Collection 6.1 land cover data were downloaded for 2001-2019 using the NASA earthaccess API. Annual global mosaics were created from HDF tiles by extracting the LC_Type1 band and mosaicking using GDAL. The sinusoidal projection mosaics were reprojected to WGS84 using nearest-neighbor resampling to preserve categorical class values. A modal land cover classification was computed across the 19-year period, then aggregated to match OIPC resolution (~9 km) while calculating fractional cover percentages for each IGBP class. Finally, IGBP classes were grouped into three plant functional types: trees (classes 1-5: all forest types), shrubs (classes 6-7: shrublands), and grasses (classes 8-10: woody savannas, savannas, and grasslands).

TerraClimate variables: Monthly TerraClimate NetCDF files (Abatzoglou et al., 2018) for precipitation, soil moisture, maximum temperature, and vapor pressure deficit were downloaded for 2001-2019. For each variable and year, monthly values were aggregated to annual values (summed for precipitation; averaged for other variables), then the 19 annual values were averaged to create 2001-2019 long-term means.

All raster datasets were processed in WGS84 (EPSG:4326) coordinate reference system. OIPC $\delta^2H_{precip}$ and elevation from GMTED2010 (via EarthEnv-DEM90) were used directly as provided by the data sources. For each sediment sample location, environmental predictors were extracted using a multi-scale spatial averaging approach (Section S2.1.5) rather than point extraction. Two distance parameters appear in this workflow and have distinct roles: the per-site raster extraction radius (up to 5°, ~555 km at the equator) determines which raster grid cells are pulled into the per-site extraction record, and the exponential-decay kernel support used during weighting (described in Section S2.1.5 as "cells within 1000 km") determines how those extracted values are weighted into the predictor value used by the calibration. This integration accounts for the spatial footprint of sediment archives and reduces sensitivity to minor geolocation errors. For $C_4$ vegetation, pixels with missing data were filled using ecological rules: locations with |latitude| $\geq 50°$ or elevation $\geq 1500$ m were assigned $C_4$ fraction = 0, consistent with known $C_4$ plant biogeography (Still et al., 2003; Luo et al., 2024).

### *S2.1.2 Measurement Uncertainty Assignment*

Our compilation included the $\delta^2H_{wax}$ value and, where available, the reported uncertainty on this measurement. Where uncertainties were not reported, we assigned 3‰; where they were reported as 0‰, we assigned 1‰. These low values are likely optimistically precise (Polissar and D'Andrea, 2014), but have little effect on the model: measurement uncertainty on $\delta^2H_{wax}$ contributes only minimally to the uncertainty in predicting $\delta^2H_{precip}$.

### *S2.1.3 Coordinate Reference System*

Latitude and longitude data were taken directly from the compilations when reported. Where unstated they were assumed to be reported in a WGS84 (EPSG:4326) coordinate reference system (CRS). Any residual positional uncertainties from undocumented CRS differences are negligible relative to the spatial resolutions used for our calibration. To handle duplicate coordinates that can cause numerical issues in spatial models, we added Gaussian noise with standard deviation 0.0001° (up to 11 meters) to each site's location.

### *S2.1.4 Environmental Covariate Extraction*

We compiled eight global raster datasets as environmental covariates contributing to variations in $\delta^2H_{wax}$:

1. $\delta^2H_{precip}$: Online Isotopes in Precipitation Calculator v3.2 (Bowen and Revenaugh, 2003; IAEA/WMO, 2015; Bowen, 2018) ~9 km resolution (5 arc-minutes)

2. Elevation: EarthEnv-DEM90 aggregated from CGIAR-CSI SRTM 90m v4.1 (Amatulli et al., 2018)

3. Plant Functional Type (PFT): MODIS MCD12Q1 Land Cover Type 1 product (Friedl and Sulla-Menashe, 2019) averaged 2001-2019, ~9 km resolution

4. $C_4$ vegetation fraction: Luo et al. (2024), global dataset, 0.5° resolution (~56 km at the equator). For pixels missing from the $C_4$ contribution raster, we assigned a $C_4$ fraction of zero to pixels that had |latitudes| $\geq 50°$ or elevations $\geq 1500$, consistent with known biogeography of $C_4$ plants (Still et al., 2003; Luo et al., 2024).

5. Climate variables: TerraClimate (Abatzoglou et al., 2018), ~4 km resolution, 2001-2019 means for:

- Annual precipitation (sum of monthly values)

- Soil moisture
- Maximum temperature
- Vapor pressure deficit (VPD)

*S2.1.5 Multi-scale spatial integration*

To account for the spatial integration of leaf waxes in sediment samples, we implemented distance-weighted averaging for environmental predictors (Figure S1). At each sample site $i$, for each spatial buffer scale $r$, we computed an exponentially decaying kernel weight for all grid cells $j$ within 1000 km:

$$w_{i,j}^{(r)} = \exp\left(-\frac{d_{i,j}}{r}\right) \tag{S10}$$

where $d_{i,j}$is the great-circle distance between site $i$ and grid cell $j$.

These weights were used to calculate spatially weighted covariate averages:

$$\bar{X}_{i,r} = \frac{\sum_{j\in J_i} \exp\left(-\frac{d_{i,j}}{r}\right) \cdot X_j}{\sum_{j\in J_i} \exp\left(-\frac{d_{i,j}}{r}\right)} \tag{S11}$$

where $X_j$is the covariate value at grid cell $j$ and $J_i$is the set of all grid cells within 1000 km of site $i$. During model fitting, a single parameter $\lambda$ controls the effective integration scale by weighting the pre-computed scales:

$$w_r = \frac{\exp\left(-r/\lambda\right)}{\sum_{r'} \exp(-r'/\lambda)} \tag{S12}$$

$$\bar{X}_i = \sum_r w_r \cdot \bar{X}_{i,r} \tag{S13}$$

where the sum is over all nine pre-computed scales r' ∈ 1, 3, 5, 10, 20, 40, 70, 100, 150. This approach interpolates between the pre-computed scales, allowing $\lambda$ to take any value while keeping computation tractable. The $\lambda$ parameter controls the weighting among the pre-computed spatial integration scales (1, 3, 5, ..., 150 km); it parameterizes the effective spatial integration window of the predictor in the calibration rather than a directly identified physical integration radius for sedimentary leaf waxes.

*S2.1.6 Uncertainty in Environmental Predictors*

OIPC provides standard error estimates for $\delta^2 H_{\text{precip}}^{\text{OIPC}}$, which were incorporated into our model. The OIPC standard errors are treated as pointwise independent errors-in-variables linking the observed $\delta^2 H_{\text{precip}}^{\text{OIPC}}$ to the latent $\delta^2\text{H}_{\text{precip}}$; in reality, interpolation residuals from a smoothly-fit precipitation-isotope surface are likely spatially structured across nearby sites, so the predictor-uncertainty term in the model probably understates uncertainty in regional gradients of the latent field. Uncertainties in other environmental covariates were not explicitly propagated. MODIS land cover classification has an overall accuracy of approximately 73–75% from independent validation (Friedl and Sulla-Menashe, 2019). Elevation accuracy in the GMTED2010 dataset is reported as 26–30 m RMSE for the 7.5 arc-second mean elevation product (Danielson and Gesch, 2011). The $C_4$ vegetation fraction model reports typical uncertainties of 1–3% of land surface area, rising to 6–7% in certain regions (Luo et al., 2024). TerraClimate has a median absolute error of ~9% against station observations for precipitation (Abatzoglou et al., 2018). No spatially explicit error models exist for most of these covariates. Their effects on $\delta^2\text{H}_{\text{wax}}$ are small relative to the dominant spatial patterns, and quantitative uncertainty models are unavailable for most predictors, so these uncertainties were not propagated through the analysis. The reported reconstruction uncertainty is therefore conditional on the environmental products used; propagating predictor uncertainties in MODIS, GMTED2010, the $C_4$ surface, and TerraClimate (and any spatial covariance in the OIPC errors) would widen the intervals, so the reconstruction uncertainty and detection thresholds reported here should be treated as lower bounds.

## S2.2 Exploratory Data Analysis

### S2.2.1 Spatial Structure Analysis

We examined the spatial distribution and clustering of samples to identify potential geographic biases in the calibration dataset. The 1,129 samples showed strong geographic clustering, with high densities in Europe, eastern North America, and East Asia, and sparse coverage in the tropics, central Asia, and oceanic regions (main-text Figure 2).

Nearest-neighbor analysis revealed:

- Mean nearest-neighbor distance: 34 km (median: 4 km)
- 62.5% of samples within 10 km of another sample
- 92.3% of observations within 100 km of nearest neighbor

The OLS residuals were spatially structured (Figure S3; Moran's I = 0.584, $p < 0.001$ at $k = 8$ nearest neighbors). Banded by distance, the autocorrelation stayed positive out to continental scales (I = 0.57 within 100 km; 0.43 within 500 km; 0.36 within 1,000 km; 0.23 within 2,000 km; 0.15 within 3,000 km; 0.06 within 5,000 km), all significant at $p < 10^{-87}$. The spatial models give a second estimate of the same quantity. Their Gaussian-process length scale, 3,600–3,950 km (main text Table 2), is the characteristic correlation length, and it tracks the Moran's I decay.

### S2.2.2 Multicollinearity Assessment

We computed pairwise Pearson correlations among all candidate predictors (Figure S2). Strong correlations ($|r| > 0.7$) were observed between:

- $\delta^2 H^{\mathrm{OIPC}}_{\mathrm{precip}}$ and maximum temperature (r = +0.85)
- $\delta^2 H^{\mathrm{OIPC}}_{\mathrm{precip}}$ and VPD (r = +0.77)
- Maximum temperature and VPD (r = +0.80)
- Annual precipitation and soil moisture (r = +0.85)

Variance inflation factor (VIF) analysis identified several problematic variables:

- Maximum temperature: VIF = 19.8
- VPD: VIF = 10.4
- Annual precipitation: VIF = 6.6
- $\delta^2 H^{\mathrm{OIPC}}_{\mathrm{precip}}$: VIF = 6.0 (when all climate variables included)
- Soil moisture: VIF = 5.6

To address collinearity while retaining mechanistic interpretability, we:

1. Removed VPD and maximum temperature (redundant with $\delta^2 H^{\mathrm{OIPC}}_{\mathrm{precip}}$ signal)
2. Removed soil moisture (highly correlated with annual precipitation)
3. Retained annual precipitation for use in some models
4. Confirmed VIF < 5 for all retained predictors in final model configurations

As a check on variable importance under penalization, we also fit an elastic net ($\alpha = 0.5$). $\delta^2 H^{\mathrm{OIPC}}_{\mathrm{precip}}$ dominated at every penalty level; its coefficient (0.66) was several times larger than any other. After $\delta^2\mathrm{H}^{\mathrm{OIPC}}_{\mathrm{precip}}$, the largest coefficients were associated with plant functional type fractions (grass and tree), annual precipitation, elevation, $C_4$ fraction, and the remaining climate variables entered with smaller ones. This ordering matches the regression results (Section 3.4 of the main text), where grass and tree cover retain measurable effects in the spatial models and the $C_4$ and elevation effects are weaker.

## S2.3 Statistical Modeling Framework

### S2.3.1 Complete Model Specification

The full hierarchical Bayesian model for sedimentary $\delta^2\mathrm{H}_{\mathrm{wax}}$ is specified as:

$$\delta^2 H_{wax,i} \sim \mathcal{N}\left(\mu_i, \sigma^2_{total}\right) \tag{S14}$$

where the mean function $\mu_i$ includes all fixed and spatially-varying components:

$$\mu_i = \beta_0(s_i) + \beta_{\delta^2\mathrm{H}_p}(s_i) \times \delta^2 H_{precip,i} + f_{elev}(elevation_i) + \beta_{C4} \times C4_i + \beta_{precip} \times precip_i + \beta_{tree} \times tree_i + \beta_{shrub} \times shrub_i + \beta_{grass} \times grass_i + \beta_{\delta^2\mathrm{H}_p \times C4}\left(\delta^2 H_{precip,i} \times C4_i\right) + \beta_{\delta^2\mathrm{H}_p \times tree}\left(\delta^2 H_{precip,i} \times tree_i\right) + \beta_{\delta^2\mathrm{H}_p \times shrub}\left(\delta^2 H_{precip,i} \times shrub_i\right) + \beta_{\delta^2\mathrm{H}_p \times grass}\left(\delta^2 H_{precip,i} \times grass_i\right) \quad \text{(S15)}$$

### *S2.3.2 B-spline Specification for Elevation*

The elevation effect $f_{\mathrm{elev}}$(elevation) was modeled using cubic B-splines (Wood, 2017):

$$f_{elev}(elevation) = \sum_{j=1}^{K} \beta_{elev,j} \times B_j(elevation) \quad \text{(S16)}$$

where:

- K = 13 basis functions (9 interior knots + 4 boundary knots)
- Interior knots placed at quantiles of the elevation distribution
- $\mathrm{B_j}$(elevation) are the B-spline basis functions
- $\beta_{\mathrm{elev},j}$ are the spline coefficients

The B-spline basis matrix is collinear, so we centered each basis function by subtracting its column mean. Centered bases kept the fit numerically stable.

### *S2.3.3 Vegetation-Climate Interaction Terms*

Vegetation may modulate the relationship between $\delta^2\mathrm{H}_{\mathrm{precip}}$ and $\delta^2\mathrm{H}_{\mathrm{wax}}$, and we tested this with interaction terms (Bolker, 2008) between $\delta^2\mathrm{H}_{\mathrm{precip}}$ and the vegetation variables. Each $\beta_{\delta^2\mathrm{H}_p}\times$ veg coefficient gives the change in the $\delta^2\mathrm{H}_{\mathrm{precip}}$ slope per unit increase in that vegetation type (Jaccard et al., 2003). For example:

- $\beta_{\delta^2\mathrm{H}_p}\times\mathrm{C_4}$ quantifies how the isotopic relationship differs in $\mathrm{C_4}$-dominated ecosystems
- A positive $\beta_{\delta^2\mathrm{H}_p}\times\mathrm{C_4}$ indicates steeper slopes (stronger $\delta^2\mathrm{H}_{\mathrm{wax}}$ response to $\delta^2\mathrm{H}_{\mathrm{precip}}$) in $\mathrm{C_4}$ vegetation
- A negative value indicates shallower slopes (weaker response) in $\mathrm{C_4}$ vegetation

We pre-computed the interaction terms at each spatial integration scale (1, 3, 5, 10, 20, 40, 70, 100, 150 km) as the spatially weighted products of the variables at that scale. The model then weighted these interaction matrices by the same exponential kernel (parameter $\lambda$) that it applied to the main effects.

- $\delta^2\mathrm{H}_{\mathrm{precip}}\times\mathrm{C_4}$: standardized as the product divided by $(\sigma_{\mathrm{OIPC}} \times \sigma_{\mathrm{C4}})$
- $\delta^2\mathrm{H}_{\mathrm{precip}}\times$PFT: standardized as the product divided by $\sigma_{\mathrm{OIPC}}$ (PFTs are proportions 0-1)

### *S2.3.4 Uncertainty Components*

Three sources of uncertainty propagate through the model. They are the analytical uncertainty in measured $\delta^2\mathrm{H}_{\mathrm{wax}}$, the uncertainty in the OIPC predictor $\delta^2 H^{\mathrm{OIPC}}_{\mathrm{precip}}$, and the residual calibration variance. The model does not pool them into one additive variance term; each is introduced at its own point. Analytical uncertainty is assigned per observation and enters the likelihood as a known component of response uncertainty. OIPC predictor uncertainty is an errors-in-variables term: the latent $\delta^2\mathrm{H}_{\mathrm{precip}}$ is sampled around the OIPC point estimate $\delta^2 H^{\mathrm{OIPC}}_{\mathrm{precip}}$ with location-specific variance, and that latent value then passes through the linear predictor. Residual variance is estimated from the data and absorbs whatever variation in $\delta^2\mathrm{H}_{\mathrm{wax}}$ is left over, including microscale spatial structure and unexplained proxy-system variability. Anyone reproducing the calibration should keep these components at their points of entry in the Stan model and should not collapse them into a single variance term in response space.

### *S2.3.5 Prior Specifications*

We used weakly informative priors to regularize the model while letting the data dominate posterior inference. Prior distributions for all model parameters are detailed in Table S2. The priors were selected on the following principles:

- Fixed effects: Centered at reasonable values with sufficient width to accommodate uncertainty
- Spatial components: Penalized complexity (PC) priors (Simpson et al., 2017) to control model complexity and prevent overfitting
- Variance components: Weakly informative normal priors to ensure reasonable scale while maintaining flexibility
- Integration scale: Lognormal distribution centered on physically plausible spatial scales for sediment integration

The spatial models used adaptive regularization. The prior variance for a knot effect grows with the local data density (Section S2.4.5), so knots in sparse regions receive stronger shrinkage, whereas knots in well-sampled regions are allowed greater flexibility. This density-dependent prior scaling makes the fitted spatial component a low-rank predictive-process spatial basis with density-adaptive shrinkage rather than a stationary Gaussian process.

### *S2.3.6 Model Variants*

We tested 14 model configurations to evaluate the importance of different components:

- baseline: $\delta^2\mathrm{H}_{\mathrm{precip}}$ only
- baseline_sp: $\delta^2\mathrm{H}_{\mathrm{precip}}$ with spatial effects
- baseline_env: $\delta^2\mathrm{H}_{\mathrm{precip}}$ + elevation + annual precipitation
- baseline_env_sp: $\delta^2\mathrm{H}_{\mathrm{precip}}$ + elevation + annual precipitation + spatial
- baseline_veg: $\delta^2\mathrm{H}_{\mathrm{precip}}$ + all vegetation + vegetation $\times$ $\delta^2\mathrm{H}_{\mathrm{precip}}$ interactions
- baseline_veg_sp: $\delta^2\mathrm{H}_{\mathrm{precip}}$ + all vegetation + vegetation $\times$ $\delta^2\mathrm{H}_{\mathrm{precip}}$ interactions + spatial
- full: All predictors
- full_sp: All predictors + spatial
- full_interact: All predictors + interactions
- full_interact_sp: All predictors + interactions + spatial
- elevation_only_sp: $\delta^2\mathrm{H}_{\mathrm{precip}}$ + elevation + spatial
- elevation_c4_sp: $\delta^2\mathrm{H}_{\mathrm{precip}}$ + elevation + C4 + spatial
- c4_only_sp: $\delta^2\mathrm{H}_{\mathrm{precip}}$ + C4 + spatial
- elevation_c4_interact_sp: $\delta^2\mathrm{H}_{\mathrm{precip}}$ + elevation + C4 + interaction + spatial

## *S2.4 Spatial Modeling Framework*

### *S2.4.1 Gaussian Process Specification*

The spatially varying intercept $\beta_0(s)$ and slope $\beta_{\delta^2 H_p}(s)$ are modeled using low-rank predictive-process spatial bases derived from independent Matérn covariance functions. Conceptually, these bases approximate Gaussian processes,

$$\beta_0(s) \sim \mathcal{GP}\left(\beta_0, k_{\beta_0}\left(s, s^{'}\right)\right) \tag{S17}$$

$$\beta_{\delta^2\mathrm{H}_p}(s) \sim \mathcal{GP}\left(\beta_{\delta^2\mathrm{H}_p,\mathrm{global}}, k_{\beta_{\delta^2\mathrm{H}_p}}\left(s, s^{'}\right)\right) \tag{S18}$$

where $\beta_0$ and $\beta_{\delta^2\mathrm{H}_p,\mathrm{global}}$ are global mean values, and $k_{\beta_0}$ and $k_{\beta_{\delta^2\mathrm{H}_p}}$ are independent spatial covariance functions. As fit, however, the GP is approximated by a finite-dimensional predictive-process basis at 125 knot locations (Section S2.4.2) and the basis coefficients are regularized by density-adaptive shrinkage (Section S2.4.5), so the fitted spatial component is a low-rank predictive-process spatial basis with adaptive shrinkage rather than a stationary GP. This formulation allows the intercept and $\delta^2\mathrm{H}_{\mathrm{precip}}$ slope to vary smoothly across space, capturing the environmental heterogeneity observed in our clustering analysis while maintaining the ability to make predictions at new locations.

*S2.4.2 Predictive Process Approximation*

For computational efficiency, we approximate each GP using the predictive process (Banerjee et al., 2008; Finley et al., 2009):

$$\beta_0(s_i) \approx \mathbf{c}_{\beta_0}(s_i)^T \mathbf{K}_{\beta_0}^{-1} \beta_0^* \tag{S19}$$

$$\beta_{\delta^2 \mathrm{H}_p}(s_i) \approx \mathbf{c}_{\beta_{\mathbf{OIPC}}}(s_i)^T \mathbf{K}_{\beta_{\mathbf{OIPC}}}^{-1} \beta_{\mathbf{OIPC}}^* \tag{S20}$$

Where $\beta_0^*$ and $\beta_{\mathbf{OIPC}}^*$ are the GP values at $m = 125$ knot locations, $\mathbf{K}_{\beta_0}$ and $\mathbf{K}_{\beta_{\mathbf{OIPC}}}$ are the $m \times m$ knot-to-knot covariance matrices, and $\mathbf{c}_{\beta_0}(s_i)$ and $\mathbf{c}_{\beta_{\mathbf{OIPC}}}(s_i)$ are $m \times 1$ covariance vectors between site $i$ and all knots.

*S2.4.3 Matérn Covariance Function*

We employed the Matérn 3/2 covariance kernel:

$$k(s_i, s_j) = \eta^2 \left(1 + \frac{\sqrt{3}\, d_{ij}}{\rho}\right) \exp\left(-\frac{\sqrt{3}\, d_{ij}}{\rho}\right) \tag{S21}$$

where:

- $\eta^2$ = marginal variance (process amplitude)
- $\rho$ = range parameter (correlation length scale in km)
- $d_{ij}$ = great-circle distance between sites $i$ and $j$

The kernel stays flexible and smooth without committing to strong differentiability assumptions (Stein, 1999). There is a subtlety on the sphere: the Matérn 3/2 covariance evaluated on great-circle distance need not be positive definite for arbitrary smoothness. We sidestep this by treating the spatial component as a finite-dimensional predictive-process spatial basis at the 125 knot locations (Section S2.4.4) rather than a continuous stationary Gaussian process on the sphere. We then verified positive definiteness directly. At every fitted posterior draw we examined, the 125×125 knot-to-knot covariance matrices $\mathbf{K}_{\beta_0}$ and $\mathbf{K}_{\beta_{\delta^2 \mathrm{H}_p}}$ were positive definite: across all nine spatial-model variants and 200 randomly subsampled posterior draws per model (1,800 draws total per matrix), Cholesky decomposition succeeded with no added jitter, and the minimum-of-minimum-eigenvalue across all models was $8.5 \times 10^{-5}$ (verification script: `scripts/verify_pd_knots.R`). The fitted field should be read as a regularized spatial surface defined through this basis rather than a draw from a strictly stationary GP on the globe. With the density-adaptive shrinkage on knot effects (Section S2.4.5), the spatial component becomes a low-rank GP basis with density-adaptive regularization.

*S2.4.4 Knot Placement and Coverage*

Two considerations set the number of knots. More knots give better spatial coverage, so that observations can inform the local field; but sparse data leaves many knots with no local observations regardless. We tried 75 to 150 knots. At 125 the results were stable and interpretable, and we used 125 for all reported models.

We placed knots using a spherical Fibonacci lattice (Swinbank and Purser, 2006) ensuring approximately uniform global distribution. With 125 knots:

- Mean inter-knot distance: ~1,910 km
- 71.7% of observations within 1,000 km of nearest knot
- 74.4% of knots had no observations within 1,000 km

This configuration resolved regional climate variation and stayed computationally tractable. Spatial models on highly irregular data coverage need to capture local variation where data are dense and keep predictions stable where data are sparse (Heaton et al., 2019). Our adaptive regularization (Section S2.4.5) constrains knots more tightly in data-sparse regions; this guards against overfitting yet still picks up genuine spatial patterns where data density permits.

### *S2.4.5 Spatially-Adaptive Regularization*

To prevent overfitting in data-sparse regions, we used spatially varying regularization in which the prior variance for each knot adapts to local data density. The regularization uses a piecewise function that applies stronger constraints where data are sparse:

For knots with no observations within 1,000 km:

$$\tau_{slope} = 0.40, \quad \tau_{intercept} = 0.50 \tag{S22}$$

For knots with 1-10 observations:

$$\tau_{slope} = 0.40 + 0.20 \times \frac{n}{10}, \quad \tau_{intercept} = 0.50 + 0.20 \times \frac{n}{10} \tag{S23}$$

For knots with >10 observations:

$$\tau_{slope} = 0.60 + 0.40 \times \left(1 - e^{-(n-10)/30}\right), \quad \tau_{intercept} = 0.70 + 0.30 \times \left(1 - e^{-(n-10)/30}\right) \tag{S24}$$

Estimates stay conservative where data are poor, and the model remains free to capture genuine spatial patterns where data density permits, so its flexibility tracks data availability (Simpson et al., 2017; Fuglstad et al., 2019).

### *S2.4.6 Computational Implementation*

Models were implemented in Stan using:

- Non-centered parameterization for hierarchical components
- Cholesky decomposition of covariance matrices
- PC priors on spatial standard deviations (Simpson et al., 2017):
- Intercept: $P(\sigma > 20‰) = 0.05$
- Slope: $P(\sigma > 0.3) = 0.05$

Convergence assessed via:

- $\hat{R} \leq 1.011$ for all parameters ($\hat{R} < 1.01$ for 13 of 14 models; *baseline_env* reached 1.011 on a B-spline elevation coefficient)
- Effective sample size (ESS bulk): minimum 857 (baseline_env, non-spatial); minimum 1,293 among spatial models (full_sp)
- Divergent transitions after warmup: zero in 12 of 14 models. *full_sp* produced 8 divergences out of 16,000 post-warmup samples (0.05%); *full_interact_sp* produced 1 of 16,000 (0.006%). We accept these residual divergences because the divergent-draw diagnostics argue for benign step-size adaptation lag rather than biased posterior coverage: (i) the 8 divergent iterations in *full_sp* cluster in consecutive pairs across multiple chains rather than scattering across the trace, the signature of transient step-size adaptation rather than persistent pathological geometry; (ii) z-scores of $\sigma_{\text{intercept,spatial}}$ at the divergent draws lie within $+1.7\sigma$ of the posterior median, so the divergences do not preferentially sample the upper-tail funnel geometry that would indicate biased exploration; and (iii) *full_sp* satisfies $\hat{R} < 1.01$ across chains despite the 8 divergences, so the between-chain consensus on the posterior is unaffected. Increasing `adapt_delta` or reparameterizing the spatial-amplitude block would likely eliminate the residual divergences but is not motivated by the diagnostic profile above.
- E-BFMI $\geq 0.76$ across all chains (minimum 0.759, *elevation_only_sp*)

## *S2.5 Extended Model Validation*

### *S2.5.1 Regional In-Sample Performance*

To see how model performance varies geographically, we split the residuals from each fitted model by region (Americas, Europe, Africa, Asia, Oceania) and computed regional RMSE, mean bias, and $R^2$ for each variant. These numbers measure how well each spatial model fits each region under the global parameter posterior. They are not a leave-one-region-out cross-validation in the sense of Roberts et al. (2017), which would refit the model with each region held out and is computationally prohibitive across all 14 variants. Table S3 reports regional in-sample performance for all variants.

### *S2.5.2 Data Density Categories*

To evaluate whether model performance degraded in data-sparse regions, we classified each observation by the number of other observations within 0.2 standardized coordinate units (approximately 500 km) of its nearest GP knot:

- Sparse: <10 observations (n=225)
- Medium: 10-50 observations (n=431)
- Dense: >50 observations (n=473)

We computed performance metrics for each category separately (illustrative values from *baseline_env_sp*): RMSE was 13.0‰ in sparse regions, 14.4‰ in medium-density regions, and 17.7‰ in dense regions. RMSE is highest in the dense regions. This most likely reflects greater environmental heterogeneity in well-sampled areas such as the Asian highlands, not a failure of the model.

### *S2.5.3 Overfitting Diagnostics*

We assessed three independent indicators of overfitting risk.

*Length scale vs. data spacing:* The observations were strongly clustered, with 92.3% of sites having a neighbor within 100 km. The estimated GP length scales (3,600–3,950 km) were about twice the mean inter-knot distance (1,910 km) and about 110 times the mean observation spacing (34 km). At that length scale the spatial field captures continental-scale trends; it does not interpolate between individual sites (Diggle and Ribeiro, 2007).

*Effective parameters:* The ratio $p_{eff}/n$ measures model complexity against sample size. Every spatial variant held $p_{eff}/n < 0.05$, and even the most complex model reached only 4.9% (55.0 effective parameters / 1,129 observations), far below the range where overfitting becomes a concern.

*Prediction uncertainty:* At each observation we took the width of the posterior predictive 95% interval. In *baseline_env_sp* the width grew from 63.8‰ in dense regions to 66.1‰ in sparse regions. Every spatial model kept this ordering. They were also tighter than the non-spatial models on average (~65‰ vs. ~80‰). The spatial field cut residual uncertainty overall, then let the intervals widen a little where the data thinned out.

## *S2.6 Simulation tests of model behavior*

Three sets of simulation tests probe the spatial model: (i) parameter recovery on synthetic data with known true values, (ii) a graded confounding stress test in which the spatial intercept was built to correlate with $\delta^2 H^{\text{OIPC}}_{\text{precip}}$ at four controlled levels, and (iii) a prior-sensitivity analysis that refit the model on real data under seven alternative prior specifications. Tests (i) and (ii) check parameter recovery under controlled conditions. Test (iii) asks something else: do the real-data inferences survive a change of prior?

### *S2.6.1 Parameter recovery*

For the three parameter-recovery scenarios we used the *baseline_veg_sp* spatial structure as a template. Each scenario fixed the data-generating slope and the intercept–OIPC correlation. We drew an independent Gaussian process realization for the spatial intercept, added independent Gaussian noise ($\sigma = 0.3$ in standardized units), and refit the model under the production configuration (8 chains, 3,000 iterations, half warmup).

In Scenario 3a, the simulated slope was uniform across space at $\beta_{\delta^2 H_p} = 0.7$. The posterior recovered a median of 0.71 with 95% credible interval [0.60, 0.82], cleanly containing the simulated value. In Scenario 3b, the simulated slope varied spatially (tropics 0.5, high-latitude 0.9, global mean 0.65), and the posterior recovered a median of 0.71 [0.59, 0.81], containing the simulated global mean. Both scenarios used a spatial intercept independent of $\delta^2 H^{\text{OIPC}}_{\text{precip}}$ ($\rho_c = 0$, where $\rho_c$ denotes the constructed correlation between the synthetic spatial intercept and $\delta^2 H^{\text{OIPC}}_{\text{precip}}$). The model recovers both globally constant and spatially varying slopes when the spatial intercept is independent of the predictor.

In Scenario 3c, the simulated slope was uniform at $\beta_{\delta^2 H_p} = 0.7$ but the spatial intercept was constructed to correlate with $\delta^2 H^{\text{OIPC}}_{\text{precip}}$. The posterior recovered a median of 0.92 [0.84, 0.99], substantially higher than the simulated value and with a credible interval that did not contain it. This result motivated the systematic confounding stress test described next.

### *S2.6.2 Spatial confounding stress test*

We constructed synthetic datasets in which the spatial intercept was correlated with the locally-weighted $\delta^2 H^{\text{OIPC}}_{\text{precip}}$ predictor at four controlled levels: $\rho_c$ = 0.0, 0.3, 0.45, and 0.5. The $\rho_c$ = 0.45 level was chosen to match the empirical correlation between posterior-mean spatial intercepts and $\delta^2 H^{\text{OIPC}}_{\text{precip}}$ observed in the real-data spatial-model fits (Section 3.2: r = 0.39–0.51 across spatial-model variants). Following Paciorek (2010) and Dupont et al. (2022), the synthetic intercept was constructed as

$$z_{\text{confound}}(s) = \rho_c \cdot \sigma_z \cdot \text{OIPC}_{\text{std}}(s) + \sqrt{1 - \rho_c^2} \cdot z_{\text{indep}}(s) \tag{S25}$$

where $z_{\text{indep}}$ is a Gaussian process draw with the empirical Matérn 3/2 covariance (length scale 3,700 km, amplitude $\sigma_z$ matching the empirical intercept SD of *baseline_sp*). The same $z_{\text{indep}}$ draw was used across all four scenarios so only $\rho_c$ varied. Synthetic $\delta^2\text{H}_{\text{wax}}$ was constructed as $z_{\text{confound}} + \beta_{\text{sim}} \cdot \text{OIPC} + \varepsilon$ with $\sigma_\varepsilon$ = 0.3 in standardized units, then re-standardized before fitting; the simulated slope was correspondingly transformed to re-standardized space.

The recovered slope estimates were graded with $\rho_c$ (Table S4). At $\rho_c$ = 0, the posterior median was within 0.06 of the simulated value and the 95% credible interval contained it, so the spatial GP correctly absorbs the spatial intercept structure when the intercept is independent of the predictor. At higher correlation levels, the bias grew: +0.21 at $\rho_c$ = 0.3, +0.28 at $\rho_c$ = 0.45, and +0.30 at $\rho_c$ = 0.5. The credible intervals at $\rho_c \geq 0.3$ did not contain the simulated slope. The bias is unidirectional (always positive), graded with $\rho_c$, and most consequential at the empirical level: at $\rho_c \approx 0.45$ the bias of +0.28 is comparable in magnitude to the slope reduction the spatial GP delivers in real data (~0.20, from the 0.78 non-spatial baseline to 0.53–0.62).

This pattern is consistent with established spatial-confounding theory. When a predictor and the spatial random effect share similar spatial structure, they are not separately identifiable; the model's prior structure determines how shared variance is allocated between them (Reich et al., 2006; Hodges and Reich, 2010; Paciorek, 2010). In our setup the GP and the OIPC field both vary at continental scales (~3,700 km), so the prior structure of the GP and the centered, weakly informative prior on $\beta_{\delta^2\text{H}_p}$ (Table S5) allocate a portion of the shared variance to the slope rather than absorbing all of it through the GP.

### *S2.6.3 Implications for the reported slope*

The simulation results show that the spatially corrected slope can remain biased upward when the predictor and spatial intercept share continental-scale structure. The bias is unidirectional and persistent at empirical confounding levels in the stress test, so the real-data slope reported in Section 3.2 (0.53–0.62 across spatial-model variants) should be interpreted as spatially adjusted, not as a causal estimate. The simulation also quantifies how much confounding the spatial GP absorbs: at empirical $\rho_c$ = 0.45 (re-standardized space), the OLS estimate on the synthetic data was 0.838 (confounded), the spatial GP recovered 0.656, and the simulated slope was 0.381. The spatial GP therefore closed (0.838 - 0.656) / (0.838 - 0.381) ≈ 40% of the OLS-to-simulation gap, leaving about 60% of the confounding bias on the slope. Methods that explicitly orthogonalize the predictor against the spatial field – restricted spatial regression (Reich et al., 2006; Hanks et al., 2015) and Spatial+ (Dupont et al., 2022) – remove the predictor's spatial component before estimating the slope and could further reduce this bias. Implementing them would require changes to the model structure and is left to future work.

### *S2.6.4 Prior sensitivity*

To test sensitivity to prior specification, we refit the *baseline_veg_sp* model on the real data under the reference prior and seven alternative prior specifications (Table S5). These alternatives widened, shifted, or weakened the prior on $\beta_{\delta^2\text{H}_p}$; relaxed the PC prior on $\sigma_{\text{slope}}$; and shifted the GP length-scale prior toward shorter or longer spatial scales. Across all prior variants, the posterior median of $\beta_{\delta^2\text{H}_p}$ ranged from 0.614 to 0.638, a spread of less than 0.03, and the 95% credible intervals overlapped almost entirely. Inferences on the global slope are therefore robust to reasonable variation in prior specification, and the upward-bias caveat from Section S2.6.2 is not an artifact of the chosen priors.

## S3 Extended Results

This section reports diagnostics and supporting analyses that complement the main-text results. Section S3.1 examines how spatial integration of the predictor improves OLS prediction independent of the Bayesian framework.

Section S3.2 reports the elevation-effect posterior across all 14 spatial-model variants. Cross-cutting diagnostics for the spatial models – regional in-sample performance, simulation-based confounding stress tests, and prior sensitivity – are reported alongside the methodology in Sections S2.5 and S2.6.

### *S3.1 Spatial Integration*

To evaluate whether spatial integration improves model performance independent of the Bayesian framework, we fit the OLS regression (Figure 1 of the main text) using $\delta^2 H^{\text{OIPC}}_{\text{precip}}$ values averaged over spatial scales from 0 km (point values) to 100 km with exponential distance weighting. Figure S4 shows the regression scatter and fitted line for four representative integration choices (point values, 10 km exponential, equal weights across the pre-computed scales, and the Bayesian-fitted effective scale); Figure S5 sweeps continuously over the integration scale and reports $R^2$ as a function of $\lambda$. Spatial integration consistently improves prediction across all modeling approaches, with optimal OLS scales matching the Bayesian model estimates.

### *S3.2 Environmental Predictors*

Elevation effects on $\delta^2\text{H}_{\text{wax}}$ carry substantial uncertainty across all models (Figure S6). The 95% credible-interval envelope on the elevation–$\delta^2\text{H}_{\text{wax}}$ curve reaches half-widths of up to ~280‰, far exceeding the central trend, which is approximately flat at zero across the full elevation range (~0–5,000 m). The envelope is constructed by design-weighted summation of the B-spline coefficient marginal half-widths and is conservative; the true joint posterior on the curve is narrower because the spline coefficients are partly anti-correlated. Even so, the data place no meaningful constraint on a systematic elevation effect once spatial structure is accounted for. Elevation acts mainly as a proxy for regional patterns rather than as a strong direct predictor of fractionation.

## S4 Predicting $\delta^2\text{H}_{\text{precip}}$ from $\delta^2\text{H}_{\text{wax}}$

Paleoclimate reconstruction of $\delta^2\text{H}_{\text{precip}}$ proceeds through Bayesian inversion of the fitted forward model: for each posterior draw of the model parameters, the inverse is evaluated at the prediction site, and the per-draw values are aggregated into a posterior distribution for $\delta^2\text{H}_{\text{precip}}$ that incorporates regression-parameter uncertainty, residual variance, analytical uncertainty in the wax measurement, and (for spatial models) spatial prediction uncertainty at the new location from the fitted spatial basis. The R package implementing this inversion is `leafwax` (`https://github.com/bradleylab/leafwax`). The equations in this section describe the conceptual inversion the package implements; per-record implementation details (closed-form vs. numerical evaluation of the per-draw inverse, handling of missing covariates via marginalization over regional distributions) are documented in the package vignettes.

### *S4.1 Bayesian Inversion Framework*

Recovering $\delta^2\text{H}_{\text{precip}}$ from a measured $\delta^2\text{H}_{\text{wax}}$ means inverting the calibrated forward models. We do this with a posterior predictive inversion that propagates calibration, slope, spatial, and analytical uncertainty. No informative prior is placed on $\delta^2\text{H}_{\text{precip}}$; the implicit prior comes from the OIPC range seen during calibration and from the calibration posterior itself. That makes the procedure a posterior predictive inversion under weak implicit priors rather than a fully Bayesian inversion with a stated reconstruction prior. For a new leaf wax measurement $\delta^2\text{H}_{\text{wax}}$ with analytical uncertainty $\sigma_{\text{analytical}}$, the inversion samples from the joint posterior distribution:

$$p\left(\delta^2 H_{\text{precip}} \mid \delta^2 H_{\text{wax,obs}}, \mathbf{x}^*\right) \propto p\left(\delta^2 H_{\text{wax,obs}} \mid \delta^2 H_{\text{precip}}, \mathbf{x}^*\right)\, p\left(\delta^2 H_{\text{precip}}\right) \tag{S26}$$

where $\mathbf{x}^*$ represents the environmental covariates at the prediction location (coordinates, elevation, $C_4$ fraction, PFT, precipitation) and $p\left(\delta^2 H_{\text{precip}}\right)$ is a weakly informative or flat prior used to regularize the per-draw inverse where required (the implementation is otherwise dominated by the likelihood in well-constrained regions).

For each draw $i$ from the posterior distribution of model parameters obtained during calibration, the per-draw inverse follows the linearized form:

$$\delta^2 H^{(i)}_{\text{precip}} = \frac{\delta^2 H_{\text{wax,obs}} - \beta_0^{(i)}(s^*) - \mathbf{f}^{(i)}(\mathbf{x}^*)}{\beta^{(i)}_{\text{eff}}(s^*, \mathbf{x}^*)} \tag{S27}$$

where the superscript *(i)* indicates the *i*-th posterior draw, $\beta_0^{(i)}(s^*)$ is the spatially-varying intercept evaluated at the prediction site $s^*$, $\mathbf{f}^{(i)}(\mathbf{x}^*)$ is the contribution of additive covariates (elevation, vegetation main effects, precipitation, etc.) at the new location, and $\beta_{\text{eff}}^{(i)}(s^*, \mathbf{x}^*)$ is the location- and covariate-specific effective slope on $\delta^2 H_{\text{precip}}$ obtained by combining the global slope, the spatially-varying slope contribution, and the $\delta^2\text{H}_{\text{precip}} \times$ vegetation interaction contributions for the model variant in question. For non-interactive non-spatial variants $\beta_{\text{eff}}^{(i)}$ reduces to the global $\beta_{\delta^2\text{H}_p}^{(i)}$; for the *full_interact_sp* variant it carries spatial-slope and interaction terms.

To incorporate measurement uncertainty, we add Gaussian noise to the observed value:

$$\delta^2 H_{wax,obs}^{(i)} \sim \mathcal{N}\left(\delta^2 H_{wax,obs}, \left(\sigma_{\text{analytical}}^*\right)^2 + \left(\sigma^{(i)}\right)^2\right) \tag{S28}$$

where $\sigma^{(i)}$ is the residual standard deviation from the *i*-th posterior draw. This ensures that analytical and residual calibration uncertainty are propagated through the inversion. The posterior reconstruction uncertainty includes:

1. Analytical uncertainty in the measured $\delta^2\text{H}_{\text{wax}}$ value.
2. Residual calibration uncertainty, represented by $\sigma^{(i)}$ in wax-isotope space.
3. Parameter uncertainty, propagated by evaluating the inverse across the full posterior distribution of model parameters.
4. Spatial prediction uncertainty in the fitted spatial-basis terms at new locations, for spatial model variants.

For locations with missing covariate data (e.g., unknown elevation), we marginalize over plausible values based on regional distributions, appropriately inflating the predictive uncertainty. The final posterior distribution

$$p\left(\delta^2 H_{precip} \mid \delta^2 H_{wax}^*, \mathbf{x}^*\right) \tag{S29}$$

is represented through Monte Carlo samples, from which we compute summary statistics (mean, median, credible intervals) for reporting.

The inversion relies on assumptions of stationarity — the spatially varying regression parameters relating $\delta^2\text{H}_{\text{precip}}$ to $\delta^2\text{H}_{\text{wax}}$ do not vary through time, and space-for-time transferability — that the modern spatial calibration is applicable to temporal changes at a single site.

Abatzoglou, J. T., Dobrowski, S. Z., Parks, S. A., Hegewisch, K. C., 2018. Terraclimate, a high-resolution global dataset of monthly climate and climatic water balance from 1958-2015. Sci. Data. 5, 170191.

Amatulli, G., Domisch, S., Tuanmu, M.-N., Parmentier, B., Ranipeta, A., Malczyk, J., Jetz, W., 2018. A suite of global, cross-scale topographic variables for environmental and biodiversity modeling.

Banerjee, S., Gelfand, A. E., Finley, A. O., Sang, H., 2008. Gaussian predictive process models for large spatial data sets. J. R. Stat. Soc. Series B Stat. Methodol. 70, 825–848.

Bolker, B. M., 2008. Ecological models and data in R. Princeton University Press, Princeton, NJ.

Bowen, G. J., 2018. Gridded maps of the isotopic composition of meteoric waters.

Bowen, G. J., Revenaugh, J., 2003. Interpolating the isotopic composition of modern meteoric precipitation. Water Resour. Res. 39, 1–13.

Chang, Q., Hren, M., Lin, A. T., Tabor, C., Yu, S.-W., Eley, Y., Harris, G., 2021. Terrestrial biomarker isotope records of late quaternary climate and source-to-sink sediment transport processes in southwestern taiwan. Am. J. Sci. 321, 393–423.

Collins, J. A., Schefuß, E., Mulitza, S., Prange, M., Werner, M., Tharammal, T., Paul, A., Wefer, G., 2013. Estimating the hydrogen isotopic composition of past precipitation using leaf-waxes from western africa. Quat. Sci. Rev. 65, 88–101.

Corcoran, M. C., Diefendorf, A. F., Lowell, T. V., Hall, B. L., Spoth, M. M., Schartman, A., Brickle, P., 2022. Hydrogen and carbon isotope fractionation in modern plant wax n-alkanes from the falkland islands. Org. Geochem. 166, 104404.

Daniels, W. C., Russell, J. M., Morrill, C., Longo, W. M., Giblin, A. E., Holland-Stergar, P., Welker, J. M., Wen, X., Hu, A., Huang, Y., 2021. Lacustrine leaf wax hydrogen isotopes indicate strong regional climate feedbacks in beringia since the last ice age. Quat. Sci. Rev. 269, 107130.

Danielson, J. J., Gesch, D. B., 2011. Global multi-resolution terrain elevation data 2010 (GMTED2010). U.S. Geological Survey.

Diggle, P. J., Ribeiro, P. J. J. r., 2007. Model-Based Geostatistics. Springer, New York, NY.

Dupont, E., Wood, S. N., Augustin, N. H., 2022. Spatial+: A novel approach to spatial confounding. Biometrics 78, 1279–1290.

Eensalu, M., Nelson, D. B., Buczynska, A., Rach, O., Klein, E. S., Dodd, J. P., Poska, A., Stansell, N. D., 2023. Hydrogen isotope biogeochemistry of plant waxes in paired lake catchments. Org. Geochem. 185, 104674.

Feakins, S. J., 2013. Pollen-corrected leaf wax d/h reconstructions of northeast african hydrological changes during the late miocene. Palaeogeogr. Palaeoclimatol. Palaeoecol. 374, 62–71.

Feakins, S. J., Bentley, L. P., Salinas, N., Shenkin, A., Blonder, B., Goldsmith, G. R., Ponton, C., Arvin, L. J., Wu, M. S., Peters, T., West, A. J., Martin, R. E., Enquist, B. J., Asner, G. P., Malhi, Y., 2016. Plant leaf wax biomarkers capture gradients in hydrogen isotopes of precipitation from the andes and amazon. Geochim. Cosmochim. Acta. 182, 155–172.

Fieller, E. C., 1954. Some problems in interval estimation. J. R. Stat. Soc. Series B Stat. Methodol. 16, 175–185.

Finley, A. O., Sang, H., Banerjee, S., Gelfand, A. E., 2009. Improving the performance of predictive process modeling for large datasets. Comput. Stat. Data Anal. 53, 2873–2884.

Friedl, M., Sulla-Menashe, D., 2019. MCD12Q1 MODIS/Terra+Aqua Land Cover Type Yearly L3 Global 500m SIN Grid V006. NASA EOSDIS Land Processes Distributed Active Archive Center.

Fuglstad, G.-A., Simpson, D., Lindgren, F., Rue, H., 2019. Constructing priors that penalize the complexity of gaussian random fields. J. Am. Stat. Assoc. 114, 445–452.

Gaviria-Lugo, N., Läuchli, C., Wittmann, H., Bernhard, A., Frings, P., Mohtadi, M., Rach, O., Sachse, D., 2023. Climatic controls on leaf wax hydrogen isotope ratios in terrestrial and marine sediments along a hyperarid-to-humid gradient. Biogeosciences 20, 4433–4453.

Gensel, J., Humphries, M. S., Zabel, M., Sebag, D., Hahn, A., Schefuß, E., 2022. Origin, transport, and retention of fluvial sedimentary organic matter in South Africa's largest freshwater wetland, Mkhuze Wetland System. Biogeosciences 19, 2881–2902.

Hanks, E. M., Schliep, E. M., Hooten, M. B., Hoeting, J. A., 2015. Restricted spatial regression in practice: geostatistical models, confounding, and robustness under model misspecification. Environmetrics 26, 243–254.

Heaton, M. J., Datta, A., Finley, A. O., Furrer, R., Guinness, J., Guhaniyogi, R., Gerber, F., Gramacy, R. B., Hammerling, D., Katzfuss, M., Lindgren, F., Nychka, D. W., Sun, F., Zammit-Mangion, A., 2019. A case study competition among methods for analyzing large spatial data. J. Agric. Biol. Environ. Stat. 24, 398–425.

Hodges, J. S., Reich, B. J., 2010. Adding spatially-correlated errors can mess up the fixed effect you love. Am. Stat. 64, 325–334.

Hren, M. T., Brandon, M. T., 2026. A process-based model of precipitation isotopes, orographic lifting and leaf wax $\delta^2$h across the tibetan plateau and south asia. Paleoceanography and Paleoclimatology 41 (1), e2025PA005167.

IAEA/WMO, 2015. Global network of isotopes in precipitation. the GNIP database.

Jaccard, J. J., Turrisi, R., Wan, C. K., 2003. Interaction Effects in Multiple Regression, 2nd Edition. SAGE Publications, Thousand Oaks, CA.

Konecky, B., Russell, J., Bijaksana, S., 2016. Glacial aridity in central indonesia coeval with intensified monsoon circulation. Earth Planet. Sci. Lett. 437, 15–24.

Konecky, B. L., Dee, S. G., Noone, D. C., 2019. Waxpsm: A forward model of leaf wax hydrogen isotope ratios to bridge proxy and model estimates of past climate. J. Geophys. Res. Biogeosci. 124, 2107–2125.

Ladd, S. N., Maloney, A. E., Nelson, D. B., Prebble, M., Camperio, G., Sear, D. A., Hassall, J. D., Langdon, P. G., Sachs, J. P., Dubois, N., 2021. Leaf wax hydrogen isotopes as a hydroclimate proxy in the tropical pacific. J. Geophys. Res. Biogeosci. 126.

Liu, J., An, Z., 2019. Variations in hydrogen isotopic fractionation in higher plants and sediments across different latitudes: Implications for paleohydrological reconstruction. Sci. Total Environ. 650, 470–478.

Luo, X., Zhou, H., Satriawan, T. W., Tian, J., Zhao, R., Keenan, T. F., Griffith, D. M., Sitch, S., Smith, N. G., Still, C. J., 2024. Mapping the global distribution of c4 vegetation using observations and optimality theory. Nat. Commun. 15, 1219.

Martins, G. S., Cordeiro, R. C., Turcq, B., Meyers, P. A., Mendez-Millan, M., Moreira, L. S., Fontes, D., Rodrigues, R. A., Sifeddine, A., Behling, H., Bouloubassi, I. D., 2022. Late quaternary hydrological changes in the southeastern amazon basin from n-alkane molecular and isotopic records in sediments of saci lake, pará state (brazil). Glob. Planet. Change. 213, 103833.

McClelland, H. L. O., Halevy, I., Wolf-Gladrow, D. A., Evans, D., Bradley, A. S., 2021. Statistical uncertainty in paleoclimate proxy reconstructions. Geophys. Res. Lett. 48, 1–11.

McFarlin, J. M., Axford, Y., Masterson, A. L., Osburn, M. R., 2019. Calibration of modern sedimentary $\delta$2h plant wax-water relationships in greenland lakes. Quat. Sci. Rev. 225, 105978.

National Research Council, 2006. Surface Temperature Reconstructions for the Past 2,000 Years. The National Academies Press, Washington, DC.
Nieto-Moreno, V., Rohrmann, A., van der Meer, M. T. J., Sinninghe Damsté, J. S., Sachse, D., Tofelde, S., Niedermeyer, E. M., Strecker, M. R., Mulch, A., 2016. Elevation-dependent changes in *n*-alkane $\delta$d and soil GDGTs across the South Central Andes. Earth Planet. Sci. Lett. 453, 234–242.
Paciorek, C. J., 2010. The importance of scale for spatial-confounding bias and precision of spatial regression estimators. Stat. Sci. 25, 107–125.
Polissar, P. J., D'Andrea, W. J., 2014. Uncertainty in paleohydrologic reconstructions from molecular $\delta$d values. Geochim. Cosmochim. Acta. 129, 146–156.
Reich, B. J., Hodges, J. S., Zadnik, V., 2006. Effects of residual smoothing on the posterior of the fixed effects in disease-mapping models. Biometrics 62, 1197–1206.
Repasch, M., Scheingross, J. S., Hovius, N., Lupker, M., Wittmann, H., Haghipour, N., Gröcke, D. R., Orfeo, O., Eglinton, T. I., Sachse, D., 2021. Fluvial organic carbon cycling regulated by sediment transit time and mineral protection. Nat. Geosci. 14, 842–848.
Roberts, D. R., Bahn, V., Ciuti, S., Boyce, M. S., Elith, J., Guillera-Arroita, G., Hauenstein, S., Lahoz-Monfort, J. J., Schröder, B., Thuiller, W., Warton, D. I., Wintle, B. A., Hartig, F., Dormann, C. F., 2017. Cross-validation strategies for data with temporal, spatial, hierarchical, or phylogenetic structure. Ecography (Cop.). 40, 913–929.
Roy, B., Sanyal, P., 2022. Isotopic and molecular distribution of leaf-wax in plant-soil system of the Gangetic floodplain and its implication for paleorecords. Quaternary International 607, 89–99.
Sachse, D., Billault, I., Bowen, G. J., Chikaraishi, Y., Dawson, T. E., Feakins, S. J., Freeman, K. H., Magill, C. R., Mcinerney, F. A., Meer, M. T. J. V. D., Polissar, P., Robins, R. J., Sachs, J. P., Schmidt, H.-L., Sessions, A. L., White, J. W. C., West, J. B., 2012. Molecular paleohydrology : Interpreting the hydrogen-isotopic composition of lipid biomarkers from photosynthesizing organisms. Annual Review of Earth and Planetary Sciences 40, 221–252.
Sessions, A. L., Hayes, J. M., 2005. Calculation of hydrogen isotopic fractionations in biogeochemical systems. Geochim. Cosmochim. Acta. 69, 593–597.
Simpson, D., Rue, H., Riebler, A., Martins, T. G., Sørbye, S. H., 2017. Penalising model component complexity: A principled, practical approach to constructing priors.
Stein, M. L., 1999. Interpolation of spatial data, 1999th Edition. Springer, New York, NY.
Still, C. J., Berry, J. A., Collatz, G. J., DeFries, R. S., 2003. Global distribution of $c_3$ and $c_4$ vegetation: Carbon cycle implications. Global Biogeochem. Cycles. 17, 6–1–6–14.
Struck, J., Bliedtner, M., Strobel, P., Bittner, L., Bazarradnaa, E., Andreeva, D., Zech, W., Glaser, B., Zech, M., Zech, R., 2020. Leaf waxes and hemicelluloses in topsoils reflect the $\delta^2$H and $\delta^{18}$O isotopic composition of precipitation in Mongolia. Frontiers in Earth Science 8, 343.
Swinbank, R., Purser, R. J., 2006. Fibonacci grids: A novel approach to global modelling. Q. J. R. Meteorol. Soc. 132, 1769–1793.
Tierney, J. E., Russell, J. M., Huang, Y., Damsté, J. S. S., Hopmans, E. C., Cohen, A. S., 2008. Northern hemisphere controls on tropical southeast african climate during the past 60,000 years. Science 322, 252–255.
Tipple, B. J., Berke, M. A., Doman, C. E., Khachaturyan, S., Ehleringer, J. R., 2013. Leaf-wax n-alkanes record the plant–water environment at leaf flush. Proceedings of the National Academy of Sciences 110 (7), 2659–2664.
Utida, G., Cruz, F. W., Etourneau, J., Bouloubassi, I., Schefuß, E., Vuille, M., Novello, V. F., Prado, L. F., Sifeddine, A., Klein, V., Zular, A., Viana, J. C. C., Turcq, B., 2019. Tropical south atlantic influence on northeastern brazil precipitation and ITCZ displacement during the past 2300 years. Sci. Rep. 9, 1698.
Wang, Y.-P., Luo, T., Chen, J., Zhan, Z.-W., Song, Z., Xing, L., He, D., 2023. Influence of salinity on hydrogen isotope fractionation of n-alkanes in mangrove leaves and surface sediments: A comparison across various geomorphological settings. Chem. Geol. 634, 121589.
Wang, Y. V., Larsen, T., Leduc, G., Andersen, N., Blanz, T., Schneider, R. R., 2013. What does leaf wax $\delta$d from a mixed c3/c4 vegetation region tell us? Geochim. Cosmochim. Acta. 111, 128–139.
Wood, S. N., 2017. Generalized additive models. Chapman and Hall/CRC, Boca Raton, FL.
Zhao, B., Russell, J. M., Blaus, A., de Novaes Nascimento, M., Freeman, A., Bush, M. B., 2024. Tropical andean climate variations since the last deglaciation. Proc. Natl. Acad. Sci. U. S. A. 121, e2320143121.

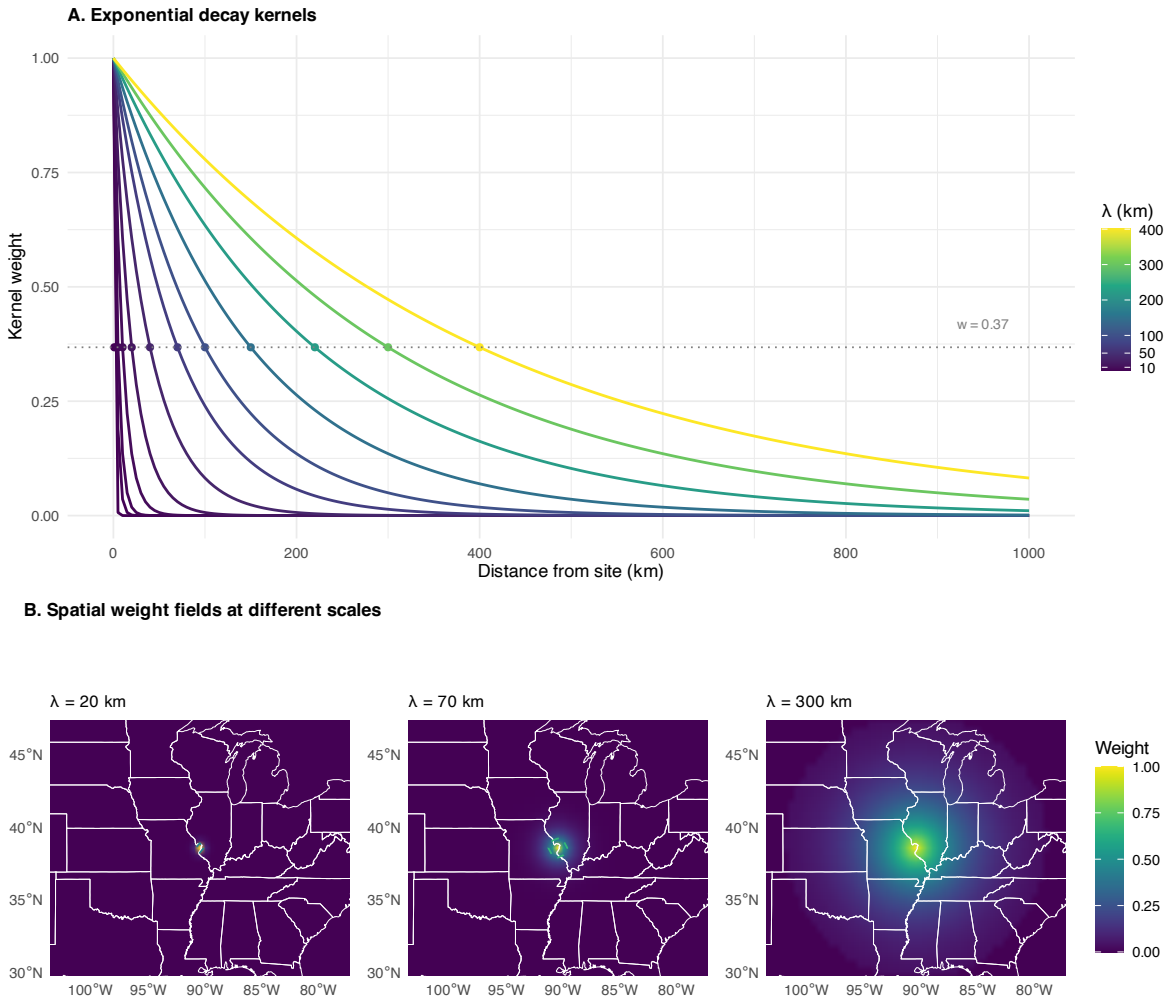


Figure S1: **Spatial weighting scheme for addressing spatial autocorrelation.** (A) Exponential decay kernels showing how observation weights decline with distance for different integration scales ($\lambda$). The horizontal dashed line indicates w = 0.37 (1/e), showing the distance at which weights have decayed to ~37% of their maximum value. (B) Example spatial weight fields centered on a site in the central United States for three different integration scales ($\lambda$ = 20, 70, and 300 km). Warmer colors indicate higher weights.

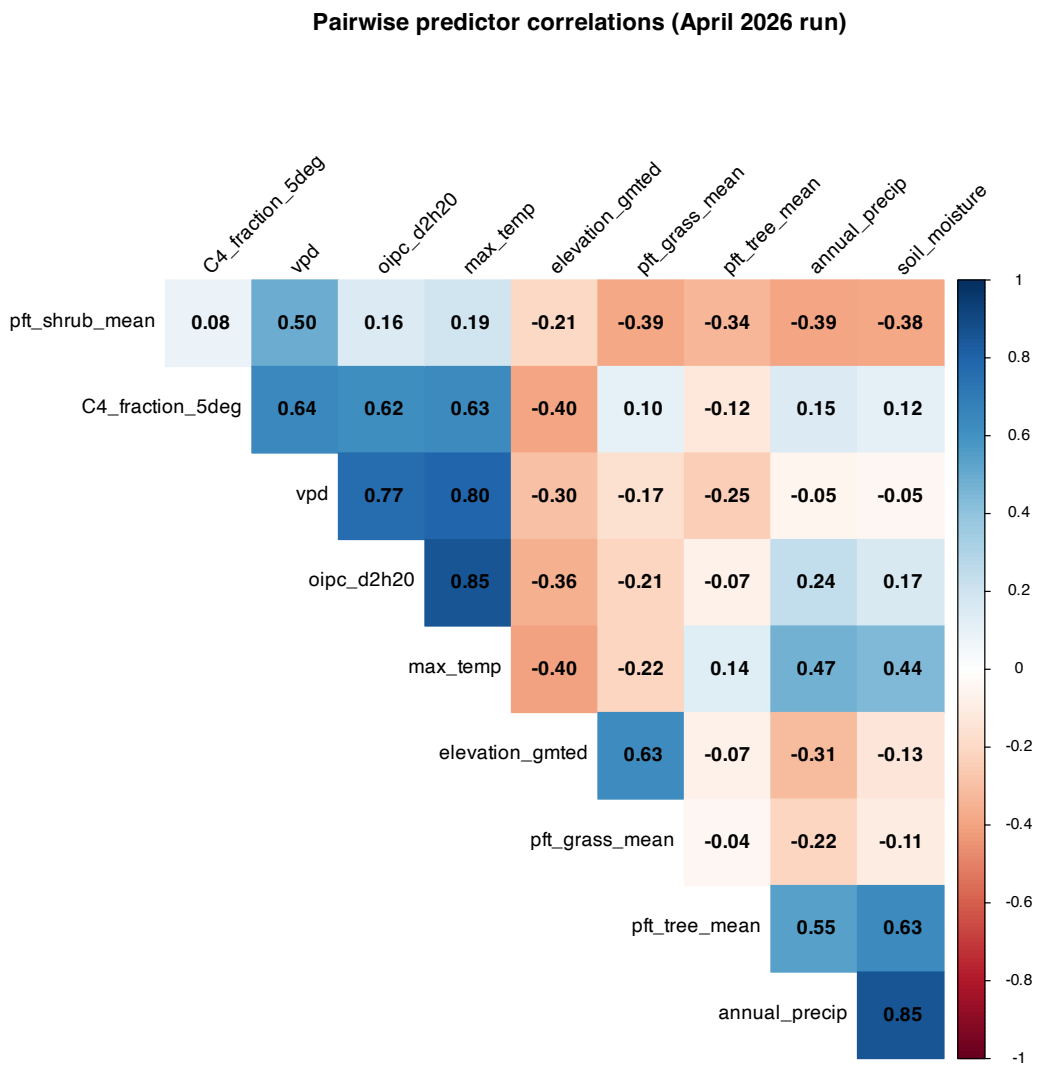


Figure S2: **Pairwise correlations among environmental predictors and response variable.** Correlation matrix showing Pearson correlation coefficients between all variables before multicollinearity filtering. Strong correlations ($|r| > 0.7$) are observed between $\delta^2H_{wax}$ and several climate variables ($\delta^2H^{OIPC}_{precip}$**: r = +0.80; VPD: r = +0.71**), and among climate variables themselves (**VPD and max temperature: r = 0.80; annual precipitation and soil moisture: r = 0.85**). Variables with high collinearity were excluded from final models to avoid multicollinearity issues (see Methods).

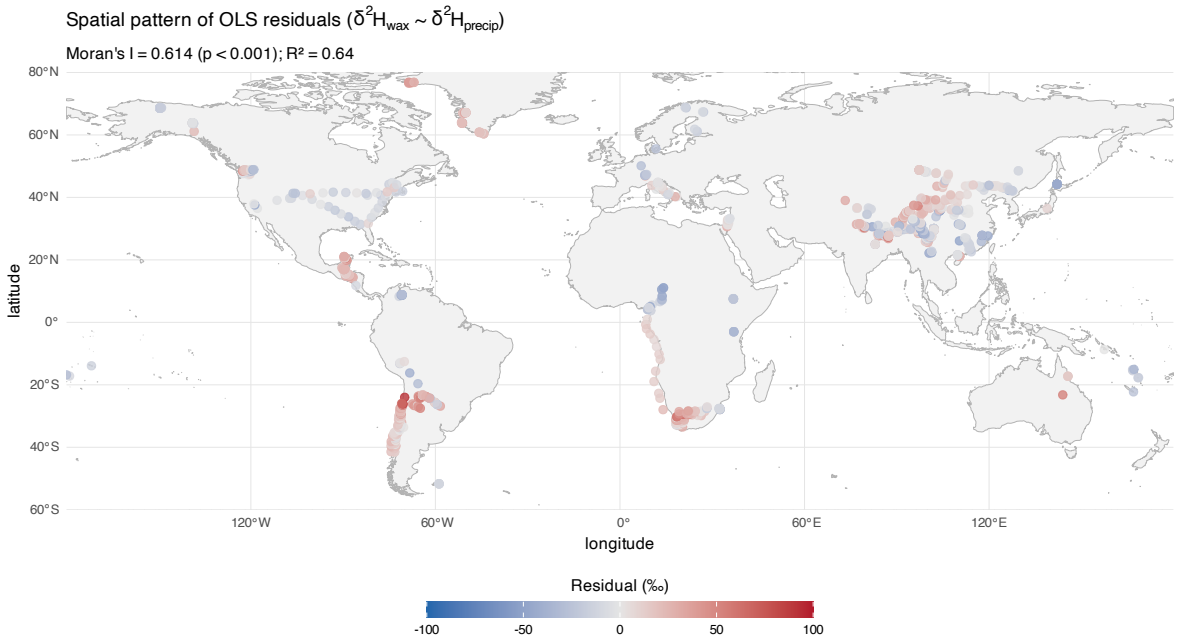


Figure S3: **Spatial autocorrelation in OLS regression residuals.** Map showing residuals from the ordinary least squares regression of $\delta^2 H_{wax}$ $\delta^2 H^{OIPC}_{precip}$ (Figure 1). Points are colored by residual magnitude (blue = negative residuals, red = positive residuals). Significant spatial autocorrelation is evident (**Moran's I = 0.584, p < 0.001**), with clusters of similar residuals indicating that the non-spatial model fails to capture spatially structured variation. This motivates the use of spatial Gaussian process models to account for spatial autocorrelation.

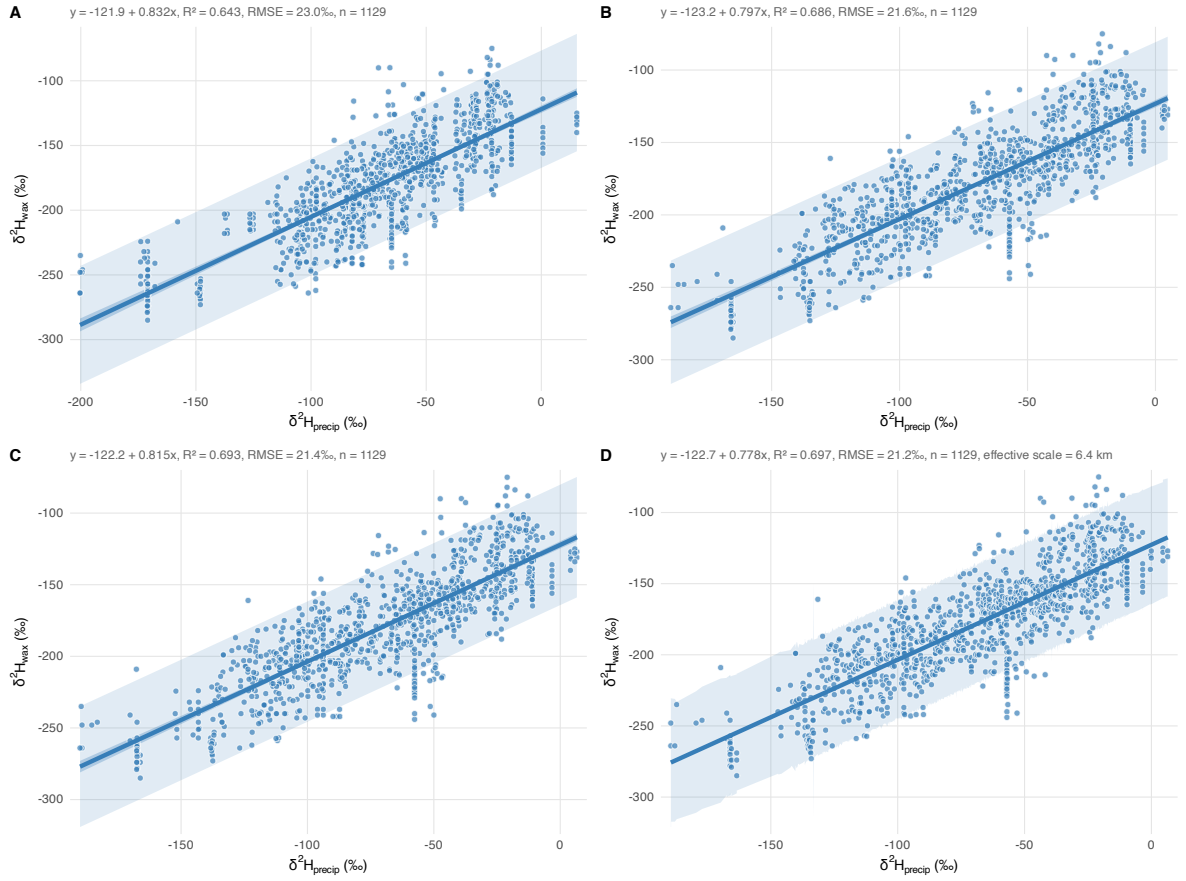


Figure S4: **OLS regression under alternative spatial-integration choices for the predictor.** Each panel shows the same n = 1,129 surface sediment and soil samples regressed against $\delta^2 H^{\mathrm{OIPC}}_{\mathrm{precip}}$, with the predictor field summarized at the sample location in four different ways. **(A)** Point values from the OIPC raster cell containing the sample (slope = 0.832, $R^2$ = 0.643, RMSE = 23.0‰; reproduced as Figure 1 of the main text). **(B)** Exponential distance-weighted average at a 10 km integration scale (slope = 0.797, $R^2$ = 0.686, RMSE = 21.6‰). **(C)** Equal-weight average across the nine pre-computed scales of 1–150 km (slope = 0.815, $R^2$ = 0.693, RMSE = 21.4‰). **(D)** Bayesian-fitted exponential integration at the model's posterior-mean effective scale of 6.4 km (slope = 0.778, $R^2$ = 0.697, RMSE = 21.2‰). Spatial integration modestly improves fit ($R^2$ from 0.643 to 0.697; RMSE from 23.0‰ to 21.2‰) and changes the effective precipitation-isotope predictor used in the calibration. The slope in panel D matches the baseline non-spatial Bayesian model's posterior median used throughout the main text.

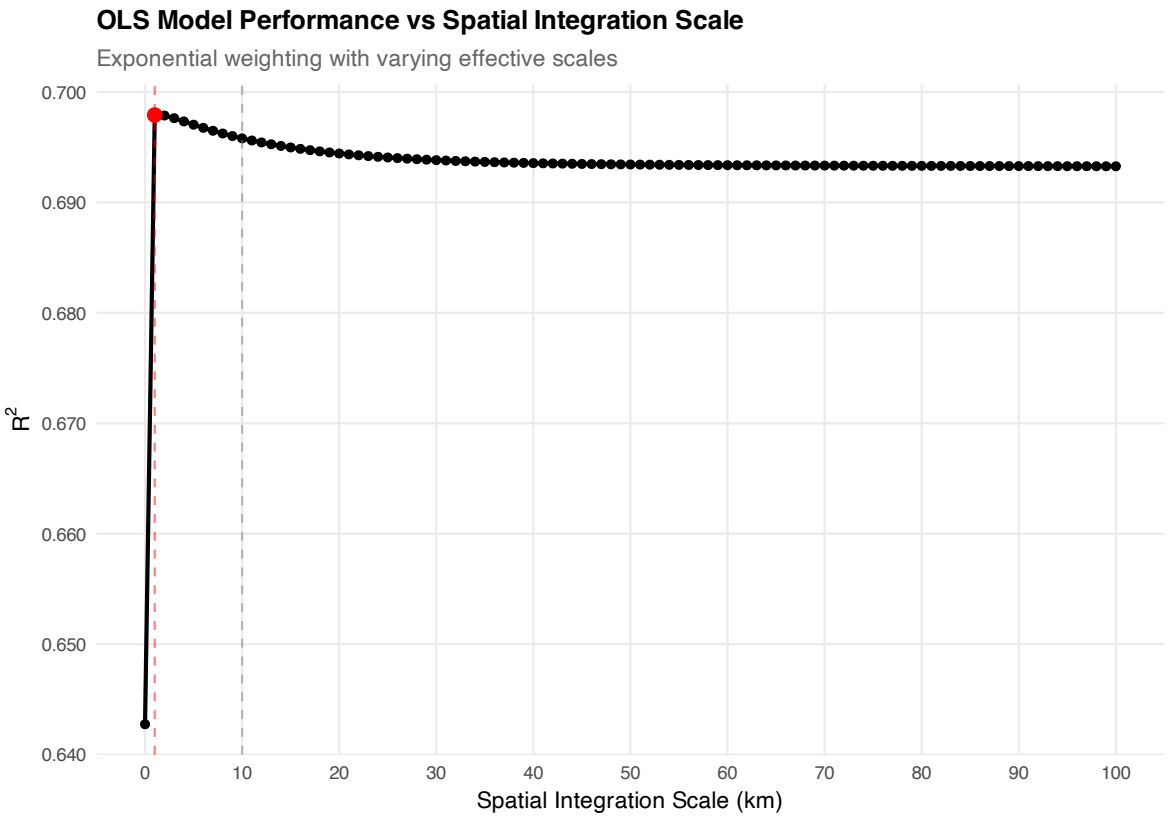


Figure S5: **Optimization of spatial integration scale for weighted regression.** Model performance ($R^2$) as a function of spatial integration scale ($\lambda$) using exponentially weighted ordinary least squares regression. The red point indicates the optimal scale that maximizes $R^2$. Performance improves sharply from point values ($\lambda$ **= 0 km, $R^2$ = 0.643**) to the Bayesian model's fitted scale (**$R^2$ = 0.695**), then plateaus for larger scales. The gray dashed line shows $\lambda$ = 10 km for reference. This analysis informed the choice of exponential decay weighting in the Gaussian process models.

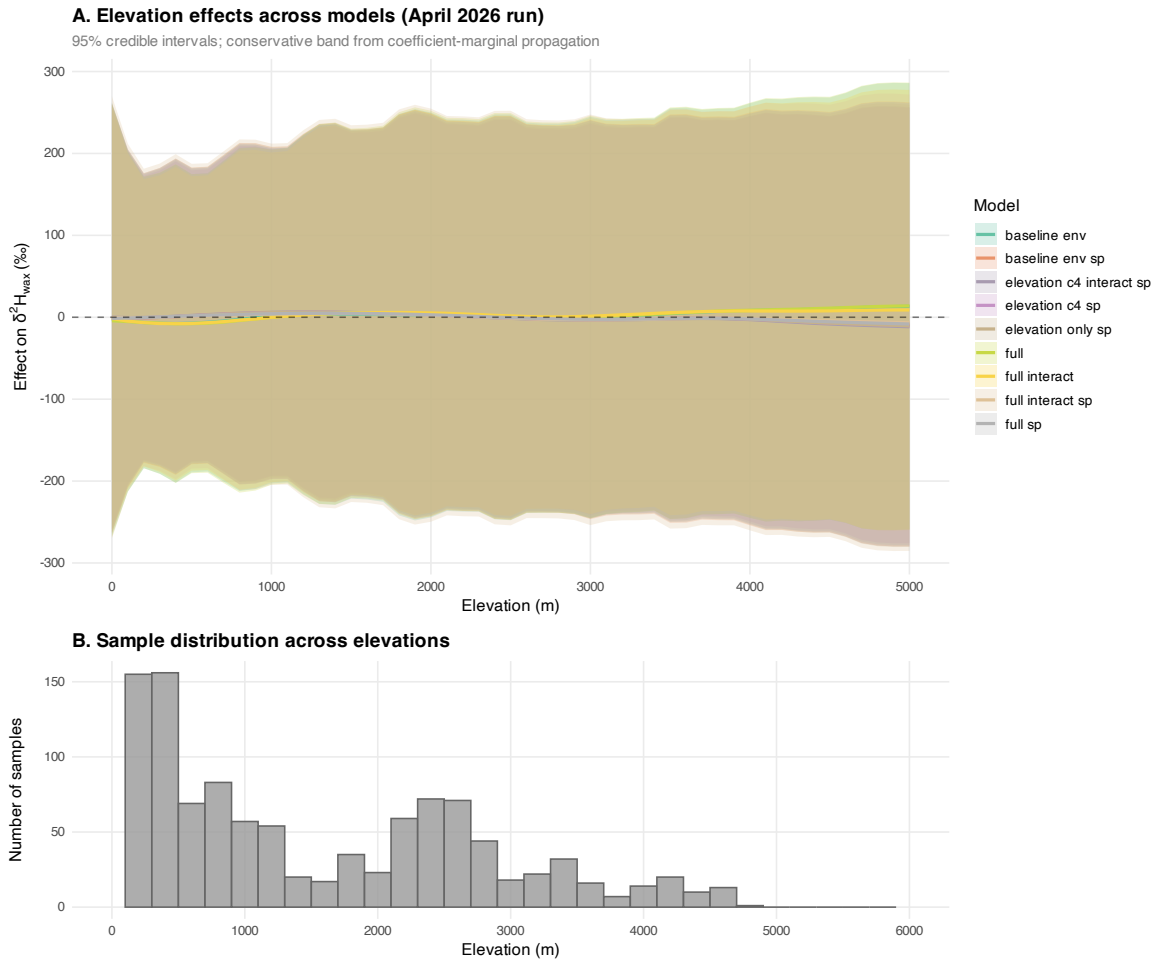


Figure S6: **Elevation effects across models.** **(A)** Estimated B-spline elevation effect on $\delta^2H_{wax}$ for the nine model variants that include elevation (six spatial, three non-spatial). Lines show the posterior-mean curve for each model; shaded ribbons show 95% credible-interval envelopes constructed from coefficient-marginal half-widths (a conservative band that ignores anti-correlations among basis coefficients). The envelope half-width reaches **up to ~280‰**, far exceeding any systematic central trend. **(B)** Histogram of sample distribution across elevations (bin width = 250 m).

Table S1: Compilation sources for the global *n*-$C_{29}$ $\delta^2H_{wax}$ database (n = 1,129). "*n* samples" is the count of calibration sites contributed by each source. Several entries (ETH Zurich, Liu and An, McFarlin, Ladd, manual extraction) are themselves compilations of multiple primary publications; "# primary DOIs" indicates how many distinct primary references contribute through each source. Five further rows are populated by direct ingest from individual primary publications. Across all 18 source entries the database aggregates 49 unique primary-publication DOIs.

| Source | *n* samples | # primary DOIs | Notes |
|---|---|---|---|
| ETH Zurich (10.3929/ethz-b-000412154) | 406 | 30 | Multi-study open-access deposit |
| Hren and Brandon (2026) Zenodo:17209981 | 191 | 1 | Recent global re-compilation |
| Liu and An (2019) | 125 | 9 | Asia-focused meta-compilation |
| McFarlin et al. (2019) | 48 | 8 | Greenland + nearby regional sets |
| Manual extraction from primary literature | 45 | 7 | Tables/figures not in deposits |
| Ladd et al. (2021) | 35 | 6 | Tropical Pacific compilation |
| Roy and Sanyal (2022) Table S1 (soil) | 35 | 1 | Tropical India soils |
| Wyoming Data Repository (10.15786/20126483) | 30 | 1 | Standalone calibration deposit |
| Struck et al. (2020) DataSheet1 | 27 | 1 | *Frontiers in Earth Science* |
| NOAA WDS Paleoclimatology study 27790 | 17 | 1 | Database release |
| PANGAEA (10.1594/PANGAEA.859572) | 13 | 1 | Open-access deposit |
| Corcoran et al. (2022) | 5 | 1 | Falkland Islands |
| Roy and Sanyal (2022) Table 2 | 3 | 1 | Subsidiary table |
| *Direct ingest from primary publication:* | | | |
| Gaviria-Lugo et al. (2023) *Biogeosciences* | 67 | 1 | 10.5194/bg-20-4433-2023; hyperarid–humid gradient |
| Repasch et al. (2021) *Nat. Geosci.* | 27 | 1 | 10.1038/s41561-021-00845-7; Rio Bermejo |
| Gensel et al. (2022) *Biogeosciences* | 23 | 1 | 10.5194/bg-19-2881-2022; Mkhuze Wetland, S. Africa |
| Nieto-Moreno et al. (2016) *EPSL* | 19 | 1 | 10.1016/j.epsl.2016.07.049; S. Central Andes |
| Wang et al. (2023) *Chem. Geol.* | 13 | 1 | 10.1016/j.chemgeo.2023.121589; mangrove leaves & sediments |
| **Total** | **1,129** | **49 unique** | |

**Table S2.** Prior distributions used in the geospatial Bayesian leaf wax model

| Parameter | Description | Prior | Informativeness | Justification |
|---|---|---|---|---|
| $\beta_0$ | Global intercept for $\delta^2H_{wax}$ | normal(0, 5) | Weakly informative | Wide SD allows intercept to adapt to data; centered at 0 for standardized $\delta^2H_{wax}$ |
| $\beta_{\delta^2H_p}$ | Global coefficient for $\delta^2H_{precip}$ | normal(0.8, 0.3) | Weakly informative | Centered near the OLS estimate; 95% prior interval [0.21, 1.39]; posterior medians (0.53–0.62) sit 2–3 SDs from the prior mean and are stable across wider priors (Table S5), confirming the prior is data-dominated. |
| $\lambda_{decay}$ | Exponential decay for spatial scale weighting | lognormal(2.5, 0.5) | Weakly informative | Centers at ~12 km based on preliminary analysis; allows flexibility |
| $\beta_{C4}$ | $C_4$ fraction coefficient | normal(0, 2) | Weakly informative | Centered at 0 with wide SD |
| $\beta_{tree}$ | Tree fraction coefficient | normal(0, 2) | Weakly informative | Centered at 0 with wide SD |
| $\beta_{shrub}$ | Shrub fraction coefficient | normal(0, 2) | Weakly informative | Centered at 0 with wide SD |
| $\beta_{grass}$ | Grass fraction coefficient | normal(0, 2) | Weakly informative | Centered at 0 with wide SD |
| $\beta_{precip}$ | Precipitation coefficient | normal(0, 0.5) | Moderately informative | Matches interaction prior scale; allows moderate effect while regularizing |
| $\beta_{elev}[k]$ | B-spline coefficients | $\beta_{elev}[1] \sim \text{Normal}(0, 2)$; $\beta_{elev}[k] \sim \text{Normal}(\beta_{elev}[k-1], \tau_{elev})$ for $k > 1$ | Weakly informative on first coefficient; smoothing across the rest | Random-walk prior encourages smooth elevation response |
| $\tau_{elev}$ | Elevation spline smoothness | normal(0, 1) | Moderately informative | Controls smoothness between knots |
| $\sigma_{intercept}$ | SD of spatial intercept GP | exponential($\lambda_{intercept}$) where $\lambda_{intercept} = -\log(0.05)/20$ | PC prior | $P(\sigma > u) = \alpha$; with $u = 20‰$, $\alpha = 0.05$ |
| $\sigma_{slope}$ | SD of spatial slope GP | exponential($\lambda_{slope}$) where $\lambda_{slope} = -\log(0.05)/0.3$ | PC prior | $P(\sigma > u) = \alpha$; with $u = 0.3$, $\alpha = 0.05$ |

Table S2 (continued)

| Parameter | Description | Prior | Informativeness | Justification |
|---|---|---|---|---|
| $\log(\rho_{\text{spatial}})$ | Log length scale for GP | normal(−1.0, 0.4) | Moderately informative | $\rho$ is in standardized coordinate units; the prior median $\exp(-1.0) \approx 0.37$ corresponds to the ~1,850 km regional scale quoted here, whereas the fitted posterior (3,600–3,950 km, Table 2) lies well above it |
| $z_{\text{intercept}}[k]$, $z_{\text{slope}}[k]$ | Standardized spatial effects at knots | normal(0, $\tau_k$), with $\tau_k$ set by the density-adaptive piecewise scheme of Section S2.4.5 ($\tau_{\text{slope}}$ from 0.40 to 1.0; $\tau_{\text{intercept}}$ from 0.50 to 1.0, increasing with local data density) | Density-adaptive | Adaptive regularization to data density; prevents unrealistic values where data are sparse |
| $\sigma$ | Residual SD (includes nugget) | normal(0, 2) | Weakly informative | Determined by data |
| $\beta_{\delta^2\text{H}_p \times \text{C4}}$ | $\delta^2\text{H}_{\text{precip}} \times \text{C}_4$ interaction | normal(0, 0.5) | Moderately informative | Moderate interactions expected |
| $\beta_{\delta^2\text{H}_p \times \text{PFT}}$ | $\delta^2\text{H}_{\text{precip}} \times$ PFT interactions | normal(0, 0.5) | Moderately informative | Moderate interactions expected |

Table S3: **Regional in-sample RMSE (‰) for all 14 model variants.** Region sample sizes: Africa $n$=143; Americas $n$=373; Asia $n$=551; Europe $n$=30; Oceania $n$=32; Overall $n$=1,129. Per-region $R^2$ values are reported in the companion CSV (`manuscript/tables/Table_S2_regional_performance.csv`).

| Model | Overall | Africa | Americas | Asia | Europe | Oceania |
|---|---|---|---|---|---|---|
| baseline | 21.2 | 20.5 | 19.8 | 20.5 | 17.3 | 44.1 |
| baseline_sp | 15.9 | 12.2 | 14.7 | 17.7 | 12.4 | 15.1 |
| baseline_env | 20.3 | 19.4 | 19.4 | 20.0 | 14.3 | 36.7 |
| baseline_env_sp | 15.6 | 11.5 | 14.4 | 17.4 | 12.3 | 15.0 |
| baseline_veg | 20.1 | 14.9 | 19.4 | 19.9 | 16.3 | 41.7 |
| baseline_veg_sp | 15.7 | 11.1 | 14.2 | 17.8 | 12.4 | 14.7 |
| full | 20.0 | 16.5 | 20.0 | 19.8 | 13.7 | 36.8 |
| full_sp | 15.5 | 10.8 | 14.4 | 17.4 | 12.4 | 14.8 |
| full_interact | 19.4 | 14.8 | 18.7 | 19.7 | 13.6 | 36.6 |
| full_interact_sp | 15.5 | 10.8 | 14.1 | 17.4 | 12.0 | 15.0 |
| elevation_only_sp | 15.7 | 11.4 | 14.5 | 17.5 | 12.4 | 15.1 |
| elevation_c4_sp | 15.7 | 11.4 | 14.5 | 17.5 | 12.4 | 15.0 |
| c4_only_sp | 15.9 | 12.2 | 14.7 | 17.7 | 12.4 | 14.8 |
| elevation_c4_interact_sp | 15.7 | 11.5 | 14.4 | 17.5 | 12.4 | 14.7 |

Table S4: **Spatial confounding stress test results (Section S2.6.2).** All slopes reported in re-standardized space; $\rho_c$ denotes the constructed correlation between the synthetic spatial intercept and locally-weighted $\delta^2 H_{precip}$. Empirical $\rho_c \approx 0.45$ matches the observed correlation between fitted spatial intercepts and $\delta^2 H_{precip}$ in the real-data spatial-model fits.

| $\rho_c$ | Input $\beta$ | Posterior median | 95% CI | Bias | 95% CI covers input |
|---|---|---|---|---|---|
| 0.0 | 0.458 | 0.513 | [0.428, 0.606] | +0.055 | yes |
| 0.3 | 0.400 | 0.609 | [0.536, 0.692] | +0.208 | no |
| 0.45 (empirical) | 0.381 | 0.656 | [0.587, 0.733] | +0.275 | no |
| 0.5 | 0.376 | 0.674 | [0.605, 0.750] | +0.298 | no |

Table S5: **Prior sensitivity analysis (Section S2.6.4).** Posterior of $\beta_{\delta^2\mathrm{H}_p}$ from refits of *baseline_veg_sp* on real data under alternative prior specifications. Reference prior is $\beta_{\delta^2\mathrm{H}_p} \sim \mathcal{N}(0.8,\ 0.3)$; $\sigma_{\text{slope}}$ PC prior $P(\sigma > 0.3) = 0.05$; log GP length-scale $\sim \mathcal{N}(-1.0,\ 0.4)$.

| Prior variant | Posterior median | 95% CI |
|---|---|---|
| Reference | 0.623 | [0.497, 0.751] |
| $\beta_{\delta^2\mathrm{H}_p}$ wider: $\mathcal{N}(0.8, 1.0)$ | 0.616 | [0.481, 0.749] |
| $\beta_{\delta^2\mathrm{H}_p}$ shifted: $\mathcal{N}(0.5, 1.0)$ | 0.614 | [0.478, 0.749] |
| $\beta_{\delta^2\mathrm{H}_p}$ uninformative: $\mathcal{N}(0, 2.0)$ | 0.614 | [0.478, 0.748] |
| $\sigma_{\text{slope}}$ relaxed: $P(\sigma > 0.5) = 0.05$ | 0.627 | [0.493, 0.760] |
| $\sigma_{\text{slope}}$ very relaxed: $P(\sigma > 1.0) = 0.10$ | 0.638 | [0.499, 0.776] |
| GP length scale longer: $\mathcal{N}(-0.5, 0.4)$ | 0.627 | [0.495, 0.757] |
| GP length scale shorter: $\mathcal{N}(-1.5, 0.4)$ | 0.621 | [0.491, 0.748] |